Probing for optical and HI diffuse gas in MHONGOOSE galaxy UGCA 250

A dissertation submitted in partial fulfilment of the requirements for the degree of
Master of Science in Astronomy
Department of Astronomy
University of Cape Town

Author:
Mikhail de Villiers

November 2023

Supervisors:
Dr. Moses Mogotsi
Prof D.J. Pisano

Plagiarism Declaration

I, Mikhail Ashley de Villiers, know the meaning of plagiarism and declare that all of the work in the document except for that which which is properly acknowledged is my own.

Abstract

Extraplanar diffuse ionised gas (eDIG) has been observed in external spiral galaxies as well as the Milky Way and is distinguished by its emission-line ratios and its rotational velocity lag with respect to the galactic disk. Similarly, there is a wealth of observational evidence for extraplanar gas in the form of neutral atomic hydrogen (HI) associated with spiral galaxies. The presence of extraplanar hydrogen emission around nearby galaxies is believed to be a direct consequence of active star formation processes in the galactic disk. MHONGOOSE is an HI Nearby Galaxies Legacy Survey of MeerKAT probing the neutral atomic hydrogen in and around local disk galaxies. UGCA 250 is an edge-on, late-type spiral (Sd) galaxy part of MHONGOOSE. This work searches for signatures of extraplanar gas associated with this galaxy through studying the kinematics of the HI using tilted-ring modelling and Gaussian decomposition. This is supplemented with high-resolution spectroscopic data from the Southern African Large Telescope (SALT) allowing for the detection of extraplanar gas in both its ionised and neutral states. We find interesting kinematics in both the optical and the radio, suggesting that the kinematics should be explained by more than a simple disk model adopted in this work. The end result is a multi-wavelength characterisation of the gas associated with this galaxy. Thus, we probe for multi-phase planar and extraplanar diffuse gas associated with this galaxy. This work illustrates how sensitive HI observations with MeerKAT can be combined with high-resolution spectroscopic SALT data to achieve a complete kinematic study of a nearby galaxy.

Acknowledgements

The completion of this thesis would be impossible without my supervisors Dr Moses Mogotsi and Prof D.J Pisano. I would like to thank them for their insurmountable support, invaluable advice, endless encouragement, patience and constant willingness to read drafts of conference abstracts or provide feedback on my dissertation. Thank you to the South African Astronomical Observatory for creating an environment in which I could produce my best work.
This work was funded by the National Astrophysics and Space Science Program, which is funded by the National Research Foundation. I would like to thank Erwin de Blok and the MHONGOOSE collaboration for allowing me access to their high quality data. I would also especially like to thank Dr Moses Mogotsi for providing the SALT data used in this work and conducting the observations of the data used in this work. Thank you to my family for providing endless support in my academic endeavours.

Contents

1 Introduction

1.1 Galaxies

Galaxies are grand systems consisting of stars, gas, dust and dark matter all gravitationally bound. At first, we were uncertain whether external galaxies were truly separate from our very own Milky Way until 1923. It was then when Edwin Hubble used a Cepheid Variable star to measure the distance to the Andromeda Galaxy by implementing a period-luminosity relationship applicable to these kinds of stars. Although his initial distance estimate was incorrect, he was able to prove that those Cepheid variable stars were much further away than those detected in the Milky Way and concluded that these stars should exist in a galaxy of their own.

As Hubble expanded his observations to more extragalactic objects, he noticed that there were visual differences in the galaxies he continued to catalogue and classify. This led to his derivation of a classification scheme (Hubble, 1926) which would describe a galaxy based on its visual appearance along with further implications as to its physical conditions. This classification scheme is known as the Hubble Tuning Fork and divides galaxies into two broad categories describing their shape, spiral or elliptical. Spiral galaxies have the appearance of a spiral defined by a bulge in the centre along with spiral arms emanating from the core while elliptical galaxies are smooth and featureless in comparison. These categories are further subdivided based on finer details defining how tightly wound the spiral arms of a spiral galaxy are and whether there is a bar present in the spiral or how elliptical the galaxy is in its appearance, ranging from elongated to round.

There are also differences in their physical conditions. Elliptical galaxies are older and typically contain older stars as well as a lower dust and gas content than spiral galaxies, (Bower et al., 1992). They also have a much lower star-formation rate as a consequence of their poor gas content. Spiral galaxies have a richer gas content and consist of younger, hotter stars. Spirals (also known as late-type galaxies) typically consist of two baryonic components; a spherical bulge mainly consisting of an older stellar population and a disk composed of young stars gas and dust rotating around the bulge. Furthermore, they are often surrounded by galactic halos, mixtures of old stars, star clusters and dark matter.

1.2 Gas kinematics

Studying the kinematics of the gas within galaxies, through which we can infer the distribution of the luminous as well as the dark matter in galaxies, furthers our understanding of the underlying disk dynamics of the galaxy. Rotation curves are vital in understanding the kinematics of galaxies as they provide a means of visually describing the velocities of a galaxy as a function of the radial distance from the centre (Sofue and Rubin, 2001). They are an essential method of analysis for determining the distribution of mass within spiral galaxies and provide foundational information for studying the dynamics, formation and evolution of galaxies. Spectroscopy is an extremely powerful observing technique as it ultimately provides the means for kinematic studies of galaxies to be pursued. Radial velocities can be derived by determining the Doppler shift of the observed wavelengths of spectral lines. This allows us to obtain the redshift of the galaxy and in turn calculate its apparent velocity.

$$1 + z = \frac{\lambda_{obs}}{\lambda_{rest}} \tag{1}$$

Equation (1) shows how to determine the optical redshift of an emission or absorption line given the observed wavelength of the observation compared to the rest wavelength of the line. Similarly, to find the redshift in the radio regime, the observed frequencies are compared with its rest frequency as opposed to to a shift in wavelength. Rotation curves are commonly obtained through spectroscopic observations because implementing the Doppler equation to observed

spectral features allows one to determine the apparent velocity of the observation by multiplying the measured redshift by the speed of light. Observed rotation curves are generally thought to exhibit two types of behaviour dictated by the morphology of the galaxy they aim to describe (Casertano and van Gorkom, 1991). Typically speaking, a spiral galaxy has a rotation curve which rises steeply as we measure outward from the galactic center and it remains relatively flat at greater radii. Dwarf galaxies tend to show a rotation curve that has a gradually increasing gradient as we extend further from the galactic center and never reach a flat portion. This behaviour in the rotation curves of spiral galaxies are thought to be a consequence of the galaxy being baryon-dominated in its inner regions to being dominated by dark matter in the outer regions, while dwarf galaxies are thought to be dominated by dark matter at all radii.

Rotation curves are commonly determined in the optical by using long-slit spectroscopy. Long-slit spectra allow for rotation curves to be obtained through the use of analysing emission lines. The incoming light from the observed object enters the slit and is dispersed by a diffraction grating, separating the incoming light into a spectrum. Although long-slit spectroscopy is a widely-used observing technique in acquiring rotation curves of galaxies, it comes with flaws. Most notably it can only probe a narrow spatial region limited by the width and length of the slit used, leading to the slit most often being placed along the kinematic major-axis and minor-axis of the galaxy in observations. Hα is an emission line in the the Balmer series with a rest wavelength of 6562.85 $\mathring{A}$ in air and occurs when a hydrogen electron transitions from its third to its second lowest energy level. It is typically the brightest spectral line in the visible range and, with Hydrogen being the most abundant element in the universe, makes it the most traditionally-used spectral line to analyse when studying galaxy kinematics.

The HI (neutral atomic hydrogen) line is a robust tool in obtaining kinematic information of galaxies. It comes as a consequence of the spin-flip transition of an electron in a hydrogen atom and emits radiation at a wavelength of 21 cm and a frequency of 1420.406 MHz (Ewen and Purcell, 1951), meaning that its observations are obtained through the use of radio telescopes such as MeerKAT (Jonas and MeerKAT Team, 2016, Camilo, 2018). With hydrogen being the most abundant element in the universe, HI observations have been and continue to be widely used in tracing the neutral gas content in the universe (e.g Rogstad and Shostak, 1971). An added benefit of observing the neutral hydrogen content of galaxies is that it typically extends much further than its ionised counterpart, making it an ideal tool for probing the most outer regions of galaxies (e.g. Swaters, Sancisi, and van der Hulst, 1997).

Early studies of neutral hydrogen involved observing with a single radio dish, but in recent years observations have improved through the use of radio interferometry where many dishes work in conjunction for simultaneous observations. This allows for the baselines to be configured between this dishes in order to obtain a higher spatial resolution in the observations. One disadvantage of observing the HI line as opposed to Hα is that radio observations can not attain as high a spatial resolution of that of optical observations, making the combination of multi-wavelength data a valuable asset in obtaining a complete kinematic study of a galaxy.

1.3 Extraplanar gas

The existence of gaseous, multi-phase galactic halos encompassing the disks of spiral galaxies comes as a direct consequence of the star-formation activity within the disks of these galaxies. This has been reinforced by the theory of a 'disk-halo' connection whereby the morphology and presence of the halo correlates directly with the activity occurring in the disk of the galaxy. Many models have been suggested to explain the mechanisms behind the transport of gas and energy from the disk into the halo; such as the *chimney* phenomenon whereby gas is driven by collective Supernovae explosions (SNe) into the halo (Norman and Ikeuchi, 1989) or the *galactic fountain* model (Shapiro and Field, 1976). Other theories involving starburst galaxies have also been imposed, such as the condition of a superwind which catalyses the movement of outbreaking gas from bubbles into the galactic halo (Lehnert and Heckman, 1996).

Observations of nearby spiral galaxies have provided evidence of copious amounts of gas, in the form of neutral atomic hydrogen (HI) extraplanar gas (EPG), residing in their halos at fairly great distances from the thin disk. In particular, NGC 891 is a galaxy which has been extensively studied and is known to exhibit an extensive halo of HI gas which approximately accounts for about 30 percent of the galaxy's entire HI mass (Oosterloo et al., 2007). The phenomenon of the coalescence of HI EPG has been extensively studied and has been essentially subdivided into two models: the inflow model and galactic fountain. The inflow model aims to explain how galaxies obtain sufficient gas to continue to form stars and proposes that galaxies accrete gas from the large reservoirs of gas surrounding them (e.g. Bregman, 2007). Previous studies have shown that mergers of dwarf galaxies with spiral galaxies fail to provide sufficient mass which would sustain the star formation in the galaxy (Di Teodoro and Fraternali, 2014). Thus, it is believed that galaxies should be acquiring their gas through some other mechanism, thought to be the accretion of gas from the intergalactic medium (IGM). Cold accretion is a method through which galaxies accrete gas via the means of the gas flowing along cold filaments through the circumgalactic medium and remains cool as it falls onto the disk (Kereš et al., 2005). It serves as a main idea of how galaxies accrete more gas in order to sustain the star formation within them as well as a description of the origin of EPG. An alternative explanation for EPG would be the galactic fountain model which describes the EPG as being expelled from the disk via the expansion of superbubbles near young, hot O- and B-type stars. In this picture, gas is ionised and expelled from the disk. As it travels upward, the hydrogen cools and recombines to once again form neutral hydrogen gas. This gas undergoes thermal instabilities (Field and Saslaw, 1965) and coagulates, creating cool, condensed clouds which ballistically return to the disk.

Ionised gas existing within the galactic halo and residing above or below the plane of the galaxy is most commonly referred to as *extraplanar diffuse ionised gas* (eDIG) and is vital for determining the distribution of baryons in the universe as well as the enrichment of the intergalactic medium. These eDIG layers have proven to be most prevalent in late-type star-forming spiral galaxies (e.g. Rossa and Dettmar, 2003) comparable to that of the *Reynolds layer* in the Milky Way (Reynolds et al., 1999). Akin to the origin of neutral extraplanar gas, the presence of eDIG is believed to come as a consequence of activity within the disk such as the rate of star-formation occurring within the disk (e.g. Rossa and Dettmar, 2003). OB stellar populations tend to ionise their surroundings which often gets ejected from the disk via stellar winds and resides above or below the plane of the galaxy as eDIG. Observations have shown a correlation between the intensity of the eDIG emission and the areas of HII regions in the disk, further reinforcing the notion that the primary source of ionisation of the eDIG is photoionisation from OB stars residing in these HII region (e.g. Miller and Veilleux, 2003).

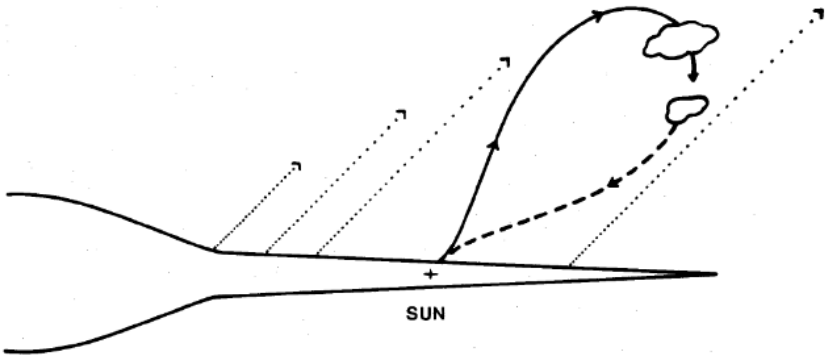

Figure 1: *An illustration taken from Bregman (1980) depicting the mechanism of a galactic fountain. The dashed arrows refer to hot gas rising from the disk. The solid arrow shows the cycle of gas in a galactic fountain in which the gas travels radially upward, cools and eventually returns to the disk.*

Previous studies and observations of eDIG in edge-on systems have proved to show convincing lines of evidence reinforcing the idea of star formation in the disk being the driving force for copious amounts of gas observed in galactic halos. Filament-like formations, anchored by HII regions in the disk, have been shown to be present in many galaxies and are thought to trace regions of active star formation in the disk (Rand, 1996). Furthermore, a measure of the star formation rate per unit area using the FIR (far-infrared) luminosity of the disk has been shown to be directly proportional to the presence of eDIG in the halo (Dettmar, 2005).

Spectroscopic studies of HI and Hα have revealed the presence and following properties of EPG: (1) EPG shows a lagging rotation, with velocity gradients typically of the order of -10 to -20 km s^{-1} kpc^{-1} (e.g. Fraternali et al., 2002, Fraternali et al., 2004). (2) EPG has a scale height of several kpc (Swaters, Sancisi, and van der Hulst, 1997). These properties are true for both EPG and eDIG, however HI EPG typically extends further from the disk than its ionised counterpart. eDIG extending further than the neutral gas implies the existence of some extending ionising sources as well as the ionisation caused by leaking photons from the star formation regions in the disk (Lu et al., 2023a). The kinematics of EPG and eDIG prove to exhibit similar behaviour, suggesting that neutral and ionised gas in the halo perhaps have the same origin (Rossa and Dettmar, 2003). EPG layers are not, however, ubiquitous in galaxies; a notable example is NGC 4565 which has been shown to not possess an extended HI extraplanar layer throughout the galaxy (Zschaechner et al., 2012).

1.4 Halo Kinematics

Previous studies of edge-on systems have revealed vertical extensions of neutral and ionised EPG with the neutral EPG extending to several kpc from the plane (e.g. Oosterloo et al., 2007). Studies have involved extensive modelling of the kinematics of halo gas to gain a better understanding of the dynamics of this layer. NGC 891 is regarded as being the first galaxy in which the lagging layers of gas in the halo has been addressed. The DIG of NGC 891 was studied by Rand (1997) through which the ionised gas was probed through a long-slit observation placed perpendicular to the plane of the disk of the galaxy; allowing for the DIG to be observed on either side of the plane of the galaxy. This study involved analysing the emission line ratios between forbidden emission lines to that of Hα and they found that the smooth increase of [NII](λ6583)/Hα with vertical height from the galactic disk is exactly as expected in photoionisation models. Although this trend holds true, it has commonly been seen in eDIG layers that many line ratios cannot be explained by photoionisation alone and instead suggests the presence of an additional ionisation mechanism (Haffner et al., 2009)

The kinematics of extraplanar material is used as a proxy for determining the origins of the gas. A kinematic lag is expected in gas that is ejected from the disk of the galaxy and moves away from the plane. As the gas moves further away, it experiences a weaker gravitational force. Due to the conservation of angular momentum, the magnitude of the velocity of this gas must decrease; giving rise to a kinematic lag with respect to the gas in the disk of the galaxy. Studies such as Oosterloo et al. (2007) and Heald et al. (2007) have focused on assessing the negative gradient in the velocities of the extraplanar gas as we move away from the midplane of the galaxy. It must be said, however, that if the lag detected in extraplanar regions deviates from what one would expect from a shallowing velocity solely due to a weaker gravitational force, then there must be some other factors influencing the gas' kinematics.

In nearby edge-on systems, a typical velocity gradient of Δv = -10-40 km s^{-1} kpc^{-1} is considered to be characteristic of multi-phase, gaseous haloes (e.g. Fraternali et al., 2002, Heald et al., 2007). Lags observed in nearby , edge-on eDIG layers in excess of this gradient can often be characterised as being evidence of a galactic fountain as they have to slow down at a greater negative gradient in order to conserve angular momentum (e.g. Collins et al., 2002). There are, however, a number of other factors that could influence this such as a radial pressure gradient, coupling between the disk and the halo or the mixing of fountain gas with accreting material (e.g. Li et al., 2023).

The kinematic lags in the galactic halo has extensively been studied by probing the intermediately inclined spiral galaxy NGC 2403 by probing the neutral HI (Fraternali et al., 2002) and the eDIG (Fraternali et al., 2004). Fraternali et al. (2002) detected a faint, gas component with anomalous velocities (gas with velocities that deviate from the trend of the disk-gas in the same region) which presents itself in the HI line profiles as broad wings with velocities slower than the rotation velocity. These wings can only be attributed to the presence of an extraplanar HI region rotating slower than the gas in the disk. Fraternali et al. (2004) used optical long-slit spectroscopy to study the eDIG layers in NGC 2403 with the main purpose of comparing the kinematics of the ionised gas to that of the neutral hydrogen studied in Fraternali et al. (2002). It was found that, in general, the kinematics of the neutral and ionised gas were in agreement with each other. The spectra from the optical observations showed tails of emission in the Hα profiles at velocities lower than the systemic velocity of the galaxy. This can be thought of as a large-scale lagging ionised gas component which is interpreted as the ionised counterpart of the lagging HI halo. This conclusion was further confirmed by assessing the trend in the ratio of [NII](λ6583)/Hα, in which there is an increasing gradient in the ratio with decreasing rotation velocity. Ratios of various forbidden emission lines with Hα provide constraints on photoionisation models. For example, in NGC 891 the ratio of [NII](λ6583)/Hα is enhanced compared to HII regions and increases with height off the plane. This behaviour is expected in photoionisation models and stems from the increasing dilution of the radiation field.

The eDIG layer of the Milky Way, the Reynolds layer, has been thoroughly studied through optical spectroscopy. Photoionisation models have been constructed to explain the trend in the ratios of forbidden emission lines to Hα and have successfully explained the features observed in the DIG (Domgorgen and Mathis, 1994). These features include the ratios of [SII](λ6716)/Hα and [NII](λ6583)/Hα that increase with distance from the midplane of the galaxy and the low ratios of [OIII](λ5007)/Hβ with respect to HII regions (e.g. Rand, 1998, Otte et al., 2002). Thus, assessing the trend in the ratios of [NII](λ6583)/Hα as a function of height in an edge-on galaxy proves to be valuable as it serves as an indicator for the presence of eDIG. Going forward in this work we refer to [NII](λ6583) as [NII].

1.5 MHONGOOSE

The MHONGOOSE survey (MeerKAT Observations of Nearby Galactic Objects - Observing Southern Emitters, de Blok et al., 2017) is a deep HI survey of 30 nearby galaxies using MeerKAT with the goals of providing an improved means of studying the interstellar medium, star formation and the baryon cycle in the outer regions of nearby star-forming galaxies. Three of the chief scientific aims of the survey are to study the relation between gas and star formation, the baryon cycle as well as the relation between the distribution of dark and baryonic matter within these galaxies. The survey will produce unprecedented HI extragalactic data at both high spatial resolution as well as high sensitivity, serving as a successor to previous HI surveys such as THINGS (Walter et al., 2008) or HALOGAS (Heald et al., 2011) which have only either achieved high spatial resolution or high sensitivity. It involves a sample of 30 nearby disk and dwarf galaxies covering a range of HI masses from about 10^6 to 10^{11} $M_\odot$ in order to provide a uniform coverage of the available range in $\log(M_{HI})$. These observations will be extremely deep, down to HI column density limits of below 10^{18} cm^{-2}, which is a factor of about a hundred times fainter than the typical HI disks in galaxies.

The MHONGOOSE sample consists of galaxies primarily covering the aforementioned range in HI mass. The galaxies in the sample have all been previously observed in multiple wavelengths. The detections in HI were completed as part of the HIPASS (HI Parkes All Sky Survey, Meyer et al., 2004). Furthermore, these galaxies were detected in Hα, optical, infrared and ultra-violet wavelengths as part of the SINGG and SUNNG (The Survey for ionisation in Neutral Gas Galaxies, Meurer et al., 2006) surveys. An additional selection criterion applied pertains to the star formation rate (SFR) of the galaxies, ensuring that the separation of HI gas in the disk from diffuse HI extending further from the disk would be feasible. The diversity in the sample is further enhanced by including galaxies covering a range of inclinations including face-on, edge-on and intermediate inclinations as well as a range of morphologies from irregular dwarf galaxies to grand-design spirals. HI is ideal for probing the outer regions of the galaxy, however, the baryons are most concentrated in the center. Probing these denser regions raises the requirement for more efficient spatial sampling in order to effectively model and study the gas kinematics in these denser areas.

In addition to the observations conducted with MeerKAT, there is a project in place which aims to obtain optical spectroscopic data with SALT to complement the radio observations. This entails performing resolved spectroscopy on a sample of MHONGOOSE galaxies selected by encompassing a range in HI masses and inclinations. These observations will be conducted at spatial resolutions significantly higher than that of the radio observations, allowing for the innermost regions of these galaxies to be studied in finer detail through optical wavelengths. This programme has the following immediate science objectives (1) Determine the kinematics of the ionised gas and utilise it to derive rotation curves with the aims of probing for galactic winds and extraplanar gas. (2) To characterise the ionised gas and perform line ratio diagnostics to identify the presence of shocks, diffuse extraplanar gas and AGN activity in the galaxies. (3) Determine the stellar kinematics, which can be used to probe the dark matter distribution through stellar dynamical modelling when used in conjunction with optical imaging. (4) Determine the star formation rates, star formation histories via stellar population modelling and stellar and gas metallicities of the galaxies.

The star formation rate density over cosmic time has decreased since a redshift of z≈2 (Madau and Dickinson, 2014). It has also been shown that mergers between dwarf galaxies and spirals are unable to provide the required gas to maintain star formation in those galaxies (Di Teodoro and Fraternali, 2014). Thus, if mergers are unable to support the star-formation rates exhibited by spiral galaxies, it stands to reason that they must be obtaining gas through some other mechanism. A leading idea is through the accretion from the intergalactic medium (IGM), which is the term used to describe the gas that permeates the space in between galaxies. Thus, MHONGOOSE avoids observing dense group and cluster environments along with strongly interacting galaxies, due to previous studies showing that gas acquired from companion galaxies and galactic fountain processes are minimized in these environments (Espada et al., 2011). The sample of MHONGOOSE galaxies provides the most favourable conditions and environments to detect accretion of gas onto galaxies.

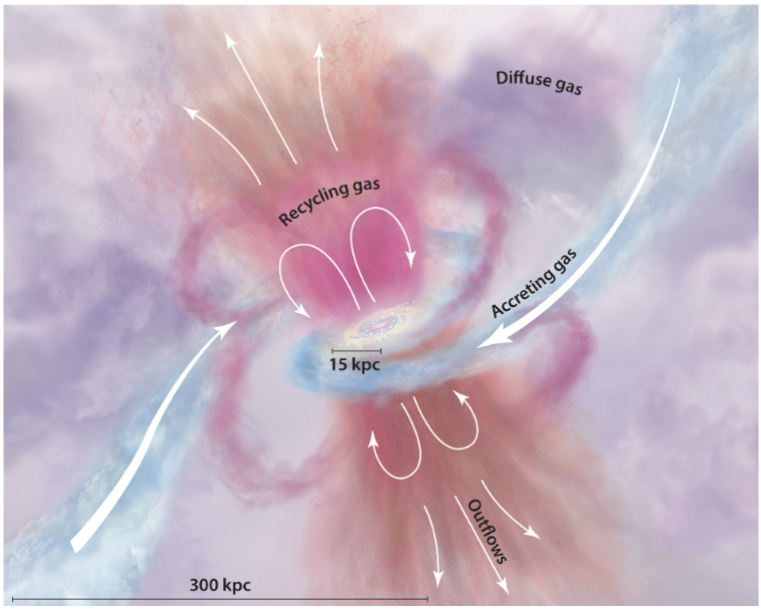

Figure 2: *A depiction of the baryon cycle and feedback associated with a galaxy. Galaxies are thought to accrete gas from the IGM and expel gas through outflows emanating from the disk of the galaxy (Tumlinson et al., 2017)*

2 The data

The galaxy observed was UGCA 250, a spiral galaxy spanning an angular size of 1.76 arcminutes (Skrutskie et al., 2006) with active HII regions. Observations were conducted with the Southern African Large Telescope (SALT) (Buckley et al., 2006), using the Robert Stobie Spectrograph (RSS) (Burgh et al., 2003) as well as with MeerKAT.

Parameter	Value	Notes
Morphology	Sd	(1)
RA (J2000)(deg)	178.35	(2)
Dec (J2000)(deg)	-28.55	(2)
Distance (Mpc)	24.4	(3)
Heliocentric velocity (km/s)	1707.02	(4)
z	0.005694	(5)
Inclination (deg)	74.93	(6)
B mag.	12.75	(7)

Table 1: *Properties of UGCA 250. (1) de Vaucouleurs et al., 1991.* (2) J2000 optical position from NED. (3) Meurer et al., 2006 (5) Koribalski et al., 2004. (6) Calculated using the axial ratio of 0.26 from NED. (7) The B-band magnitude (Doyle et al., 2005)

RSS is the main instrument on SALT and has several useful capabilities. It is situated at the prime focus and was designed to have a range of observing modes, each with flexible configurations. The capabilities of RSS involve narrow-band imaging, long-slit spectroscopy, multi-object spectroscopy, Fabry-Perot imaging spectroscopy and high time-resolution spectroscopy. For our science case, we make use of data obtained using the RSS's long-slit functionality. Long-slit spectroscopy involves placing a narrow slit at the entrance of the aperture of a spectrograph. The incoming light enters the slit and is refracted by the means of a diffraction grating after which the dispersed light is captured by the detector, in RSS' case this detector is a charged-coupled device (CCD). The main drawback of this is that only a very narrow region is being observed. This is dictated by the width of the slit which governs the spectral resolution of the observations. A narrower slit yields a higher spectral resolution, but the spectrum is fainter on the CCD while the converse is true for a wider slit. The length of the slit determines the spatial coverage of the observation. Thus, long-slit spectroscopy allows for the acquisition of spatially resolved spectral data of a galaxy. In the case of observing an edge-on galaxy, this has the appropriate utility of acquiring highly resolved spectral data along the entire major-axis of the galaxy provided the slit is orientated with the same position angle as the galaxy and the length of the slit extends across the galactic disk.

2.1 Optical Data

We use long-slit spectroscopic data obtained with the Robert Stobie Spectrograph (RSS) on SALT. These observations were obtained over 4 observing runs. All the observations were obtained using a 0.6" × 8' slit using the PG2300 grating ensuring that the spectra were obtained at high spectral resolution (R≈8000). The initial observations involved aligning the slit along the major-axis and minor-axis of the galaxy.

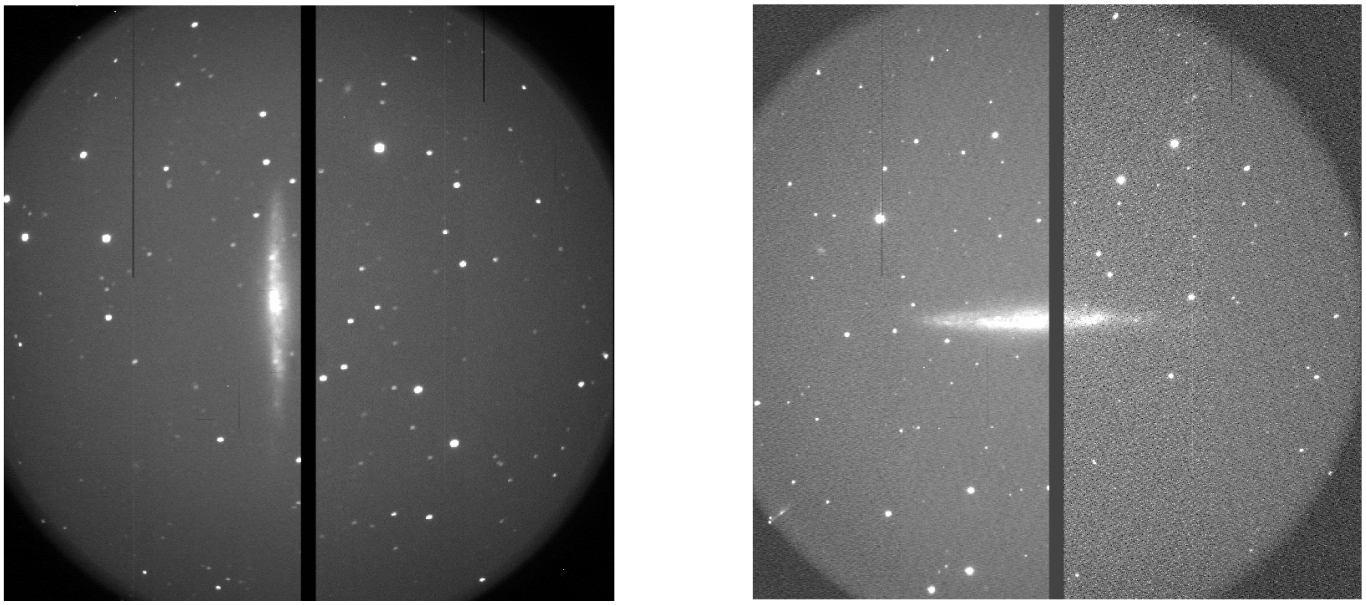

(a) (b)

Figure 3: *SALTICAM images of the galaxy along the (a) major-axis and the (b) minor-axis. This shows the alignment of the slit along the disk of the galaxy for the major-axis and perpendicular to the disk for the minor-axis.*

Follow-up long-slit observations were taken where the long-slit was orientated parallel to the major-axis but offset by 13.7" in order to probe potential regions of eDIG in the form of emission slightly off the disk. Similar observations were taken along the minor-axis of the galaxy in which follow-up observations included aligning the slit parallel to the minor-axis at an angular offset of 1'. This allows us to assess how the behaviour of the gas changes with distance from the midplane as well as asymmetries in the kinematics of the disk. All the observations were taken with a grating angle of 47^o, providing a wavelength coverage of 5872 $\AA$ to 6732 $\AA$.

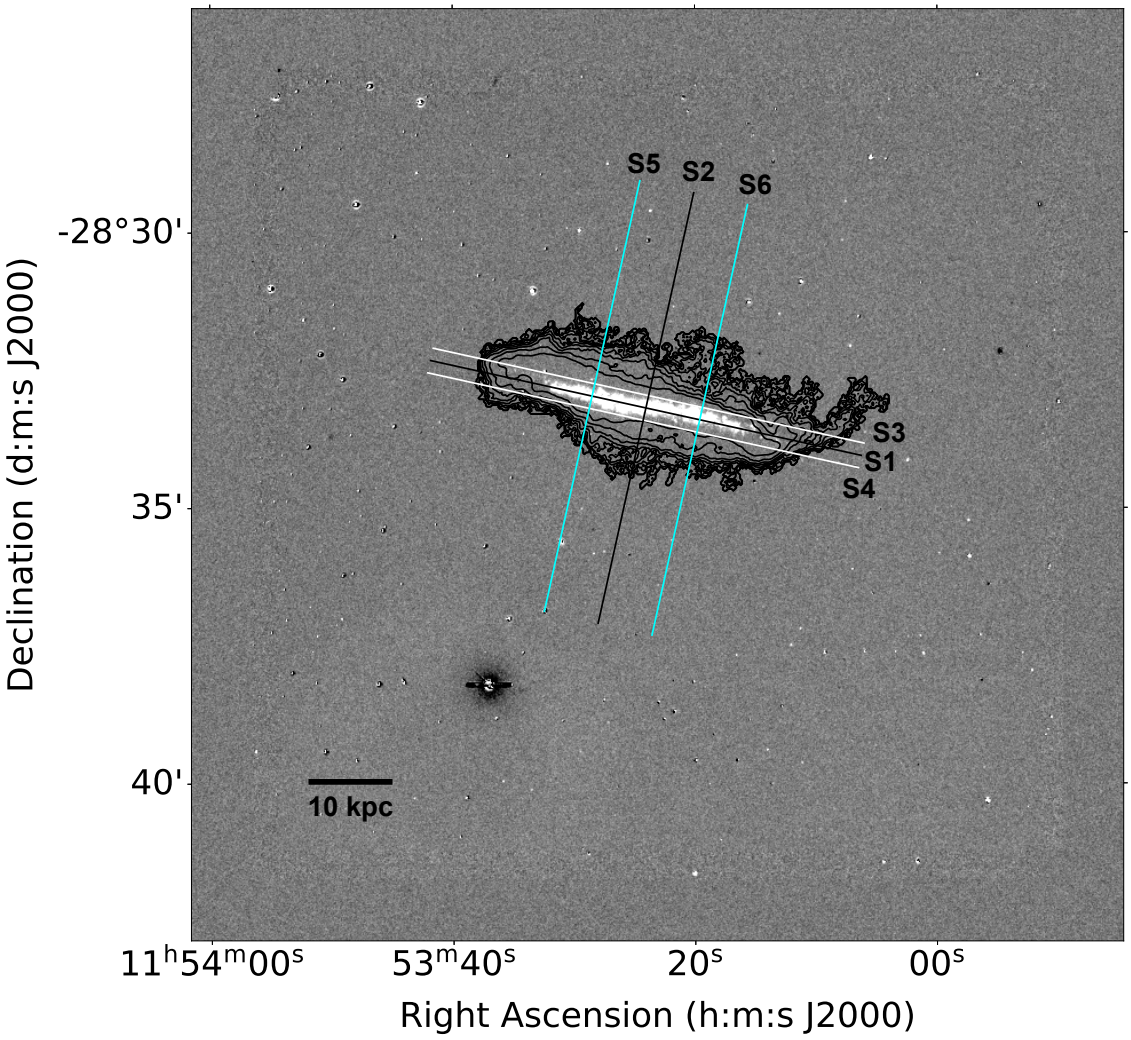

Figure 4: *Slit positions of the long-slit observations overlaid on an Hα-band image of UGCA 250 alongside the HI contours shown in units of 2^n × RMS where n=1,2,..,9. S1 and S2 lie along the major-axis and minor-axis respectively. Slits S3 and S4 are positioned parallel to the major-axis, with S5 and S6 parallel to the minor-axis. This shows the structural warp in the galaxy. The observational effects of which are that slits S3 and S4 both appear to only be probing emission from only one half of the galaxy.*

Slit label	RA (J2000)	Dec (J2000)	P.A (deg)	t_{exp} (s)
S1	11:53:24.06	-28:33:11.40	77.4	2200.295
S2	11:53:24.06	-28:33:11.40	347.4	2200.289
S3	11:53:23.83	-28:32:58.03	77.5	1050.217
S4	11:53:24.29	-28:33:24.77	77.5	1050.213
S5	11:53:28.50	-28:32:58.32	347.4	1010.139
S6	11:53:19.62	-28:33:24.48	347.4	1010.135

Table 2: *Observing summary for the long-slit observations. This includes the coordinates at which the observations are centered, RA (Right Ascension) and Dec (Declination), as well as the position angle of the slit (PA) and the exposure time of each observation. The coordinates of the slit positions are the coordinates of the center of each slit. The Position angle is measured as the angle from North.*

2.1.1 Data reduction

The reduction of the long-slit data was done using IRAF (Image Reduction and Analysis Facility) (Tody, 1986). All the data had undergone the initial data reduction using the SALT science pipeline which included bias, gain, and cross-talk corrections and image preparation and mosaicking (Crawford et al., 2010). The raw products had to be trimmed and the chipgaps, as a result of the CCD, had to be interpolated over. The L.A.Cosmic package was used to remove cosmic rays from the data (van Dokkum, 2001). The wavelength calibration was achieved by using the IRAF tasks `noao.twodspec.long-slit.identify,reidentify,fitcoords` and `transform` and the Ar comparison lamp spectra. The background subtraction and extinction correction was further determined by the tasks `background` and `extinction` respectively. Finally the apertures were extracted for each of the spectra by utilising the `noao.twodspec.apextract.apall` task.

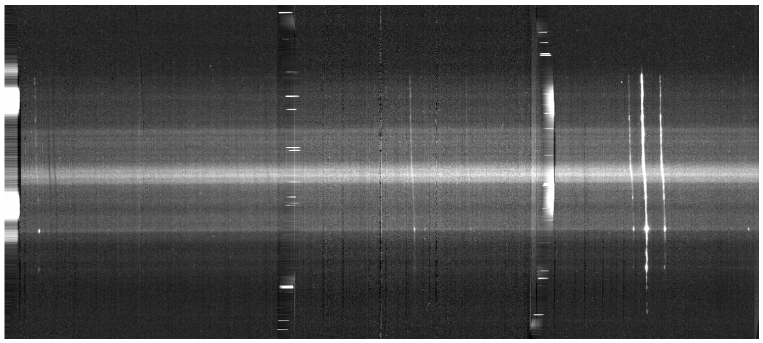

Figure 5: *The fully reduced optical spectrum along the major-axis (S1) of UGCA 250. The y-axis corresponds to the spatial axis of the slit and the x-axis is the wavelength axis. The brightness of the pixel represents the intensity of the emission. The three emission lines on the right are the two Nitrogen lines [NII] 6548 Å and 6583 Å, with Hα situated between them.*

2.2 Radio Data

The MHONGOOSE observations with MeerKAT used as an interferometer begun in October 2020 with each galaxy being allocated with 55h of observations time. Each observation required a minimum of 58 active antennae to ensure high-quality data. The radio data consists of a three-dimensional data set (cube) with two spatial axes and one spectral axis defined by frequency or velocity.

Parameter	Value
Beam size	14.37" × 9.82"
Beam position angle (°)	138.84
Velocity resolution (km s^{-1})	1.38
Pixel size (")	3
Noise (mJy $beam^{-1}$)	0.17 ± 0.01

Table 3: *Description of the radio data and observations. BMAJ and BMIN refer to the size of the major-axis and minor-axis of the beam, respectively. BPA refers to the beam position angle.*

The data was processed with the CARACal data reduction pipeline (Józsa et al., 2020). The steps in the data reduction involved (i) flagging the calibrators, (ii) cross calibration, (iii) flagging the target, (iv) imaging the continuum, (v) transferring of the self-calibration solutions to the original measurement set, (vi) subtracting the continuum from the original measurement set using the self-calibration sky model and (vii) deconvolving and creating the spectral line HI data cubes. These steps are explained in much more detail in de Blok (2023, in prep).
The radio cube consisted of 1800 × 1800 spatial pixels and 700 channels. The analysis here only involves the galaxy at the center of the FOV, therefore the data was trimmed to 700 × 700 spatial pixels and 252 velocity channels to ease computational processes in the analysis.

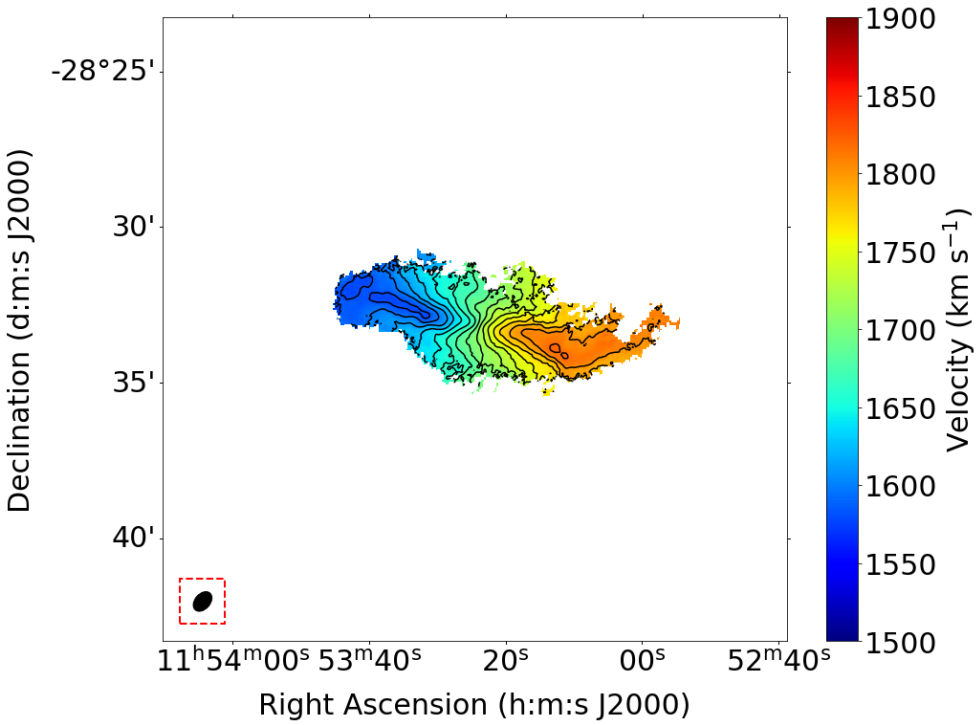

Figure 6: *Moment 1 map of UGCA 250 created with a mask that only contains emission from pixels satisfying 3σ. The beam size is shown in the lower left corner of the figure. The contours range from 1550 km s^{-1} to 1850 km $^{-1}$ and are spaced 15 km s^{-1} apart.*

3 Analysis

3.1 Optical emission-line fitting

The wavelength range of the optical spectroscopic observations allow for the detection of the Hα and [NII] emission lines. An emission line is usually shaped like a Gaussian distribution, thus modelling an emission line as a Gaussian function allows for one to obtain the parameters which govern the behaviour and shape of the emission line. This function is represented by:

$$f(x) = ae^{-\frac{(x-b)^2}{2\sigma^2}} \tag{2}$$

where a refers to the amplitude of the function which is the peak intensity, b the mean which is the wavelength peak intensity and σ the standard deviation, governing the width of the emission line. Each of these parameters are vital for describing the kinematics of the object. The mean allows us to employ the Doppler equation (1) and calculate the velocity the emission line is associated with. The standard deviation relates to the velocity dispersion in the gas which is a measure of the statistical spread of velocities around the mean velocity of the system at that point.

The emission lines are fit by using least-squares minimization through using the Python package `lmfit`. The algorithm consists of supplying the function with initial guesses to optimise the fit. The position of the emission line was found by first defining a wavelength range in which we expect the line to reside, by taking the value for the redshift of the galaxy from known literature. In this interval, the maximum intensity value was taken as an initial guess for the amplitude of the fitted function. The wavelength where the intensity reaches its maximum value was then taken as the initial guess for the mean of the Gaussian. The fitting software was not sensitive to initial guesses for the standard deviation, thus a standard deviation which corresponds to the typical value of the velocity dispersion of the Hα line was taken as an estimate (corresponding to 20 km s^{-1}). To ensure the quality of the fit, it was found that employing a signal-to-noise (SNR) cut-off of 4 to the Hα emission line provided reasonable fits. Thus, all fits in which the amplitude of the fitted Gaussian was less than 4 times the value of the noise in the profile was discarded. The noise in each profile was estimated by taking the standard deviation of the data in a region where there is no emission, in our data we selected the region of 6686 $\mathring{A}$ to 6726 $\mathring{A}$.

3.1.1 Multiple-component fitting

Approximating an emission line by the shape of a Gaussian function is a reasonable assumption to make. However, there could be multiple contributions that stem from different regions of gas in this galaxy which present themselves as different components in the emission lines. Due to the galaxy being highly inclined, along a line-of-sight (LOS) multiple components in the disk contribute to an emission line. In other words, there are multiple contributions from different regions of gas in an observed emission line resulting in a line with many components stemming from different regions. The model in this work consists of fitting the emission-line with two components, a broad and a narrow component. The physical justification for this is that a denser planar HII region contributes a Gaussian component with a narrower width while more diffuse gas in the same region could result in the emission line exhibiting broadened wings.

A consequence of the high inclination is that along a LOS we can get multiple HII gas components in different regions of the disk, with significantly different kinematics, contributing to the emission-line profiles. This causes broadening of the emission-line which can not be attributed to diffuse gas. HII regions are often found as Strömgren spheres in a galaxy (Strömgren, 1939) where a sphere of ionised hydrogen encases a young O or B type star. However, here we refer to HII regions not only as that, but also as the dense, disk, ionised gas associated with star-forming regions in the disk. Thus, it is vital to assess whether these emission lines consist of either one or multiple components. While adding more Gaussian components to fit an emission line will assuredly improve the fit as we continue adding components, we run the risk of adding too many components and could overfit the line. Here, we approximate the emission line as two components which generally consist of a broad and a narrow Gaussian. These come as a consequence of the aforementioned justification that the narrow Gaussian is considered to be emission originating from the denser, planar ionised gas while the broad component is attributed to the more diffuse gas in the galaxy (both planar and extraplanar).

This was further justified upon visual inspection of several of the emission line profiles where a single Gaussian provides a reasonable fit to the data, but there are clearly wings of emission in the base of the profile which indicate the presence of more than a singular component, as shown in Figure (7). This trend is noticed in approximately all of the ionised emission line profiles for this galaxy and is reinforced by the inclination of the galaxy. Since the system is so highly inclined and our LOS effectively samples information from many radii of the disk, the contributions from the denser regions of ionised gas provide the greatest amount of emission in the profiles. These regions are typically associated with those previously described pockets of HII regions residing in the disk of the galaxy. This reasoning holds especially true for the data set described here as a long-slit observation is conducted by aligning the slit along the major-axis of the galaxy.

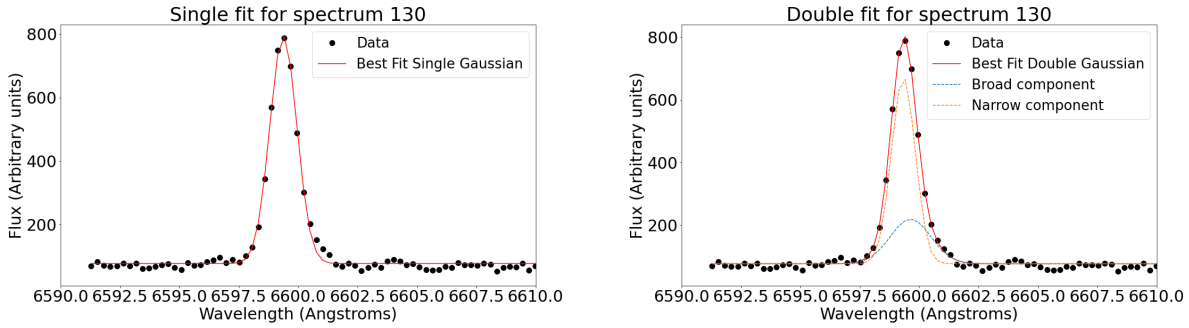

(a) (b)

Figure 7: *Hα profiles showing the difference in fitting the emission line with a Single Gaussian (a) and with two Gaussian components (b). The two-component Gaussian is an improved fit since it is able to model the wings of emission at the base of the profile.*

Thus, we approximate the emission line as a superposition of two Gaussian functions, one narrower function and one broader function. We refer to these components as the narrow and broad components respectively. The algorithm to determine the initial fits is largely the same, however, first the parameters are estimated for that of a single Gaussian function. This is taken a step further and the single Gaussian is used to approximate initial guesses for a broad and narrow Gaussian now having a general sense of the shape of the line. We aim to assess the trends in the ratios of [NII]/Hα for both the single-component fits as well as the two-component fits. Thus, to maintain consistency when comparing the ratios of the multiple components (i.e we compare the flux ratio of the broad [NII] component to that of the broad Hα component) we modify our initial guesses when fitting the [NII] line. First, the fit is performed on Hα and the profile is further decomposed into the two components. Now knowing the fit parameters of the two components, we use this when supplying an initial guess to our fit performed on the [NII] line. We assume that the separation of the velocities of the two Gaussian components in [NII] is equivalent, to that of the separation of the means in the Hα line. Furthermore, we take the standard deviation of the broad and narrow fitted components in Hα as initial guesses for that of the broad and narrow components in [NII]. Thus, we intrinsically tie together the shapes of the profiles for Hα and [NII] respectively.

To ensure that we indeed compare the same region of gas, we fix the dispersion values of the [NII] broad and narrow components to their respective counterparts in the Hα line. Furthermore, we fix the velocities of the [NII] components to the Hα components. The decomposition of the optical emission lines was performed on each of the data sets, however, failure to detect two components (under our fitting criteria) was experienced in all the spectra from the observations conducted parallel to the major-axis. This is also true for the [NII] emission line in these sets, thus only single component Gaussians were fitted to Hα for these data sets.

3.2 Asymmetric-drift correction

The measured velocities are the true velocities of the gas, but these velocities may not reflect the circular velocity due to the influence of pressure support. This causes the observed velocities to deviate from the true velocities of the gas, resulting in an Hα rotation curve with substantially lower velocities than the true rotation velocities of the gas. Correcting for this deviation in these observed velocities involves applying an asymmetric drift correction which accounts for pressure support in the observed Hα rotation velocities (e.g. Erroz-Ferrer et al., 2016).
We assume that the vertical scale height (R_{exp}) is at a constant perpendicular height with radius. The Hα surface brightness profiles are derived from SINGG images of the galaxy and these values are fit with an exponential function defined by:

$$I = I_0 e^{\frac{-R}{R_{exp}}} \tag{3}$$

where I refers to the intensity, I_0 refers to the intensity in the midplane, R is the distance measured perpendicularly from the midplane of the galaxy and R_{exp} is the scale height of the galactic disk. The peak in Hα emission, I_0, is derived from the brightest region of HII emission.
We assume that the velocity dispersion is isotropic with the velocity dispersion components in the azimuthal, radial and vertical all being equal, i.e σ_ϕ=σ_R=σ_z. This is a fair assumption to make regarding gaseous disks (Lelli et al., 2014). The observed velocity dispersion in ionised gas comes as a consequence of different phenomena. Thermal broadening, turbulent motions, gravitational interaction between particles, natural broadening of the line (σ_N) and instrumental width (σ_{inst}). The velocity dispersion of the Hα line can be described as the superposition of all of these phenomena (Erroz-Ferrer et al., 2016):

$$\sigma^2_{obs} = \sigma^2_{grav} + \sigma^2_N + \sigma^2_{inst} \tag{4}$$

The gravitational velocity dispersion described in equation (4) is taken as the total contribution of the turbulent and thermal dispersion (Westfall et al., 2011). The instrumental width was taken by performing a single Gaussian fit on emission lines in the calibration lamp used for the optical spectroscopic observations. These fits were conducted on lines within 100 $\AA$ and calculating the velocity dispersion described by this fit. This value was taken to be 15.15 km s^{-1} which corresponds to a resolution of about R≈8500, a reasonable value to be associated with the high-resolution SALT data. Here the natural broadening of the line is taken to be $\sigma_N = 3$ km s^{-1} (O'dell and Townsley, 1988) and σ_{obs} is found by fitting singular Gaussian components to the given emission line.
Assuming a Sersic profile for the galaxy (Sérsic, 1963) to describe the intensity of the galaxy as a function of galactic radius, we can use equation (A.6) from Lelli et al. (2014) to describe the circular velocity as:

$$v_c^2 = v_{rot}^2 + \sigma_{grav}^2 \left[\frac{b_n}{n} \left(\frac{R}{R_{eff}} \right)^{1/n} - 2 \frac{\partial \ln \sigma_{grav}}{\partial \ln R} \right] \tag{5}$$

Equation (5) describes the circular velocity v_c with n being the Sersic index, b_n being a constant value dependent on the Sersic index and R_{eff} the effective radius. For rotating spiral galaxies, the surface brightness profile can be well-approximated by an exponential function, therefore we take n=1 and b_1=1.678 with $R_{eff} = 1.678 \times R_{exp}$ (Lelli et al., 2014). This simplifies Equation (5) to:

$$v_c^2 = v_{rot}^2 + \sigma_{grav}^2 \left(\frac{R}{R_{exp}} + \frac{2R}{R_{exp}} \right) \tag{6}$$

Equation (6) is the final correction applied to the derived velocities found from fitting the optical emission lines. R_{exp} was found by fitting a decaying exponential to a projection of the Hα intensity taken as a function of height from the centre of the disk where the maximum intensity is detected. This value was found to be 4.18" which corresponds to a physical scale of 0.49 kpc, a reasonable approximation for a galaxy of this morphology. For each fit performed on an emission line, the velocity dispersion of the line is taken to be σ_{obs} and σ_{grav} is found by applying Equation (4) to the aforementioned measured dispersion. This corrects for the deviations from the true motions in the measured velocities of the ionised gas.

3.3 Resolution of optical spectra

As a further means of justification for the fitting of Gaussian profiles to the emission lines in our spectra, we investigate the associated shapes of the spectral lines present in the ARC lamp used for the observations. For each of the associated ARC spectra, we apply the same reduction steps and wavelength solution to the observational spectra. Thereafter, a few bright spectral lines are identified within about 100$\AA$ of where we would find the Hα line considering the redshift of our source. These lines are fitted with a single Gaussian profile and the associated FWHM of the lines are found and related to the spectral resolution of our observations. We further assess the shape of the Gaussian profiles as we progress through the spatial axis of our long-slit data. This shape is quantified by taking the ratio of the standard deviation and the amplitude of each fit of the spectral line for each pixel along the spatial axis. This stays largely the same throughout the spatial axis of the slit with minimal or no variation.
The velocity resolution is found by taking the ratio of the wavelength of the fitted line (which is determined by the mean value of the fitted Gaussian) to the associated FWHM (found by using the standard deviation of the fit). This was conducted on each of the data sets for the long-slit spectra. These fits were conducted for a few lines, however, here we show the results for the line centered near 6600 $\AA$ as it is the closest to where we find the Hα line associated with our source.

Slit position	FWHM ($\AA$)	Velocity resolution (km s^{-1})
S1	0.82 ± 0.03	15.78 ± 0.53
S2	0.78 ± 0.05	15.12 ± 0.94
S3	0.79 ± 0.10	15.21 ± 2.00
S4	0.79 ± 0.05	15.16 ± 0.88
S5	0.81 ± 0.03	16.18 ± 0.50
S6	0.86 ± 0.02	17.14 ± 0.41

Table 4: *The FWHM and associated velocity resolution derived from a single Gaussian fit implemented on the emission line centered near 6600 Å. These values correspond to a resolution of around R ≈8000, which is the desired spectral resolution of our observational setup. These values are the median values along the entire slit.*

3.4 Tilted-ring modelling

The dynamics of a spiral galaxy can be described using a tilted-ring analysis where the assumption is made that the emission in the galaxy stems from and is confined to a thin disk and that the kinematics is dominated by circular rotation. A tilted-ring model details the kinematics of a galaxy by modelling the disk as a set of concentric rings of equal width but with each of them having a distinct radius r, inclination i, position angle PA, systemic velocity V_{sys}, center position (x_0,y_0) and rotational velocity V_{rot}. The radius is measured as the distance of the ring from the center position. The inclination of the galaxy is defined as the angle between the LOS of the observer and the vector perpendicular to the plane of the disk of the galaxy (90° being edge-on and 0° being face-on). The position angle is measured as the angle between North and the major-axis of the receding half of the galaxy. The systemic velocity of the galaxy is measured as the velocity of the dynamical center of the galaxy and the rotational velocity will be the calculated velocity of each concentric ring. This assumes that the gas follows completely circular orbits; meaning that we can describe the LOS velocity for any location (x,y) on a ring with radius R as:

$$V(x,y) = V_{sys} + V_{rot}(R)sin(i)cos(\theta) \tag{7}$$

The velocity *V(x,y)* is denoted in sky coordinates (x,y) and the right-hand side of the equation describes the dynamics in the disk coordinate frame (r,θ). These two systems are related to one another by:

$$cos(\theta) = \frac{-(x-x_0)\sin(PA) + (y-y_0)\cos(PA)}{r} \tag{8}$$

The basic approach of fitting a tilted-ring model to observational data is through the fitting of 2-dimensional velocity fields. The approach to applying this method to a velocity field is to fit Equation 7 using some sort of non-linear least-squares fitting technique. There are a number of programmes that offer this sort of analysis, most notably ROTCUR (Begeman, 1987), commonly found in data analysis packages GIPSY (van der Hulst et al., 1992) and NEMO (Teuben, 1995). The 2D approach has been further refined to some extent, with newer programmes such as RINGFIT (Simon et al., 2003) and DISKFIT (Spekkens and Sellwood, 2007) implementing different fitting techniques as well as adding higher order terms to the harmonic expansion which account for non-circular motions and asymmetries in the disk.

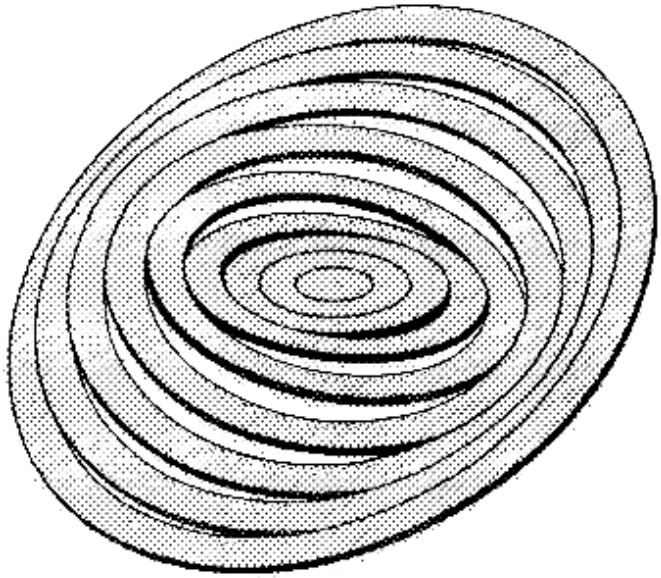

Figure 8: *A figure taken from Rogstad et al. (1974) depicting the geometry of a tilted-ring model used to originally model the kinematics of the spiral galaxy M83. This depicts the structure of the model consisting of a set of concentric rings with varying parameters of inclination and position angle.*

Although the 2D tilted-ring approach can prove to provide a reliable estimation of the overall kinematics of the disk (in that it can produce reasonable rotation curve for a galaxy) and is not computationally strenuous, it does come with a few pitfalls and drawbacks. One issue is that the 2D velocity field is not the entire data set for a given galaxy, but itself a product derived from the data cube for a given galaxy. This adds this intermediate analysis of having to extract the line profiles at each spatial pixel for a full data cube in order to create the velocity field upon which the model is applied. Furthermore, there are a couple of ways that a velocity field can be produced; such as fitting single or multiple Gaussian functions to the line profiles or using the intensity-weighted mean along the velocity axis. This inhomogeneity in producing velocity fields leads to deviations between data sets derived using different methods. The orientation of a given galaxy further induces uncertainty in derived velocity fields. If the line of sight of the observer penetrates the disk more than once, an unambiguous velocity field is unattainable. This is the case for nearly-edge on systems, galaxies with thick disks, warps or outer flares.

A major issue with deriving a tilted-ring model from a 2D velocity field is beam smearing (Bosma, 1978). This is an effect that results in the incorrect estimation of the gradient in a velocity field. Due to the beam being a finite size, the line emission from adjacent regions in the observation gets sampled which leads to smearing or blurring of the observed result. This causes the gradients in the velocity field to become shallower and the sampled emission line profiles to be broadened, supplying a false velocity dispersion value to the observer. This effect is most apparent in the innermost, denser regions of galaxies where the rotation curve appears to rise slower than its actual velocities. This is especially prominent in edge-on galaxies where the beam samples emission from many radii of the disk.

All of the aforementioned pitfalls of 2D tilted-ring modelling can be solved be applying a 3D tilted-ring model. The tilted-ring analysis was performed using 3DBarolo (3D Based Analysis of Rotating Objects from Line Observations) (Di Teodoro and Fraternali, 2015) which allows one to provide a FITS cube as an input and supply the initial values for the parameters to be optimized. Although there are a number of software that can perform this analysis, 3DBarolo is considered among the most up-to-date tilted-ring analysis programs as it can model the full data cube directly, thereby making full use of all the kinematic information contained within the data cube. Other tilted-ring analysis software of note are TiRiFiC (Tilted-ring Fitting Code) (Józsa et al., 2007) or FAT (Fully automated TiRiFiC) (Kamphuis et al., 2015) which allow for more complex kinematic modelling as they provide the means to add as many kinematic parameters as the user desires. However, our models consist purely of a thin disk through which we describe the kinematic behaviour of the HI gas and can infer any further connections between this and the ionised gas.

3.4.1 3DBarolo

3DBarolo works by supplying a 3-dimensional FITS cube, having 2 spatial dimensions and 1 spectral dimension, as an input and then constructs a number of artificial 3D models to be directly compared with the observational cube. 3DBarolo's `3DFIT` task was used to build a three-dimensional tilted-ring model from the HI cube which uses a stochastic function that randomly populates the space with gaseous clouds of emission for which emission-line profiles are constructed. Each ring is built from the set of parameters which include:

- *NRADII*. The number of concentric rings used to build the model.
- *RADSEP*. The width of each concentric ring.
- *(Xpos, Ypos)*. The coordinates of the central pixel in the cube.
- *Vsys*. The systemic velocity of the galaxy.
- i. The inclination angle of the galaxy.
- ϕ. The position angle of the receding side of the galaxy measured from North.
- *Vrot*. The rotational velocity.
- *Vdisp*. The velocity dispersion of the gas.
- Z_0. The scale-height of the gas layer.

These quantities can vary from ring to ring, however, we keep the number of concentric rings, the width of each concentric ring, the center coordinates and the systemic velocity at fixed values. In an initial fit, these quantities were free parameters as 3DBarolo is equipped with a functionality that can reasonably estimate these values from the data without supplying initial guesses. Upon keeping these values free, the median value for the sysemic velocity and center positions were taken as the fixed value for each quantity to be used in the modelling procedure.

The width of each concentric ring is by default $BMAJ/2$, i.e half the size of the major-axis of the beam and number of concentric rings in the model is determined by the extent of the emission. We leave these parameters free in order to determine the radial extent of the emission in the galaxy, after which we fix these values with *RADSEP* being equal to the *BMAJ* value indicated by the header. Furthermore, the scale height h was determined by investigating the flux distribution as a function of distance from the midplane of the galaxy by taking a projection of the intensities perpendicular to the major-axis of the galaxy. This distribution follows the trend of a decaying exponential and was fitted with the function:

$$I(z) = I_0 e^{\frac{-z}{h}} \tag{9}$$

where *I(z)* is the intensity function that changes with distance, z, from the midplane. The parameters optimized in this fit are I_0 and h, which are the intensity at the disk of the galaxy and the scale height of the disk respectively. The remaining parameters, *Vrot*, *Vdisp*, *PA* and i are all kept as free parameters in an initial fit for a tilted-ring model of the disk. For all of the fits, a $|\cos\theta|$ weighting was used since positions nearer to the major-axis of the galaxy contain more rotational information as opposed to those near the minor-axis.

The main algorithm of 3DBarolo is described and characterized by four main steps: (1) Disk model. The model is constructed through a Monte-Carlo reproduction of the gas distribution of the data cube in both the spatial and velocity domain. (2) *Convolution*. The model is smoothed such that it matches the spatial resolution of the data by convolving it with a 2D Gaussian representative of the observational Point Spread Function (PSF). (3) *Normalization*. The model is normalized to the moment 0 map of the observational cube. (4) *Residuals*. A pixel-by-pixel comparison between the model and data after which the sum of the residuals is returned to the minimization algorithm.

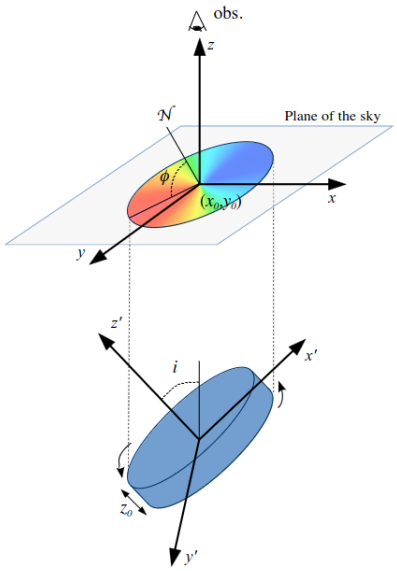

Figure 9: *A figure taken from Di Teodoro and Fraternali (2015) depicting the geometric parameters of the disk model by displaying the disk in the x', y', z' space projected into an ellipse in the xy plane of the sky.*

3.5 Position-velocity diagrams

Position-velocity (PV) diagrams are powerful tools in visualising and understanding the kinematic behaviour of galactic disks. This is especially true in the context of HI data as it provides a representation of the gas at different radii and rotational velocity. They are typically constructed by extracting a two-dimensional slice which covers the spatial extent of the galaxy along its kinematic major-axis whereby the observed velocity is plotted on the y-axis as a function of the angular distance on the x-axis. The PV-diagrams in this work were constructed using the Python package `PVextractor`. At a glance, a PV diagram provides the rough structure of the rotation curve of the galaxy. PV diagrams offer valuable information on physical properties of the gas and the underlying galactic disk as it allows one to assess whether there are any structural asymmetries in the system and how this affects the kinematics of the galaxy. In addition to this, it allows us to identify any signatures of extraplanar gas or lagging emission which presents itself as the commonly referred to 'beard gas' in a PV diagram (Sancisi et al., 2001). This is indicated by emission tending toward the systemic velocity of the system and presents itself by extended emission at lower velocities on the receding side and higher velocities on the approaching side relative to the bulk rotational velocity. PV diagrams constructed parallel to the major axis allows for one to determine whether there are changes in azimuthal velocity as a function of height above the midplane in moderate or highly inclined galaxies.

3.6 Moment Maps

A vital asset in visualising radio data of galaxies is by utilising moment maps. The moment maps used in this analysis are the Moment 0, Moment 1 and Moment 2 maps. The Moment 0 map is the total intensity map integrated over the entire cube and is defined as:

$$Moment \quad 0 = \sum_j S_{v,j} \times \Delta v \tag{10}$$

where $S_{v,j}$ is the total HI emission in the j-channel and $\Delta\ v$ is the velocity resolution of the cube. The moment 0 map proves to be useful as it provides one with the tools to identify pixels with emission at a glance. The moment 1 map involves taking the intensity-weighted mean along the velocity axis in the data cube.

$$Moment \quad 1 = \frac{\Sigma_j v_j S_{v,j} \times \Delta v}{\Sigma_j S_{v,j} \times \Delta v} \tag{11}$$

where v_j is the velocity of the j-th channel. The moment 2 map represents the velocity dispersion in the profiles and is defined as:

$$Moment \quad 2 = \sqrt{\frac{\Sigma_j (v_j - v_{\rm mean})^2 S_{v,j} \times \Delta v}{\Sigma_j S_{v,j} \times \Delta v}} \tag{12}$$

where v_{mean} is the mean velocity corresponding to the velocity channel v_j.

3.7 Gaussian decomposition of HI profiles

A commonly adopted method to separate anomalous gas from the regularly rotating disk gas in galaxies is described by Marasco et al. (2019) which further refines the technique described by Fraternali et al. (2002). This method works under the assumption that the velocity profiles can be described by a Gaussian distribution with an extended tail of emission which is skewed toward the systemic velocity of the system. If the galactic disk is relatively thin, the resolution of the data is considered reasonably good and the inclination of the system is not extreme ($i \leq 80$), then the assumption made is that the profiles are broadened only by turbulent motions in the gas. This is depicted in Figure (10).

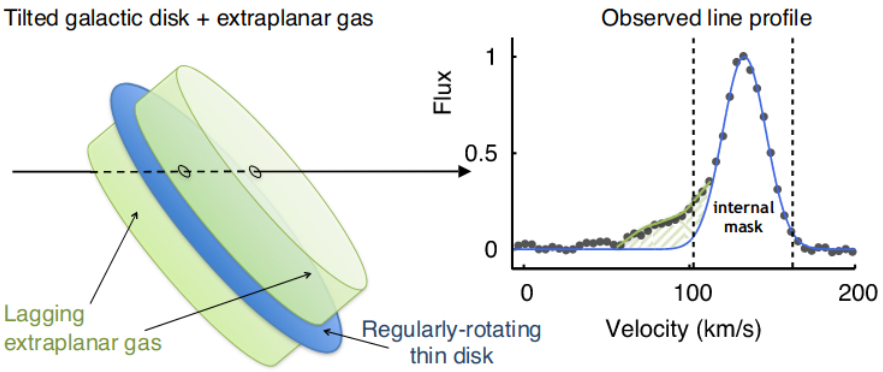

Figure 10: *A figure taken from Marasco et al., 2019 depicting how a LOS samples emission from a regularly rotating thin disk as well as the lagging extraplanar gas associated with it. The result is a Gaussian profile with broadened wings of emission shown on the right hand side of the image where the presence of a slowly rotating component is indicated by the velocities between* $\approx$ *50 km/s and 120 km/s*

The approach adopted in Marasco et al. (2019) is to fit a single Gaussian to the profile and then filter out emission where the fit has a high SNR which is shown by the vertical dashed lines in Figure (10). Profiles with a peak that satisfy a SNR of 4 are selected and a Gaussian is fit to the upper 40% section of the profile. This Gaussian component is believed to be the contribution from the disk alone and all the other emission is attributed to the extraplanar gas. This procedure, however, has been found to prove well-suited for galaxies with an intermediate inclination and observed high spatial resolution where the effects of beam-smearing do not alter the geometry of the line profile.

We use a similar procedure to separate the components in our data, by incorporating a similar methodology described in the fitting of the optical emission lines. It works primarily under the assumption that the profiles either consist of one or a maximum of two components where we consider the profiles as the superposition of profiles from the thin disk and the diffuse HI in the galaxy. It must be emphasised that our system is an edge-on galaxy, and the projection effects are maximized for this type of orientation of the galaxy. Thus, when assessing a profile through a LOS which penetrates the disk, it is not entirely clear whether the diffuse component is attributed to diffuse gas in the disk or whether it is the extraplanar gas that encompasses the so-called 'edges' of the galaxy which can be interpreted as the gas in front or behind the thin disk with respect to the observer.

The approach adopted in this work involves fitting the profile with a single Gaussian function and estimating initial guesses for the optimisation of these parameters. However, this approach does not always conventionally work for the HI velocity profiles largely due to the increased complexity in these profiles compared the the Hα profiles. Largely due to the HI existing as a more ubiquitous gaseous emission found at larger extents from the disk as opposed to Hα which presents itself more along the lines of 'pockets' of emission throughout the galaxy. Upon a visual comparison of the Hα and HI profiles, there were more possible geometries in the HI lines. Thus, we change our fitting procedure by using a Markov-Chain Monte-Carlo method to best estimate our initial guesses and then supply these guesses for our least-squares minimisation.

The MCMC-method used here involves initially supplying an initial guess for the parameters of the double Gaussian function to be fitted. The validity of this guess as a result for the best fit parameters is assessed by a probability criterion and a new set of parameters is estimated within the allowed ranges. Whether this new initial guess is favoured over the previous result is determined using a consequence of Bayes theorem:

$$P(\theta|D) = \frac{P(D|\theta)P(\theta)}{P(D)} \tag{13}$$

Equation (13) describes the posterior probability (P(θ|D)) by rearranging Bayes theorem and writing it as an expression defined by the likelihood (P(D|θ)), the prior (P(θ) and the evidence (P(D)). The likelihood is defined as the probability given our model, the prior is defined as the probability of our model and the evidence is considered the probability of the data.

We use the `emcee.EnsembleSampler` class from the Python `emcee` library to perform this analysis. Within this sampler, we define the number of walkers exploring the parameter space, the dimensions of the parameter space, the initial positions of the walkers and the log-posterior function which acts as a guide in exploring the parameter space. For the initial positions of our walkers, we adopt the approach that assumes the emission line presents itself as a superposition of two Gaussian functions where one represents the diffuse gas while the other function is a consequence of the HI in the disk of the galaxy. Using this fitting procedure, we can explore a more robust parameter space and probe a greater variety of geometries that may be present in the emission lines.Due to the physical nature of HI and how extended it can be from the disk of the galaxy, exploring a greater parameter space using this fitting procedure allows for a more robust approximation of the components inherent in the HI emission lines.

To ensure validity of assuming the presence of two components, a SNR cut-off was applied similar to the procedure followed in fitting the optical emission lines. Here, the noise is estimated in the same way by taking the standard deviation in the velocity profile within a region of no emission. Then, both of the amplitudes of the fitted components needed to exceed a 3σ noise value. In velocity profiles where one or both of the components failed to satisfy this condition, a single Gaussian function was fitted which also needed to surpass this criterion.

3.8 Envelope-tracing method

If we are provided with the position-velocity diagram along the major-axis of an edge-on galaxy, we can derive the rotation curve along this axis using the envelope-tracing method (Sofue, 1996). The rotation curve is derived by using the terminal velocity V_t in the position-velocity diagram. The terminal velocity is defined as the intensity at which the intensity becomes equal to

$$I_t = [(\eta I_{max})^2 + I_{lc}^2]^{\frac{1}{2}} \tag{14}$$

on observed position-velocity diagrams. In equation (14), I_t and I_{lc} are the intensities corresponding to the maximum and lowest contour levels of intensity where the value for I_{lc} is typically assumed to be at the 3σ level. η is a constant usually taken in the range of 0.2-0.5; $\eta = 0.2$ defines a 20% level of the intensity profile at a fixed position.
The rotation velocity (V_{rot}) at a given radius from the galactic centre is derived from the terminal velocity (V_t) at that position by the relation

$$V_{rot} = \frac{V_t - V_{sys}}{\sin i} - (\sigma_{obs}^2 + \sigma_{ISM}^2)^{\frac{1}{2}} \tag{15}$$

with V_{sys} corresponding to the systemic velocity, i the inclination angle, σ_{obs} instrumental velocity resolution and σ_{ISM} the velocity dispersion of the interstellar medium.
When dealing with edge-on spiral galaxies, they often tend to be unresolved along their minor axis (Kregel and van der Kruit, 2004). When a single beam observes part of the galaxy, it samples the kinematics and gas density across a large range of galactrocentric radius. All of this information regarding the kinematics and gas density is concentrated in a position-velocity diagram.

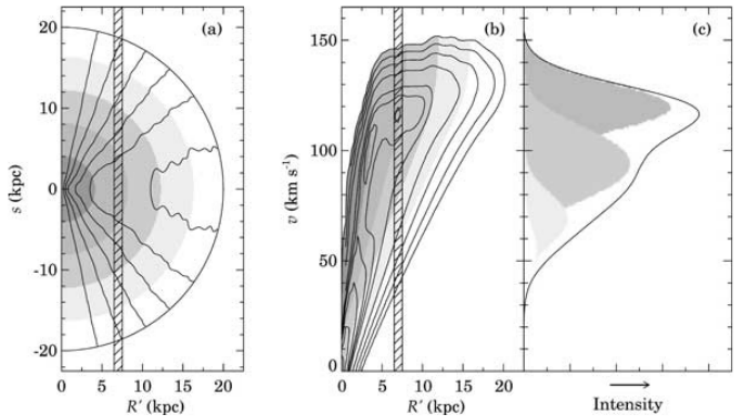

Figure 11: *A mapping of the kinematics and gas density on the position-velocity plane depicted for a simulated edge-on view of the HI distribution in the spiral galaxy NGC 2403 (Kregel and van der Kruit, 2004). (a) The beam samples many galactrocentric radii along a (LOS). (b) The LOS intercepting many velocities depicted on the PV-diagram of the galaxy. The greyscale indicates the rings in the plane of the disk from which the HI stems from. (c) The velocity profile at a radius of 7 kpc sampled from the LOS. The greyscale highlights the contributions from the many rings to the total velocity profile.*

Figure (11) portrays the importance of using the envelope-tracing method as a means of mitigating the projection effects in the kinematics of the disk. The galactic disk consists of a set of concentric rings with distinct gas densities. In an edge-on system, the LOS is depicted as the dashed vertical line shown in Figure (11). Due to the circular rotation of the galaxy, the innermost ring has its velocity vector parallel to the LOS, its projection is maximized. Thus, in frame (c) of Figure (11), the contributions from the innermost ring are shown in the darkest shaded region in the velocity profile and the contributions from other components in the LOS are shown in the lighter shaded regions.

The algorithm used to apply the envelope-tracing method is as follows: (1) Extract the velocity profile along a spatial position indicated on the PV-diagram. (2) Fit the peak of the extreme velocity side, i.e. the peak furthest from the systemic velocity.(3) Fit the remaining part of the profile with a Gaussian function.(4) Extract the velocity corresponding to greatest peak as the velocity of the main disk component at that spatial position. (5) Work through the entire PV-diagram and build up a rotation curve with the velocities at distances away from the center of the galaxy. The velocities here are the terminal velocities, therefore applying Equation (15) allows us to obtain the rotation velocity of the gas.

There is a slight complication to this method which is introduced by the fact that that HI in the velocity profiles is not solely due to the HI at the line of nodes. The extraplanar gas associated with an edge-on galaxy encompasses the entirety of the galaxy in the 3-dimensional space. This implies that our LOS penetrates through potential EPG layers residing in front or behind the galaxy relative to us. Thus, the envelope can possess emission from high-velocity tails of HI which can cause the resulting profile to stray from an exact Gaussian tail with a velocity dispersion inherent in the gas we aim to probe (Olling, 1996).

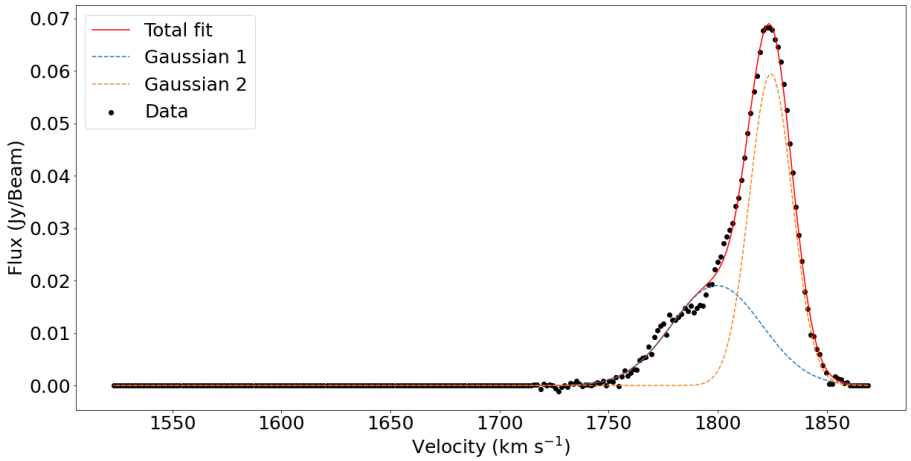

Figure 12: *An example of a velocity profile extracted along the major-axis for the HI cube of UGCA 250. This shows the contribution from the projection effects which presents itself as a broader component tending toward the systemic velocity.*

4 Results

4.1 Optical Data

4.1.1 Rotation curves

The rotation curves were derived through using both the aforementioned single Gaussian as well as the double Gaussian fits on the Hα line.

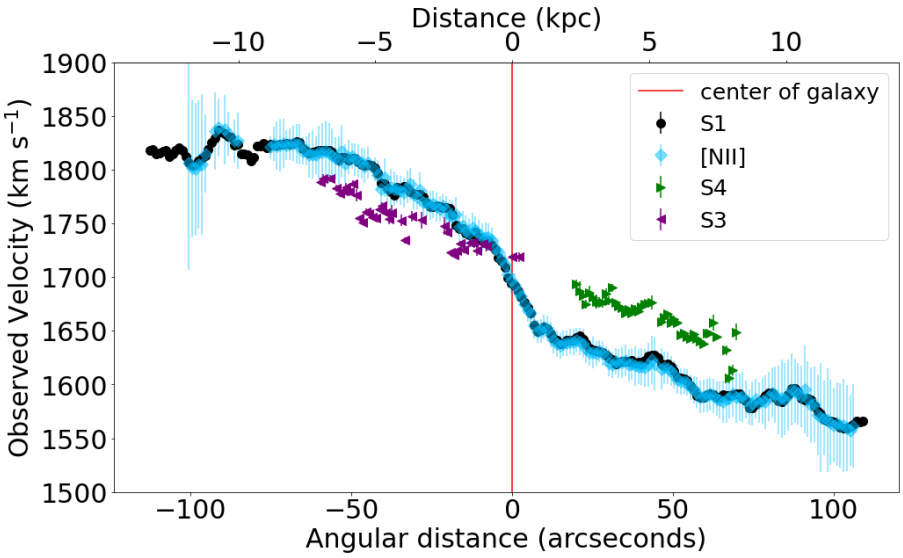

Figure 13: *The single Gaussian fit rotation curve along the major-axis (S1) of the galaxy is shown here in the black data points. The purple symbols are the top slice (S3) and the green symbols are the down slice (S4) which are the slits above and below the galaxy respectively. The [NII] rotation curve is overlaid with the blue data points. The uncertainties on the rotation velocities along the major-axis are relatively small.*

The derived rotation curve along the major-axis of the galaxy in Figure (13) exhibits the expected shape of a rotation curve for a spiral galaxy. The velocities increase as we move further away from the center of the disk and flatten out toward the edges, as one would expect from a rotating spiral galaxy. The systemic velocity was derived by assuming that the maximum intensity along the slit corresponds to the center of the galaxy. Using this assumption, the systemic velocity was found to be 1694.18 ± 14.03 km s^{-1} which is in agreement with previous studies and with the information presented in Table (1). The rotation curve derived with Hα and the one derived from [NII] are in good agreement with each other, displaying the same kinematic trend throughout the galaxy.
The contribution from the observation just below the disk, the down slice, only appears to sample emission from the approaching side of the galaxy. The same can be said for the top slice only contributing to the receding side of the galaxy. This comes as a result of the lopsidedness of the disk of ionised gas. Figure (4) shows that each of these slits only coincide with a portion of the disk while the shape is warped and no emission is detected by the top slice for the approaching side and the down slice for the receding side. In addition to this asymmetry, there appears to be asymmetry in the kinematics of the disk as well. The receding side of the galaxy seems to flatten out more and reach a plateau at the edge of emission while the approaching side still exhibits a slight gradient on the outskirts.

The kinematics of the ionised gas just above and below the disk compared to the gas within the disk indicates a velocity difference. Fraternali et al. (2004) and Heald et al. (2007) showed that eDIG layers can be characterised by a lagging rotation with respect to the gas in the disk. This behaviour is exhibited by the off-axis rotation curves which have velocities tending more toward the systemic velocity with respect to the gas in the disk. This 'lag' is similar for both regions off the disk with a velocity difference between this gas and the disk-gas being 22.58 km s^{-1} and 23.29 km s^{-1} for the regions below and above the disk respectively. The difference in distance between each of the parallel slits and the major-axis slit is 13.7" which correlates to a physical scale of about 1.6 kpc. Thus, each off-axis slit is observing gas at a distance of 1.6 kpc from the gas observed by the major-axis observation which resides in the main disk. Since we assumed a singular thin disk with a scale height of 0.49 kpc, these slits may be probing regions of ionised gas off of the main disk of the galaxy, constituted by eDIG.

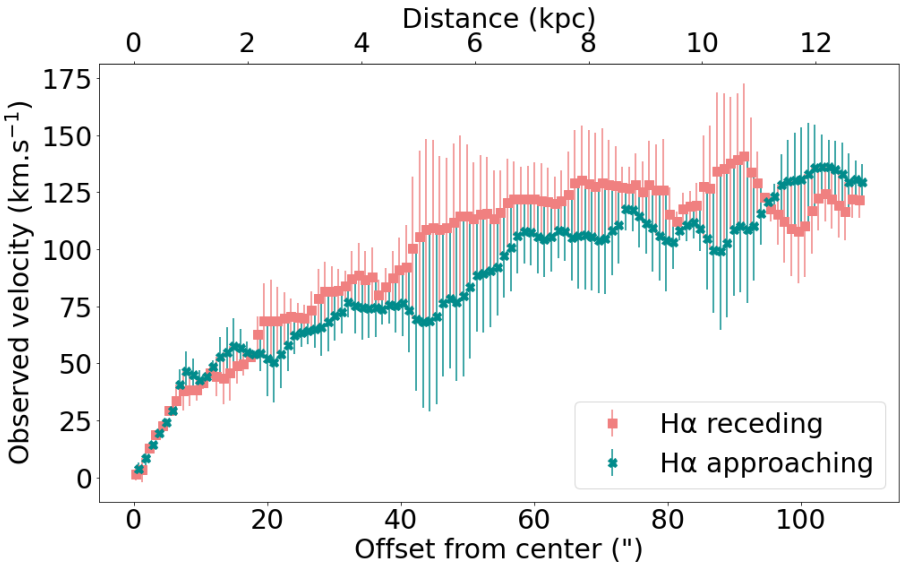

Figure 14: *The single Gaussian fit rotation curve along the major-axis for both the approaching and receding side of the galaxy. The associated uncertainties are taken as the difference between the velocities of each curve. The median associated error is 13.67 km s^{-1}.*

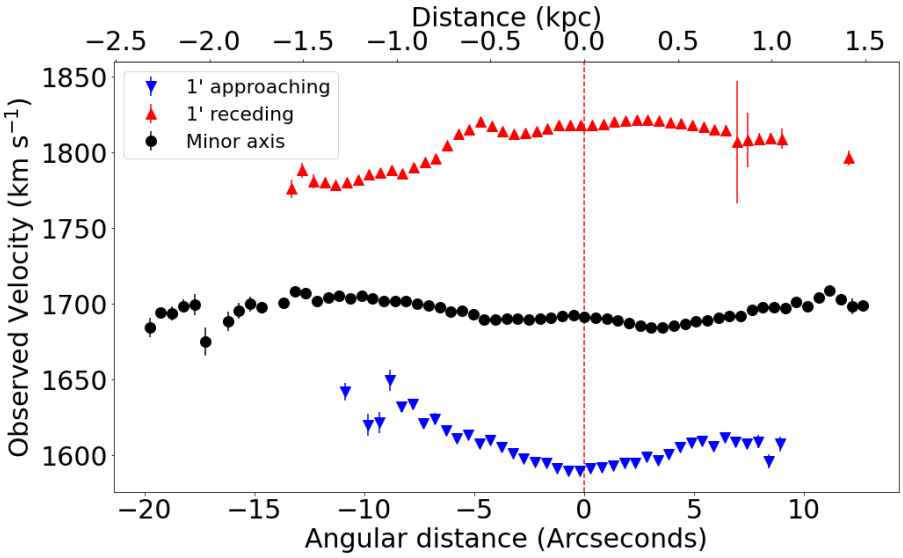

Figure 15: *The single Gaussian fit rotation curve along the minor-axis (S2) of the galaxy shown with the rotation curves derived for the long-slit observations placed parallel to the minor-axis at 1' toward the receding side (S6) and 1' toward the approaching side (S5) of the galaxy.*

The rotation velocities along the minor-axis in Figure (15) is mostly flat, as expected, and is distributed about the systemic velocity of the galaxy. This property is somewhat attained in the rotation curves for the off-axis minor-axis observations, however, the velocities deviate as we extend further from the disk. Each of the parallel slits are situated at 60" from the minor-axis which corresponds to a physical separation of 7.04 kpc. In the outer regions of these curves, the velocities tend more toward the systemic velocity. Within 0.5 kpc of either side of the disk, however, the rotation curve along the approaching side shows this behaviour with the velocities slightly moving toward the systemic velocity. The receding side rotation curve is generally flat in this region, but the velocities move toward the systemic velocities beyond 0.5 kpc on the LHS and continue this trend until about 1.5 kpc from the disk. This indicates a kinematic lag the gas layers at greater perpendicular distances from the disk which exceeds the scale height of the disk. Furthermore, the velocities in Figure (15) agree with the velocities along the major axis at 60" from the center of the galaxy as shown in Figure (13). As we extend greater distances from the disk, both of the offset rotation curves along the minor axis exhibit the same trend of tending toward the systemic velocity. We notice this by the increasing velocity in the blue rotation curve and the decreasing velocities in the red rotation curve in Figure (15) respectively.

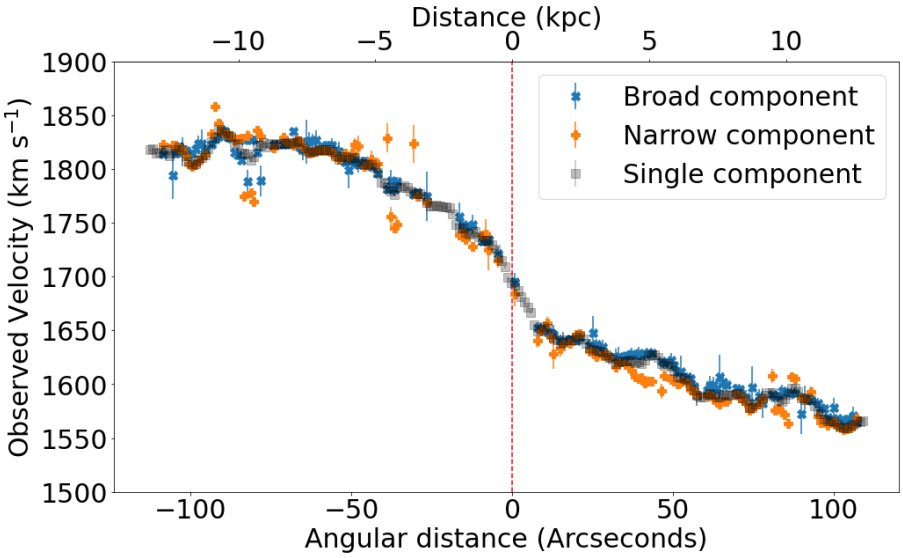

Figure 16: *The rotation curve along the major-axis of the galaxy derived using the 2-component Gaussian fits on the Hα line. The rotation curves displayed in this figure are that of the narrow (orange) and broad (blue) components in the fits along with the rotation curve derived from the single-component fits (black).*

Figure (16) depicts the rotation curve of the galaxy by decomposing the Hα line into broad and narrow components. If the broad components were constituted only by eDIG and the narrow components attributed to dense HII regions, one would expect the narrow components to be dominated by the rotation of the disk and the broad components tending more toward to the systemic velocity. On the approaching side of the galaxy, this trend appears to be more apparent with a steadily lagging broad component relative to the velocities of the narrow component in this region. The median velocity difference between the narrow and broad components here is 8.94 km s^{-1}, indicating a diffuse component with a slight lag.

In the regions closer to the center of the disk, the narrow and broad components appear to follow the same trend and the differences in their kinematics are minimal. On the receding side of the galaxy, we largely see variation between whether the broad or narrow component lags with respect to the other. This can be consistent with the broad component being constituted by planar diffuse ionised gas (pDIG) in the disk, thus both components follow the rotation of the disk and neither provides conclusive attributes of lagging gas associated with eDIG. However, as we extend out to the furthest regions on the receding side, we see a slight deviation in what one would expect from the kinematics of a diffuse gaseous component. It must be reiterated that this galaxy is warped in the outer regions, resulting in the long-slit observations perhaps probing more of the eDIG on the approaching side and more pDIG on the receding side.

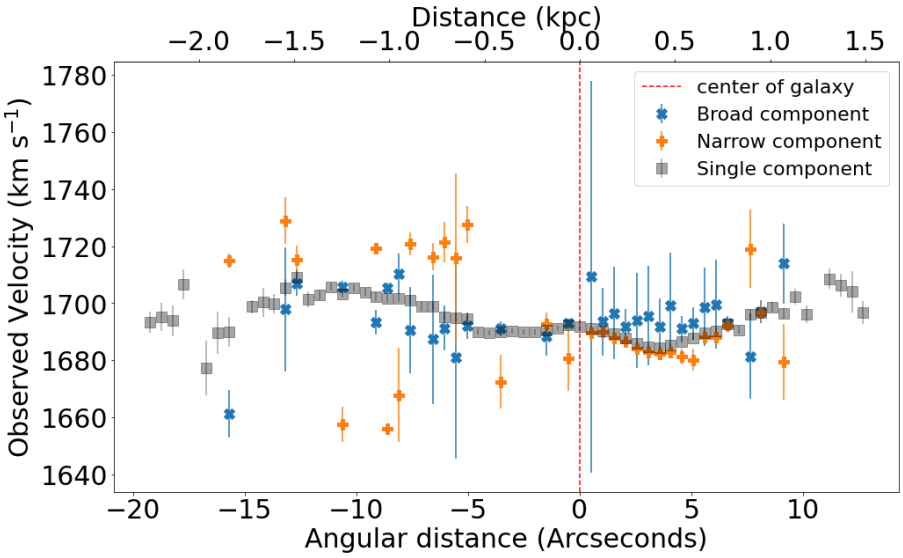

Figure 17: *The two-component minor-axis rotation curve represented by the broad and narrow components along with the single-component rotation curve plotted in the black data points.*

The two-component minor-axis rotation curve is shown in Figure (17) with all of the velocities near the systemic velocity. On either side of the galaxy, we see that the velocities of the broad and narrow components differ with the broad components having slightly higher velocities above the disk and lower velocities below the disk. This trend is consistent on either side of the galaxy, but appears more pronounced below the galaxy as the separation between the broad and narrow component velocities appear greater on the LHS (left-hand side) as opposed to the RHS (right-hand side) of Figure (17). From this figure, it is also evident that the narrow components are more analogous to the velocities of the single component rotation curve, reinforcing the claim that the narrow components trace to the HII regions in the disk and the broad components are attributed to the diffuse gas. The similarities between the narrow and single components are more prominent on the RHS of the figure, with the single component velocities lying between that of the broad and narrow components in the region of -5" to -15". They do, however, tend more toward the velocities of the narrow components.

Further from the disk, there is a greater difference in the respective broad and narrow components beyond -10" as opposed to the velocities within -10" and 5", showing that the apparent lag is greater further from the disk. Layers of eDIG are characterised by differential rotation where layers further out from the disk tend to rotate slower than those closer to the disk. On the LHS of Figure (17), the lagging component of gas is consistently the broad component. This suggests that this broad component could indeed be a consequence of diffuse gas. The high inclination of this galaxy presents the challenge of not knowing exactly whether what we see could be projection effects instead of a lagging gaseous component off the disk. For example, between 0" and 5", this could be a region in the face of the galaxy being probed as opposed to a region slightly off of the disk. This does, however, provide a stronger case for the presence of eDIG as we see a consistently lagging diffuse component of gas on either side of the galaxy. However, since the uncertainties on the broad component velocities are large, it could be that the slit is not only probing the minor-axis of the galaxy.

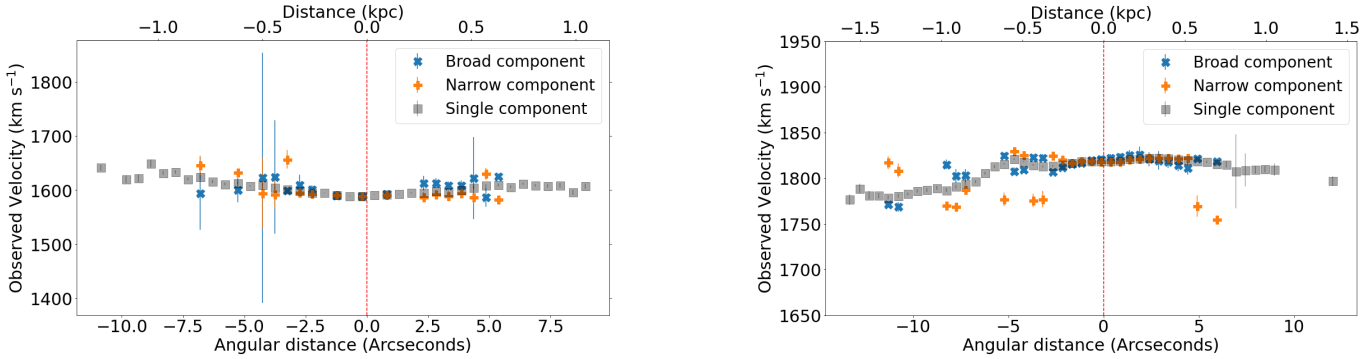

Figure 18: *The two-component minor-axis rotation curves for slits S5 (a) and S6 (b) relating to the approaching and receding side of the galaxy respectively along with their respective single component rotation curves.*

In Figure (15) we see the trend that the velocities further from the disk tend more toward the systemic velocity of the galaxy for the off-axis rotation curves along the minor-axis of the galaxy. For the two-component rotation curves in Figure (18) this behaviour is mimicked but is more prevalent in the kinematics of one component with respect to the other at the same spatial position. One would expect that the component attributed to the diffuse gas would be the one to exhibit this, however, this is not always the case here. This is largely true, in Figure (18 (a)) the broad components tend more toward the systemic velocity than the narrow components in the region between -4" and 4" and that the narrow components have velocities more comparable to the single component velocities within this region. In the outer parts, this trend is not consistent and there are instances where the narrow component has a velocity closer to the systemic velocity than the respective broad component.

Similarly in Figure (18 (b)), the narrow components follow the trend in velocity of the single component fits more closely than the broad component velocities. We also see a component tending more toward the systemic velocity as we extend from the disk. The inconsistency is also apparent here as it is not always the broad component exhibiting this kinematic lag. Due to the variability as to which component exhibits this kinematic lag, this can not be attributed to the presence of eDIG. The separation between the velocities of the components in the outskirts are larger than those within the inner regions, showing that the lag is differential similar to the kinematics displayed along the minor-axis in Figure (17). Comparing the kinematics of the broad and narrow components from these three slit positions along the minor-axis does not show concrete evidence for a lagging gaseous component present in all three data sets with kinematics characteristic of an eDIG layer.

4.1.2 Flux ratios

Assessing the flux ratios of forbidden emission lines with Hα provides information on the chemical abundances as well as the ionisation mechanisms in the regions being probed. Here, we examine the ratio of [NII]/Hα as a function of distance.

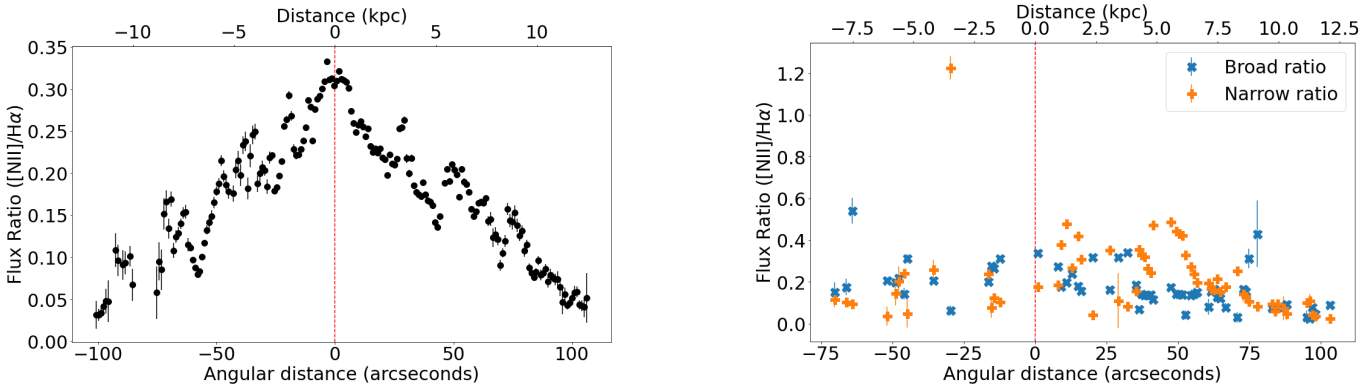

Figure 19: *The flux ratios of [NII]/Hα along the major-axis as a function of angular distance. Plot (a) shows the ratio calculated from the single Gaussian fits while (b) shows the ratios of the two-component Gaussian fits.*

Figure (19 (a)) shows that the ratio of [NII]/Hα increases toward the center when assessing the distribution from either end of the galaxy. The ratio reaches a maximum value of 0.33 ± 0.01 toward the center of the galaxy and decreases away from the center reaching values of 0.04 ± 0.02 in the most outer regions. This trend is expected as majority of the matter and the most chemically enriched gas is concentrated toward the center of the galaxy. In the outer regions, we probe more regions associated with the spiral arms of the galaxy which are associated with HII regions, this is shown by a declining ratio away from the center indicating a greater presence of Hα. The flux ratios in Figure (19 (a)) do not provide any evidence for eDIG, instead it could be an indication that the metallicity is dominating the [NII]/Hα ratios.

Figure (19 (b)) shows that neither the broad nor the narrow flux ratios ever reach unity and that they never exceed a ratio of 0.6. This is true except for one outlier on the LHS of the plot. Apart from this value, these ratios suggest that the Hα flux dominates the flux ratios throughout the galaxy. From this figure, we can not deduce a distinct trend as to how the ratios differ with respect to different locations in the galaxy. There are, however, regions in which the narrow ratio exceeds the broad ratio as well as regions where the converse is true. This could suggest the greater presence of diffuse gas in the disk compared to the HII regions. However, this could also be a consequence of the challenges faced when dealing with an edge-on galaxy where one complication could be that we are actually tracing the presence of gas in the halo in the foreground of the disk with respect to the observer. Furthermore, there could be multiple 'narrow components' present in the emission line due to the LOS sampling emission from multiple HII regions due to the high inclination.

The value in assessing the trend in the distribution of the flux ratios of [NII]/Hα is of greater worth as a means of probing for eDIG when studying the trend along the minor axis of the galaxy since we can deduce whether the ratio is enhanced as a function of distance from the midplane of the galaxy. Here, we look at the trend along the minor-axis of the galaxy as well as at 1' offsets parallel to the minor-axis in both the directions of the receding and approaching side of the galaxy.

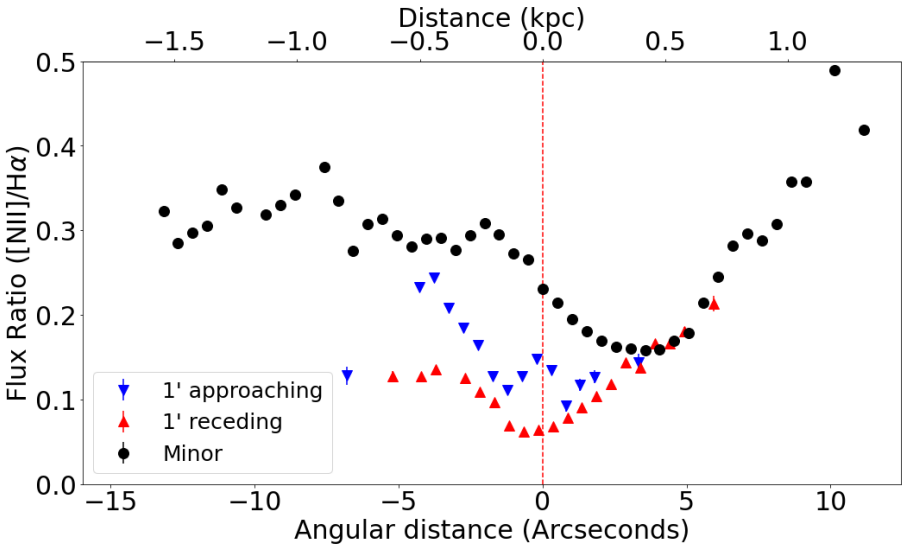

Figure 20: *The flux ratios along the minor axis of UGCA 250. The points in black are along the minor-axis, the points in red are from the long-slit observation offset at 1' parallel to the minor-axis in the direction of the receding side of the galaxy and the points in blue are from the long-slit observation offset at 1' parallel to the minor-axis in the direction of the approaching side of the galaxy. The errorbars in this plot are small.*

An immediate result from looking at the distribution of flux ratios in Figure (20) is the asymmetry along the minor-axis of the galaxy. There is a disparity in the increase of flux ratios on either side of the galaxy, with the values on the right-hand side (RHS) first declining before undergoing an increase while the value on the left-hand side (LHS) seem to largely exhibit a gradual increase as we extend further from the disk. At the most distant regions from the disk, at about 10", we see the ratios reaching values of about ≈ 0.4. This indicates that Hα is still dominant over [NII] and this ratio never reaches unity, however, it is the change in the value with distance as opposed to the actual values that indicate the presence of eDIG. Furthermore, the dip in ratio values on the RHS of the minor-axis ratios can be attributed to the inclination of the galaxy. Since the galaxy is highly inclined (i=74.9°), it could be that the central regions of the disk are being probed in this region on the plot. If this is the case, then it would mean that the increase in values occurs where the LOS penetrates the gas not residing in the galactic disk.

The ratios of the offset minor-axis observations are lower than that of the minor-axis along the entire spatial axis. This could be due to the more chemically enriched and higher gas content concentrated toward the center of the galaxy, with a higher flux value in both the [NII] and Hα emission lines in this area. Although these ratios are consistently lower than those seen along the minor-axis of the galaxy, we do see the red data points increase with distance as we extend from the disk, providing indication as to the presence of eDIG on the receding side of the galaxy. This trend, however, is not mimicked by the blue data points. We do not see a smooth increase with distance, but rather a relatively consistent ratio value as we move along this slit position. This reinforces the idea of asymmetry in the disk of the galaxy, as we do not see the same behaviour in the ratios of ionised gas on either side of the galaxy.

The two-component flux ratios along the minor-axis in Figure (21) have values comparable to the single component ratios with majority of the ratio measurements lying in the range of $0.2 \leq$ [NII]/H$\alpha \leq 0.4$. The ratios between the 0" and 5" lie closer together than the ratios measured further out from the disk. A strong indicator of eDIG would be an increasing trend seen in the broad component ratios with distance from the disk accompanied by relatively lower narrow component ratios. This would indicate that the diffuse gas is dominant in these outer regions. This trend is noticeable on the LHS of Figure (21) where there are a few data points with broad component ratios consistently higher than the narrow component ratios at the same spatial position while gradually increasing in value. This, however, is not entirely consistent as there are narrow component ratios higher than the broad component ratios away from the disk. Most noticeably, the values on the edge of the plot on either side of the galaxy have narrow component ratios much higher than the broad component ratios. An explanation for this could be a product of the fit performed on these profiles where the broad component present in the [NII] line is not as defined as the associated component in the Hα line, resulting in a small ratio value. Despite these values, the increasing trend of the broad ratios on the LHS could be indicative of the presence of eDIG. This presence of higher ratios on the LHS compared to the RHS is similar to the distribution of the ratios of the single components in Figure (20) along the minor-axis.

Figures (22) and (23) do not show the explicit trend in the enhancement of [NII]/Hα with distance from the midplane. In the fits performed to obtain these two ratio plots, the SNR condition that the amplitudes of both Gaussian functions in the [NII] line was altered from an SNR of 3 to 1 due to the inability of a fit to be obtained under the prior condition. In Figure (22) there is no distinct pattern in the way that the ratios behave on either side of the disk, however, there is a consistently greater value in the broad component ratios in the ratios on the RHS of Figure (23). These ratios are still within a distance of 0.5 kpc from the midplane and our assumed scale height was 0.49, therefore strong conclusions can not be made as to whether these ratios can be attributed to the presence of eDIG.

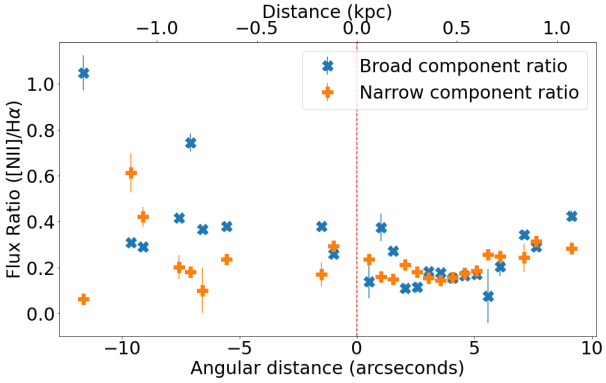

Figure 21: *The two-component flux ratios of [NII]/Hα as a function of distance from the galactic disk along the minor-axis of the galaxy.*

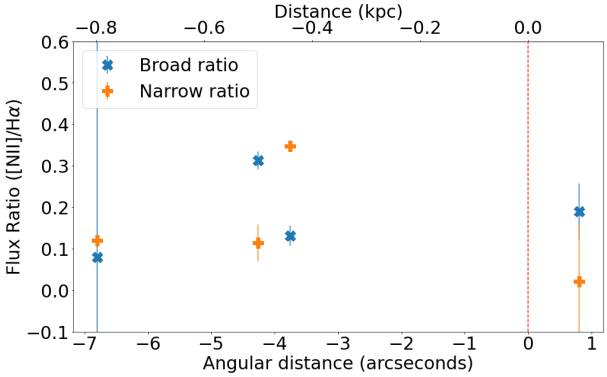

Figure 22: *The two-component flux ratios of [NII]/Hα as a function of distance from the galactic disk along slit S5 of the galaxy.*

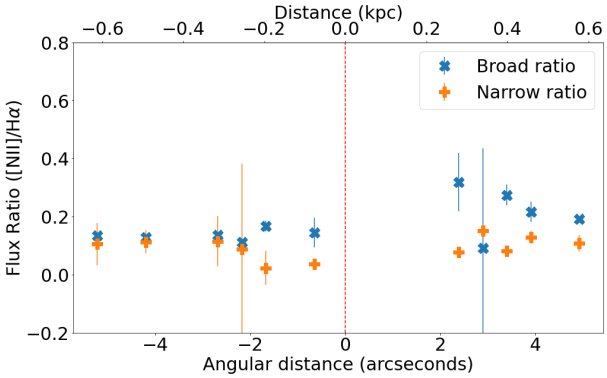

Figure 23: *The two-component flux ratios of [NII]/Hα as a function of distance from the galactic disk along slit S6 of the galaxy.*

4.1.3 Velocity dispersions

The velocity dispersions reported here are taken as the observed velocity dispersion of the fitted Gaussian functions to the Hα emission line.

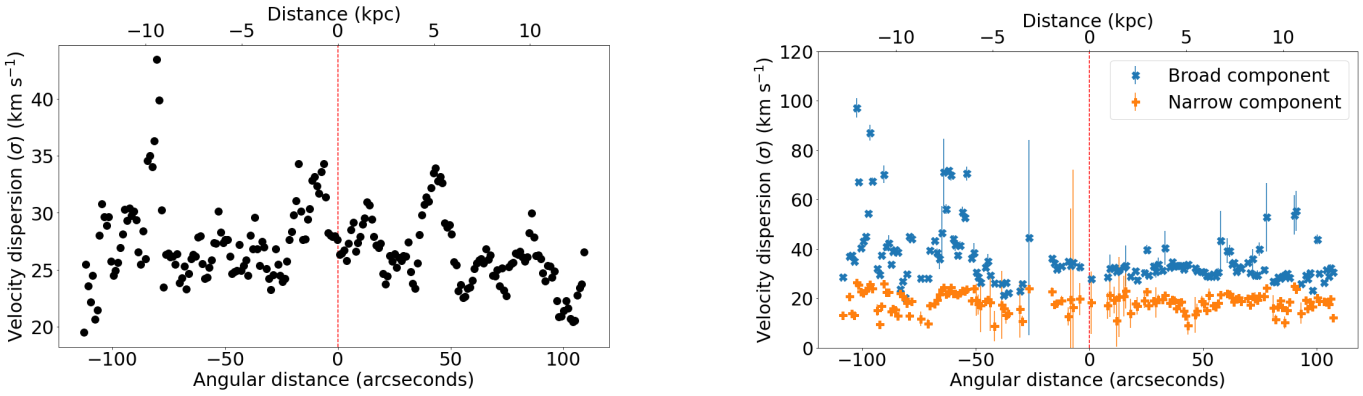

(a) (b)

Figure 24: *The velocity dispersions of Hα for the single Gaussian fits (a) and the two-component Gaussian fits (b) along the major-axis observation of the galaxy. The errorbars in the left plot are quite small.*

Velocity dispersion refers to the measurement of the spread in velocities with a higher velocity dispersion corresponds to a broader emission line profile. Velocity dispersion measurements are vital in studies of the ISM, star formation, turbulence and dynamics of galaxies (e.g. Mogotsi et al., 2016). A characteristic trait of diffuse gas is that it has a higher velocity dispersion compared to HII regions (e.g. Heald et al., 2007, Boettcher et al., 2016).
Panel (a) in Figure (24) shows that the distribution in velocity dispersion values along the major-axis has a trend consisting of periodic crests. The median dispersion value here is $\sigma = 26.16 \pm 3.38$ km s^{-1}, which is consistent with HII region line widths which are typically a few tens of km s^{-1} (e.g. Boettcher et al., 2017). The periodic increases in the dispersion values could be attributed to a non-uniform distribution in ionised gas. In some regions, we have denser pockets of ionised gas coupled with perhaps a greater presence of diffuse gas, resulting in broader profiles in some regions as opposed to others. The maximum dispersion value recorded here is $\sigma = 43.47$ km s^{-1} which is seen on the LHS of panel (a) in Figure (24) at about -70". This coincides with a region in which a high intensity of Hα is detected in the flux distribution taken along the major-axis of the galaxy.

The median dispersion of the narrow and broad components in panel (b) are $\sigma = 19.18 \pm 3.82$ km s^{-1} and $\sigma = 32.63 \pm 12.25$ km s^{-1} respectively. The median value for the narrow components is qualitatively consistent with HII regions with all the values residing in a range of 8 km s^{-1} $< \sigma <$ 30 km s^{-1}. The broad component values have a more significant spread, with values in the range of 18 km s^{-1} $< \sigma <$ 98 km s^{-1}. We also see that toward the center of the galaxy, the values between the broad and narrow components are similar, however, there is a greater difference in the values at more than 50" from the center on either side of the galaxy. There are a few consistently larger dispersion values in the broad profiles at -60", again in the region where the maximum Hα intensity in the galaxy is located. The LHS of panel (b) shows larger dispersion values in the broad components compared to the RHS, further reinforcing the idea of asymmetry in the gas distribution in the galaxy. The modest and larger velocity dispersions of the narrow and broad components are suggestive of thin (planar) and thick (planar and/or extraplanar) gaseous disks.

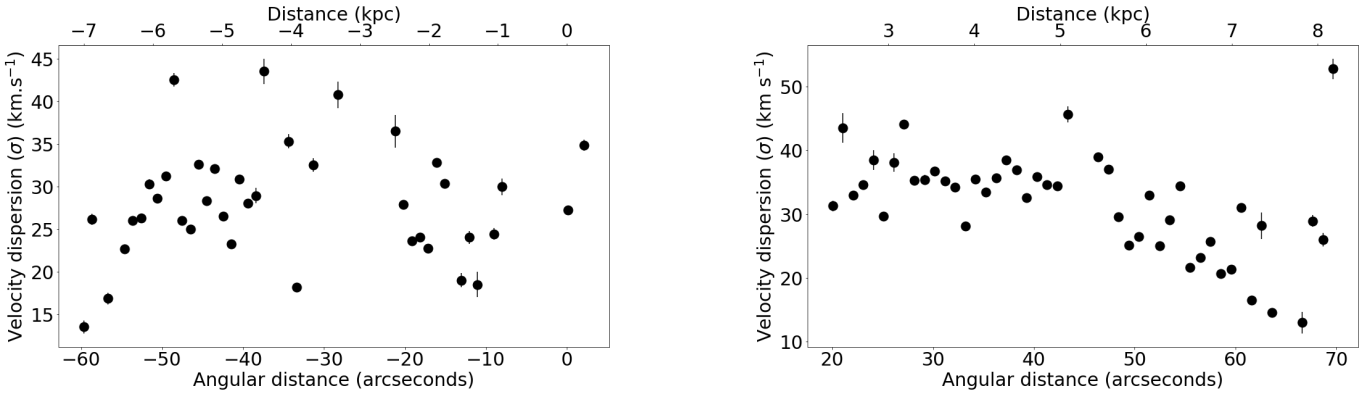

Figure 25: *The velocity dispersions of Hα for the single Gaussian fits for slits S3 (a) and S4 (b) which are the slits parallel to the major-axis above and below the galaxy respectively. The Angular distance on the x-axis provides the distance from the center of the galaxy (negative values are in the direction of the receding side of the galaxy and positive values are in the direction of the approaching side). The associated uncertainties are small.*

The velocity dispersions below and above the disk are largely similar as shown in Figure (25). The median dispersion values for S3 and S4 are $\sigma = 27.87 \pm 6.55$ km s^{-1} and $\sigma = 32.86 \pm 7.85$ km s^{-1} respectively. These values are fairly close to one another, with no significant difference between the values. The values from S3 and S4 are comparable to the dispersion values of the single component fits along the major-axis of the galaxy and lie in a range of 8 km s^{-1} $< \sigma <$ 46 km s^{-1} . This shows the dispersions in the ionised gas are quite similar both below and above the disk of the galaxy. Furthermore, the distribution in dispersion values are not entirely uniform and show some variation with distance along the major-axis of the disk. This is clearly shown by a spike in the values in Figure (25 (a)) and similarly smaller dispersion values than the rest in panel (b). The median dispersion values of S3 and S4 are similar to the median dispersion value along the major-axis, but we also see that there are consistently higher values in these figures as opposed to the major-axis. This could possibly be an indicator of eDIG emission.

Figure (26) shows the trend in velocity dispersion for each of the long-slit observations along the minor-axis. Most noticeably, these dispersion values overlap frequently with no distinct deviations in the range of values. The median values for the blue, red and black data points are $\sigma = 28.69 \pm 5.46$ km s^{-1}, $\sigma = 28.55 \pm 5.21$ km s^{-1} and $\sigma = 27.52 \pm 5.41$ km s^{-1} respectively. These values are all remarkably close, lying within 1 km s^{-1} of each other. Near the center of the disk we see these data points being nearly inseparable upon visual inspection, this is further justified by looking at the regions of Figure (24 (a)) corresponding to -60", 0" and 60" along the major-axis. These regions in (24 (a)) correspond to where slits S6, S2 and S5 intersect the disk respectively. The values show strong correlation between the two figures.
As we extend out from the disk, a trend in the dispersion values is noticeable where the values generally increase with distance from the disk. Broader profiles at a greater distance from the disk suggest the presence of eDIG.

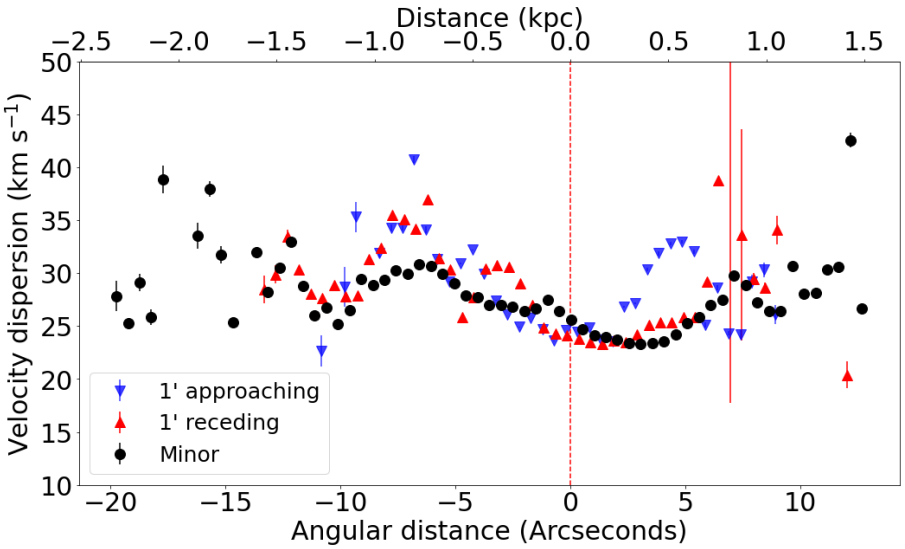

Figure 26: *The velocity dispersions calculated from the single Gaussian fits for slits S2, S5 and S6 which are the slits orientated along the minor-axis, at 1' parallel to the minor axis in the direction of the approaching side of the galaxy and 1' parallel to the minor-axis in the direction of the receding side of the galaxy.*

The median dispersion value for the broad component across the minor-axis in Figure (27) is more comparable to the single-component median velocity dispersion in Figure (26) with values of $\sigma = 30.25 \pm 4.73$ km s^{-1} and $\sigma = 27.52 \pm 5.41$ km s^{-1} respectively. The median dispersion for the narrow-component fits is $\sigma = 19.73 \pm 3.99$ km s^{-1} which is more typical of of the dispersion in HII regions. There are hardly any large deviations in the distribution of the broad or narrow component dispersions as they both appear to fluctuate near the median value with no major outliers. The median velocity dispersions of the narrow components in Figures (28) and (29) are $\sigma = 19.36 \pm 3.32$ km s^{-1} and $\sigma = 20.46 \pm 2.99$ km s^{-1} for slits S5 and S6 respectively. These values are remarkably close and are consistent with the velocity dispersion of HII regions similar to the narrow component velocity dispersions of the slits previously discussed. There is a more noticeable difference in the median broad component dispersions with median values of $\sigma = 33.62 \pm 5.96$ km s^{-1} and $\sigma = 34.43 \pm 8.49$ km s^{-1} for S5 and S6 respectively. These dispersion values are similar and is also present along the major-axis in Figure (24 (b)) where we see similar velocity dispersions at -60" and 60" which correspond to the same regions of the galaxy being probed by slits S6 and S5 respectively.

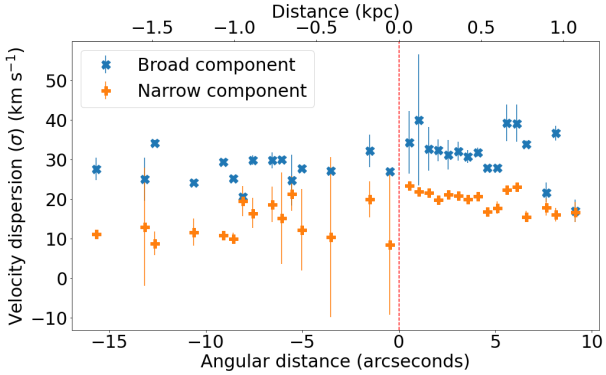

Figure 27: *The two-component velocity dispersions of Hα along the minor-axis of the galaxy*

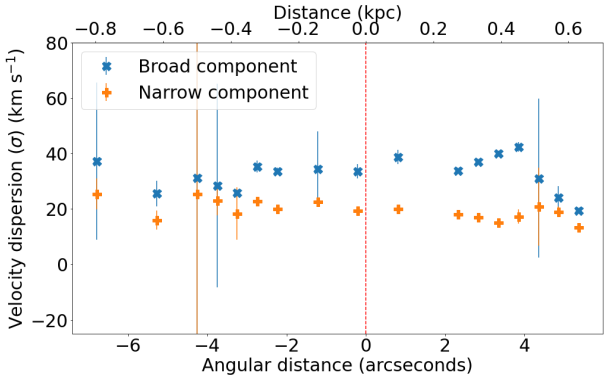

Figure 28: *The two-component velocity dispersions as a function of distance from the galactic disk along slit S5 of the galaxy.*

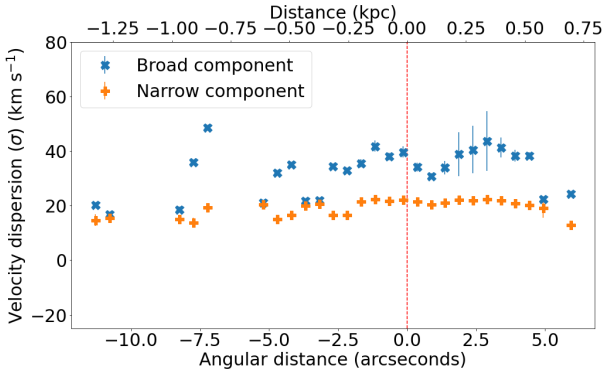

Figure 29: *The two-component velocity dispersions as a function of distance from the galactic disk along slit S6 of the galaxy.*

4.2 Radio Data

4.2.1 Tilted ring models

In our tilted-ring models, we model the galaxy as consisting of only one disk. The procedure followed here is outlined in section 3.4.1. Since we model the galaxy as only one disk, one of the first steps was to determine the scale height of the disk. We take advantage of the galaxy being edge-on and we measured the flux distribution as a function of distance from the mid-plane of the galaxy using the moment 0 map of UGCA 250. This was fitted with a decaying exponential described by equation (9). Here, we find a disk with a scale height of 12.28" which translates to a physical scale 1.44 kpc. To perform efficient tilted-ring modelling and obtain a good fit, the cube needs to be masked in order to identify the regions ascribable to the galaxy in the cube. A mask was built using 3DBarolo's *SEARCH* task which uses a source finder derived from Duchamp (Whiting, 2012) and builds a mask directly on the identified regions of emission. The source finder in our case only considered sources above 3 $\times$ *rms* in the cube. All the following models were fit on cubes that have been masked.

The first approach was to model the entire kinematics of the disk with a base model where the free parameters were the rotational velocity (V_{rot}), the velocity dispersion (V_{disp}), the position angle (PA) and inclination (INC). As initial guesses for these parameters we supply 120 km s^{-1} for the rotation velocity as this is approximately the rotation velocity that the rotation curve flattens at. The center coordinates, the width of each ring, the number of rings and the systemic velocity were kept constant and were calculated as described in section 3.4.1. The velocity dispersion was given an initial guess of 10 km s^{-1} which is a reasonable approximation for the dispersion of HI gas. The initial PA value was taken by using the observational optical data. However, the PA here differs since in the optical data it is measured as the angle made between the alignment of the slit and North whereas in 3DBarolo it is taken as the angle that the receding side of the galaxy makes with respect to North. This value was taken to be 254°. The inclination supplied was that of the optical disk, 74.9°. Although HI disks are expected to flare in their outermost regions (e.g. Kalberla and Dedes, 2008), we take the scale height to be 12" as determined by our fit and assume it to be constant,

Unphysical discontinuities can often arise in the derived rotation curve when applying tilted-ring modelling. This comes as a consequence of fitting geometrical and kinematic parameters simultaneously (Di Teodoro and Fraternali, 2015). Specifically, the fits of the inclination and position angle can show non-uniformity and numerical scatter not indicative of the true geometry of the data. A common approach to this issue is a two-stage fitting procedure which consists of firstly deriving a model by fitting all the parameters simultaneously, followed by a second which fixes the geometrical parameters to a functional form. In this analysis, we interpolate the inclination and position angle by a polynomial of degree 3 in the second stage of the fitting process. This was done for all the tilted-ring models addressed in this work.

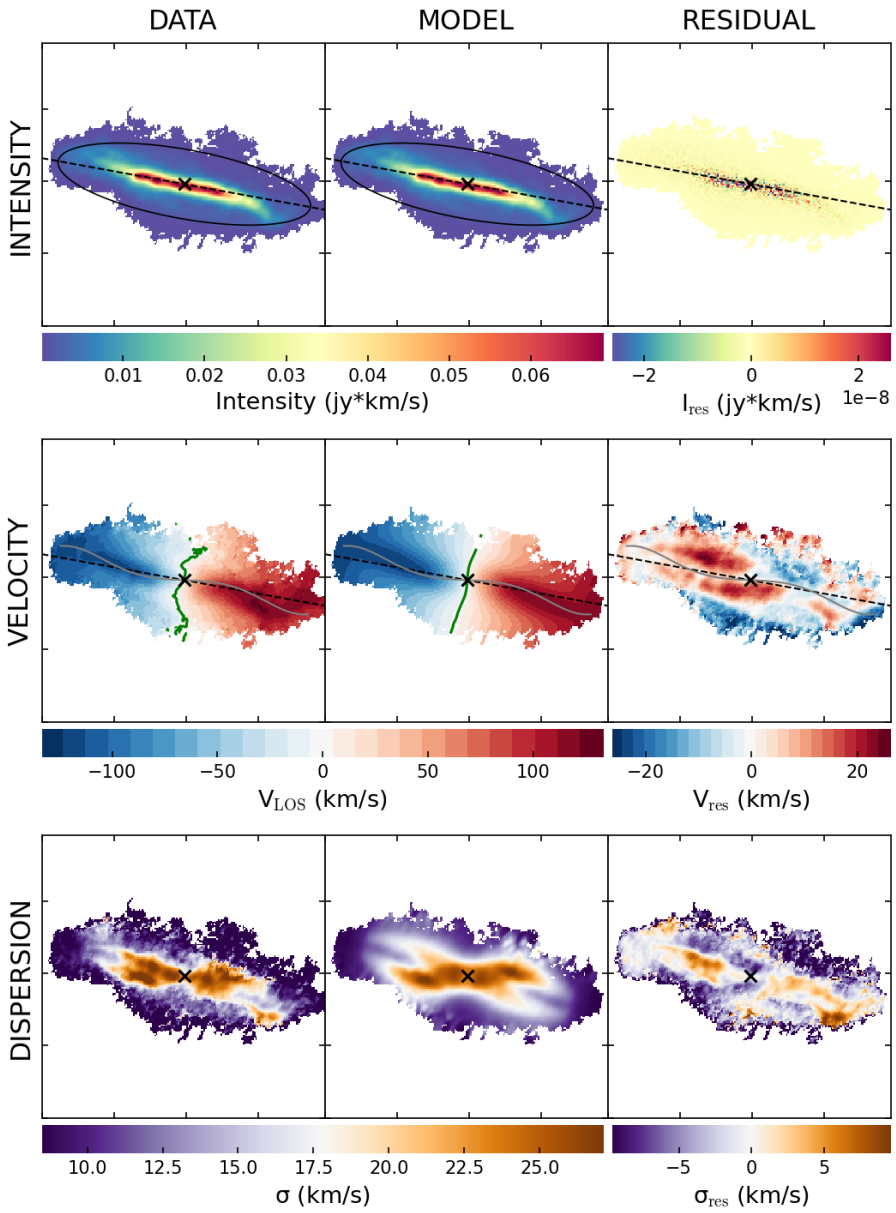

Figure 30: *The moment maps for UGCA 250 are shown in the first column of the left with the moment 0, 1 and 2 maps in the top, middle and bottom row respectively. The second column displays the associated moment map of the tilted-ring model. The third column shows the residuals of the model (Data - Model). The ellipse indicates the outermost tilted-ring and the 'x' shows the location of the center of the galaxy.*

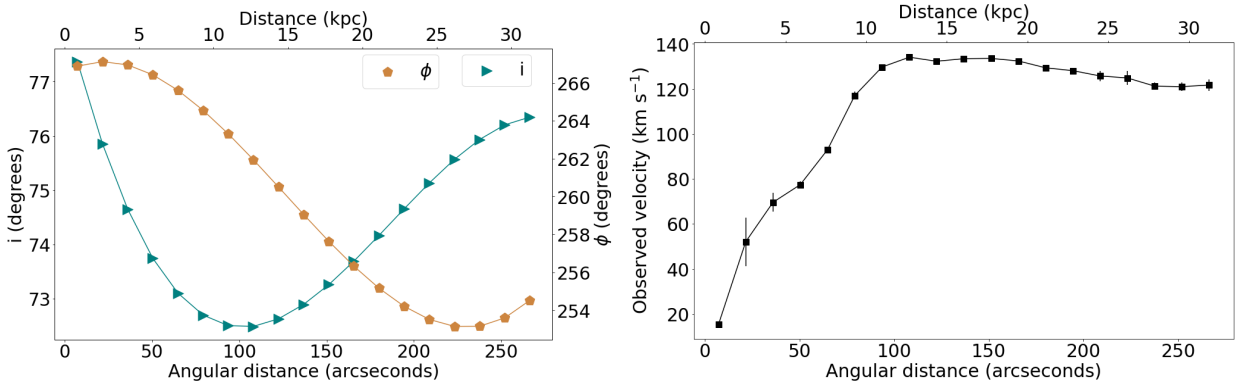

(a) (b)

Figure 31: *The inclination and position angles of the rings as a function of distance from the center of the galaxy (a) and the rotation curve along the major-axis (b) for the symmetric tilted-ring models. The inclination and position angle was regularised by a polynomial, therefore the data points have no errorbars.*

The residuals of the moment 1 map in Figure (30) provide an indication that the model is providing a fair estimate of the kinematics of the disk as there are minimal residuals along the major-axis. However, just off the disk we see that the model is slightly overestimating the velocities by more than 10 km s^{-1}. This is true for both the approaching and receding side of the galaxy, but this is more prominent on the approaching side. The receding side does have a region just above the disk off the major axis where the velocities are slightly underestimated and this same result is not seen on the opposite side of the galaxy, suggesting that the HI kinematics are not symmetric. The changing in position angle of the galaxy shown in Figure (31 (a)) shows that the HI disk is warped similar to the Hα disk as shown in Figure (4). Similarly, the inclination angle changes as we extend with radius. The inclination decreases from the center up until about 100" and then increases as we reach the extent of the galaxy. Due to this asymmetry in the disk, the approaching and receding halves were modelled independently using the same aforementioned initial guesses for the estimation of the kinematic and geometrical parameters.

Figure (32) shows the kinematic maps for our tilted-ring model where the approaching side was modelled. Upon visual inspection of the moment 1 map, it is clear that the residuals in the velocities on the approaching half are minimised more so compared to the model in Figure (30). This is evident just above the disk in the approaching side, where the model in Figure (30) underestimated the velocities compared to Figure (32). Furthermore, comparing the residual map of the velocities between these two models we see hardly any difference in the residuals on the receding half of the galaxy, showing that modelling both halves simultaneously is not the most efficient way to model this galaxy. Similarly, when modelling the receding half of the galaxy in Figure (33), we see less residuals on the receding side compared to the model in Figure (30). It also appears that the model in Figure (33) model the velocity dispersion throughout the galaxy the best compared to the other two models. The areas with the highest residual counts in the velocity maps are located around the major-axis of the galaxy. The inability of the models to correctly account for the rotation in these areas as opposed to those regions in the disk is suggestive of slower rotating gaseous layers in the outskirts.

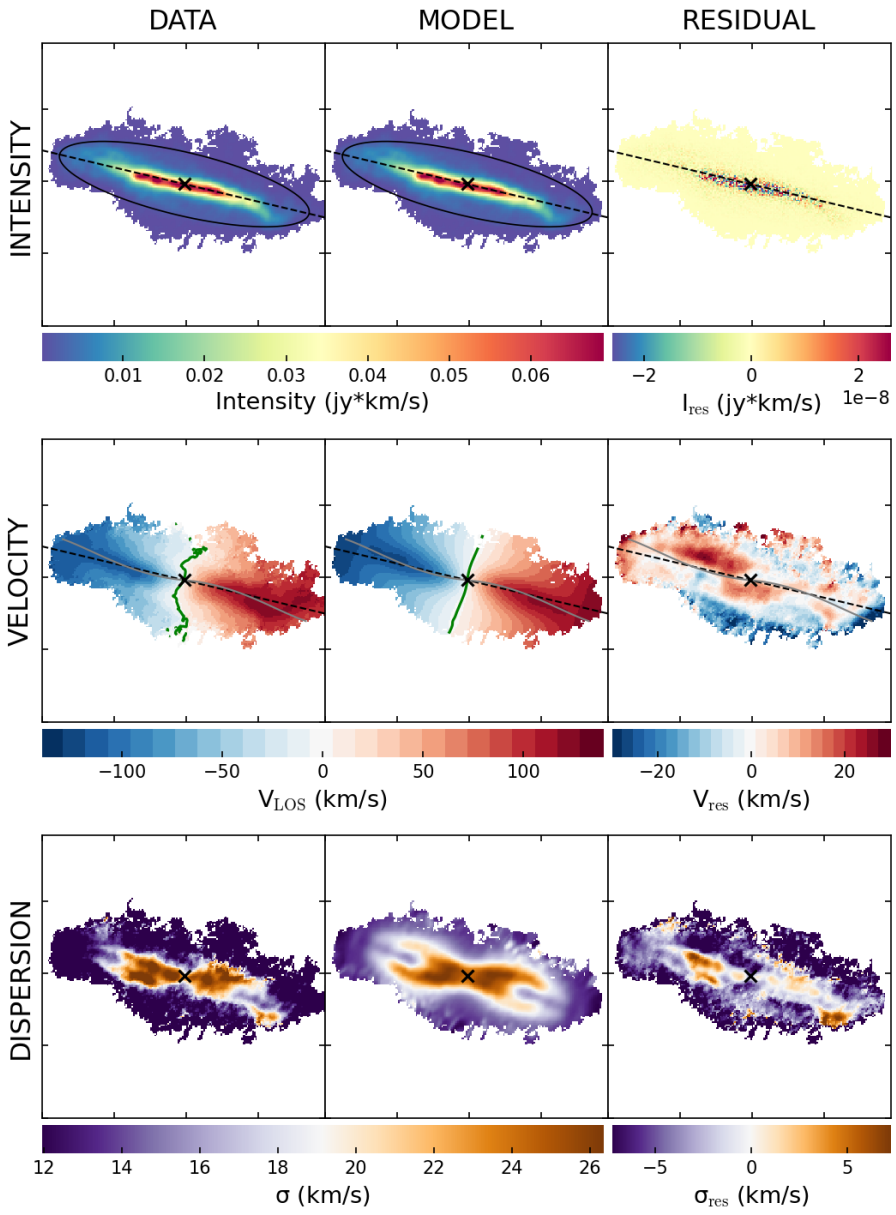

Figure 32: *The moment maps and residual maps for the tilted-ring model for the approaching side of the galaxy*

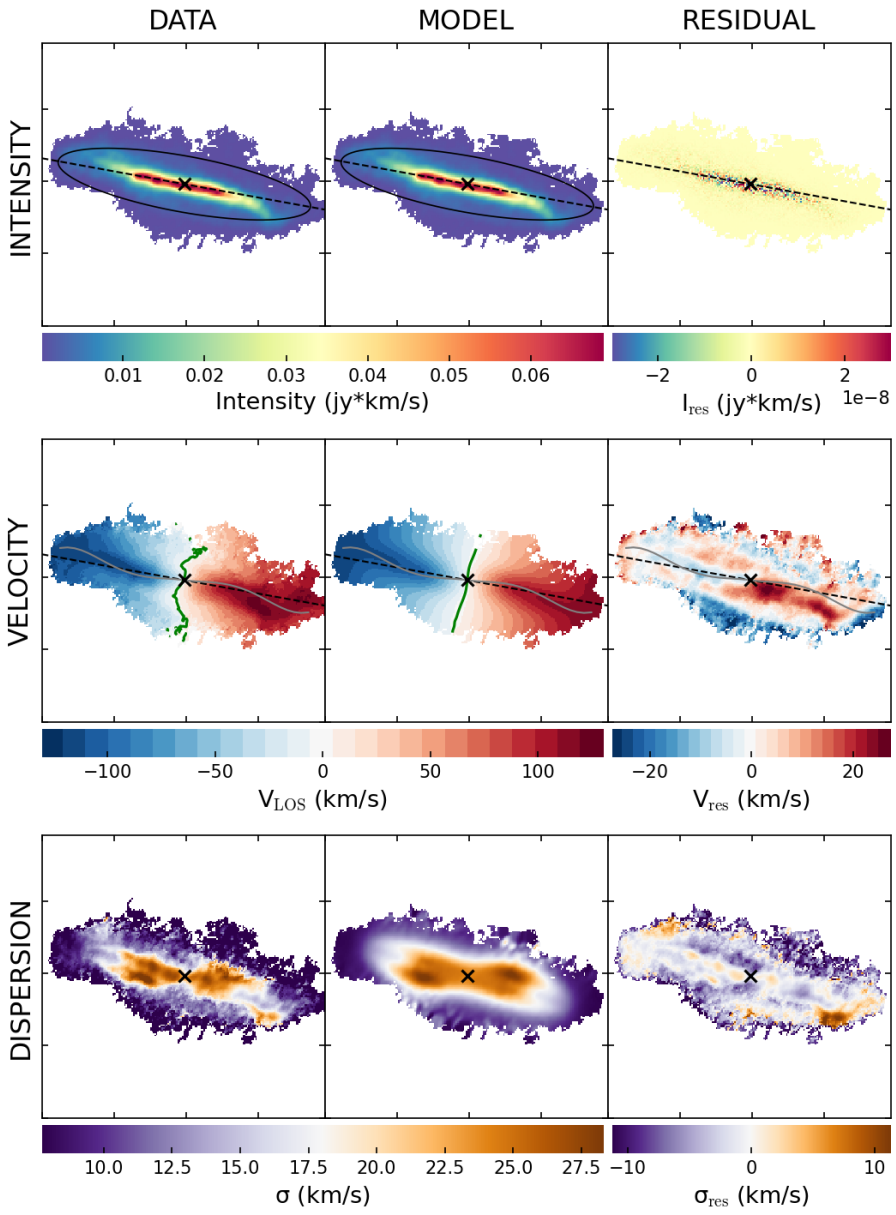

Figure 33: *The moment maps and residual maps for the tilted-ring model for the receding side of the galaxy*

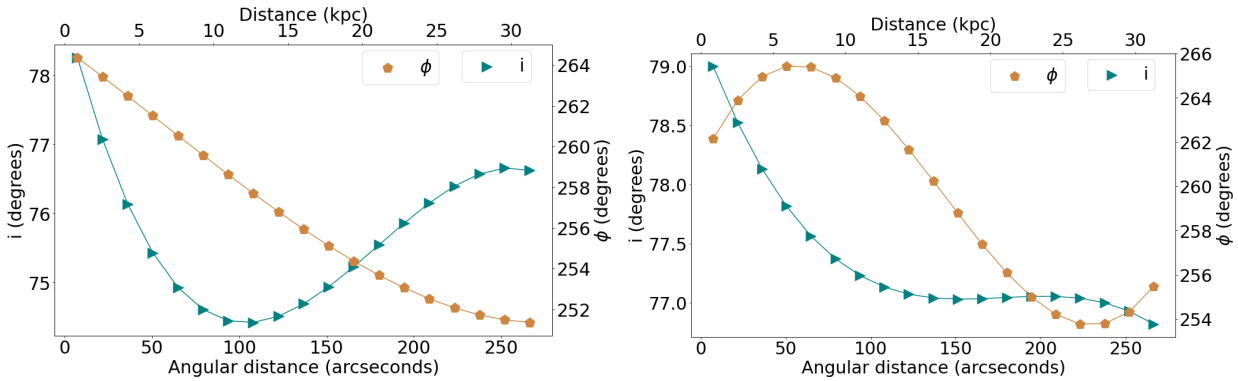

Figure 34: *The inclination and position angles of the rings as a function of distance from the center of the galaxy for the models of the approaching side (a) and the receding side (b) of the galaxy.*

The asymmetry in the geometry between the approaching and receding halves is noticeable when comparing the inclination and position angles as a function of radius of the respective models. More noticeably is that both halves have a physical warp as indicated by the change in position angle with radius. The warp on the approaching side is described by a gradually declining position angle where the disk is consistently changing its orientation with radius. The warp on the receding side is described by the position angle first increasing until about 50" and then decreasing until about 225" , after which it increases toward the extent of the galactic emission.

The PV-slices along the major and minor axes show how closely the models match the data. In the model for both sides of the galaxy in Figure (35 (a)), we see that this model is unable to produce the features of beard gas in the PV-slice along the major-axis. The PV-slice along the minor-axis suggests that the model recovers the emission from the data much more efficiently than that of the major-axis. This further justifies that the two halves of this galaxy can not be simultaneously modelled as this model reproduces the data poorly. Both the models of the approaching side and the receding side of the galaxy perform better in the aforementioned regions of lagging gas. The features of the lagging gas are better reproduced by the model of the receding half of the galaxy compared to the approaching half, but the receding half does model extra emission not present in the data. This is the emission within 100" of either side of the center of the galaxy where the red contours are tracing no emission in Figure (35 (c)). The region in question is better accounted for in the model for the approaching side of the galaxy. Both of the minor-axis PV-slices in Figures (35 (b)) and Figure (35 (c)) show that these models perform better than Figure (35 (a)) by not modelling emission not present in the data on the LHS of the diagram. These models cover the extent of the gas in the data more accurately, however, they do still model extra emission in the upper left quadrant of this diagram where the red contours extend a bit further out than the blue contours in both models.

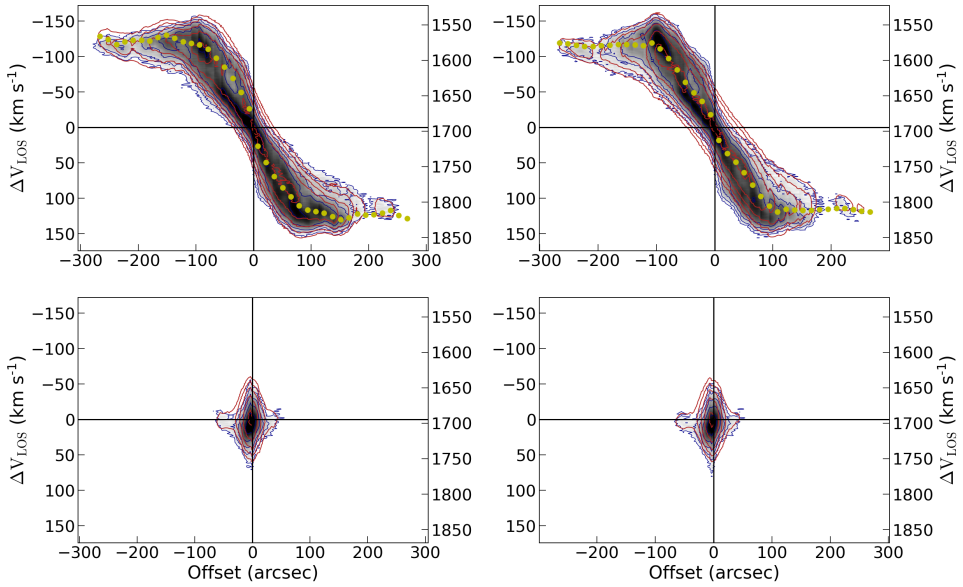

(a) (b)

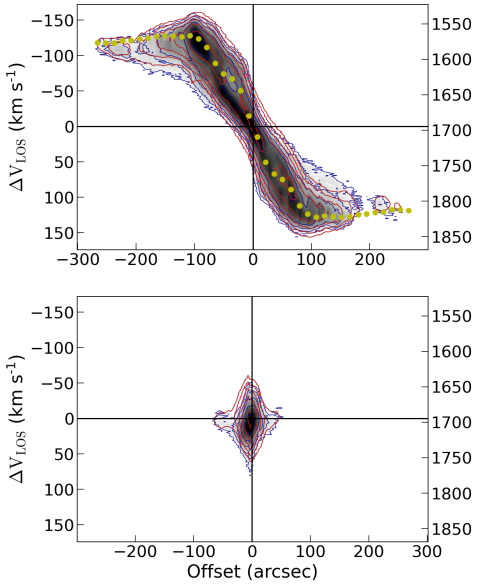

(c)

Figure 35: *The PV-diagrams along the major-axis (top row) and minor-axis (bottom row) of the models which modelled the approaching side (a), the receding side (b) and both sides (c). The contours are shown in units of* $2^n \times$ *RMS where n=1,2,..,7.* . Data and model are shown in blue and red contours respectively.

The rotation curves of each of the models show the slight kinematic asymmetry between the approaching and receding halves of the galaxy. The approaching side rises more sharply in the inner regions and all three of the rotation curves flatten out at about 100" where a rotation velocity of around 120 km s^{-1} is attained. In the flat region of the curve, the approaching side consistently maintains a higher rotation velocity than the receding side indicating that this side of the galaxy is rotating faster than the other. The rotation curve from the model of both sides simultaneously appears to be compensating for the differences in both sides since the inner region of the curve has velocities similar to either side, not blatantly favouring one side over the other. An explanation for the discrepancy in the inner regions of the curve could be the more efficient estimation of the beard gas in the model of the receding side of the galaxy seen in Figure (35 (b)). The fact that the model for the receding side of the galaxy models the beard emission better than the model for the approaching side could be attributed to the difference in the distribution in the velocity dispersion. Figure (36) shows that within a radius of 150", the velocity dispersions on the receding side are consistently higher than those in the approaching side, resulting in the model for the receding side having emission more representative of the beard gas.

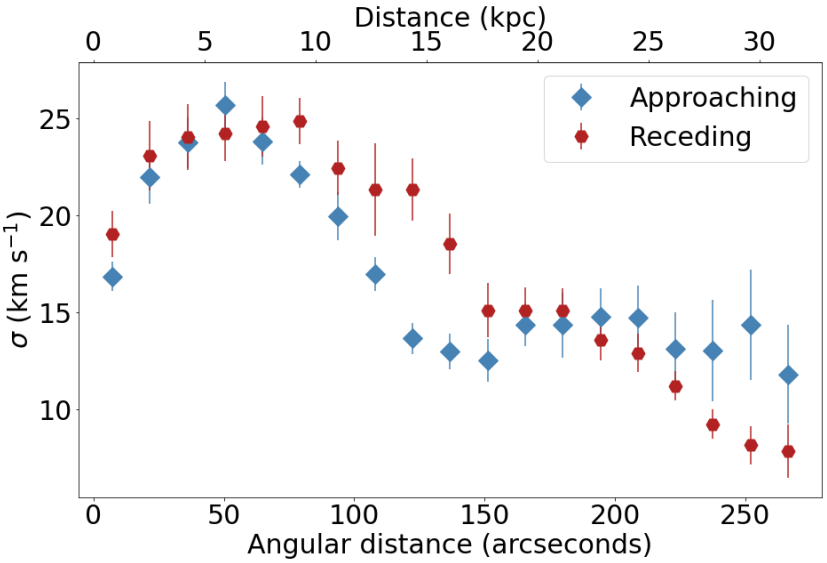

Figure 36: *The distribution of the velocity dispersions along the major-axis for the models of the approaching and receding side.*

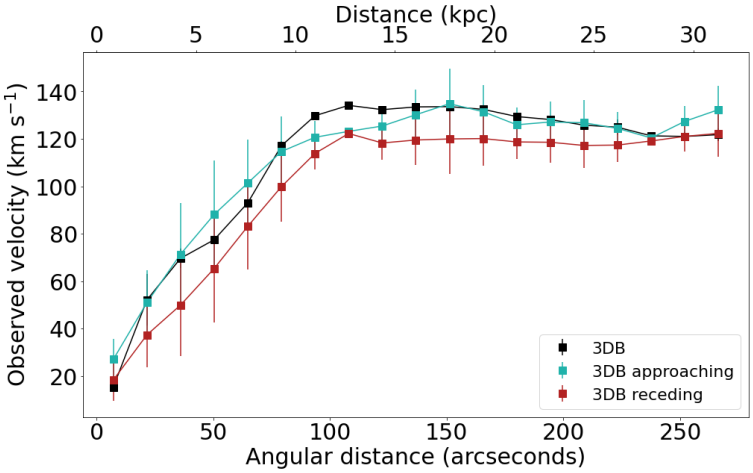

Figure 37: *The rotation curves along the major-axis for each of the tilted ring models where both sides of the galaxy are modelled symmetrically, only the approaching side is modelled and where only the receding side is modelled. The errorbars are from 3DBarolo for the symmetric curve while the errorbars on the approaching and receding sides are taken as the difference in their velocities.*

The rotation curves for each of the models in Figure (37) show that the same rotational behaviour is present in each of the models. Here, the model for the approaching side has a rotation curve with consistently higher rotation velocities than that in the model of the receding side. This is true for both the rising and flat part of the rotation curves. The maximum rotation velocity of the approaching side is 134.8 km s^{-1} which exceeds the maximum rotation velocity of the receding side of 122.3 km s^{-1}.

4.2.2 Position-velocity diagrams

We take the position-velocity diagrams along the same positions as our long-slit observations of the galaxy. The HI, however, extends much further from the disk than the Hα emission. Thus, the PV-diagrams were extracted by using lengths of 12' in contrast to the 8' long-slit lengths along the major-axis of the galaxy. For the minor-axis, the PV-diagrams were extracted with a length of 8' due to a lesser extent of emission compared to the major-axis.

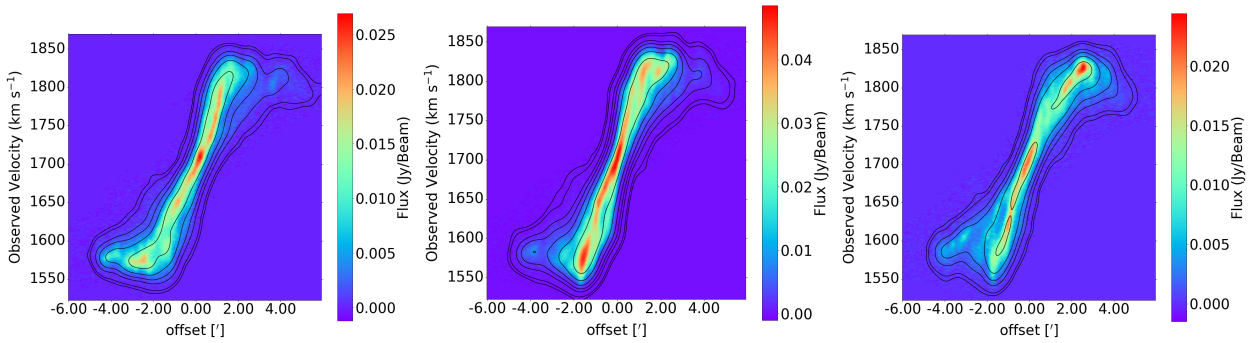

Figure 38: *PV-diagrams extending 12' centered at the same positions as S3 (a), S1 (b) and S4 (c).The contours are shown in units of 2^n × RMS where n=1,2,..,9.*

The PV-diagrams in Figures 38 (a) and (c) show that there is a clear asymmetry in the gas distribution above and below the disk. This is shown not only by the kinematics, but also the flux distribution along which these slices were taken. This serves as evidence that the aforementioned warp in the ionised gas in the disk is also present in the HI disk. The greatest intensity of flux in Figure (38 (c)) is present at 2' from the center of the disk toward the receding side of the galaxy.

The PV-diagram along the major-axis in Figure (38) shows evidence for 'beard' gas in this galaxy with extended emission toward the systemic velocity of the galaxy. This indicates the presence of lagging gas with respect to the disk gas. Furthermore, a fraction of this gas could be extraplanar, residing in front of the galaxy with respect to the observer. This 'beard' gas also presents itself above and below the disk and shows its presence in Figures 38 (a) and (c). However, it must be stressed that due to the inclination of this galaxy, much of what could be indicative as beard gas in the PV-diagrams could instead be foreground disk gas. This phenomenon is shown in Figure (11) where a LOS samples contributions from many galactrocentric radii. Thus, some of this gas which appears to be lagging is indeed gas residing in the thin disk at closer radii.

The PV-diagrams in Figure (39) are taken along and parallel to the minor-axis of the galaxy at offsets of 1 and 2 arcminutes in both the receding and approaching side of the galaxy. By assessing the PV-slices taken parallel to the minor-axis, we can look for further indicators of lagging gas. This is given by the diagrams exhibiting a triangular shape (Kamphuis et al., 2013). This is evident in all of the parallel slices, providing stronger evidence for lagging diffuse gas.

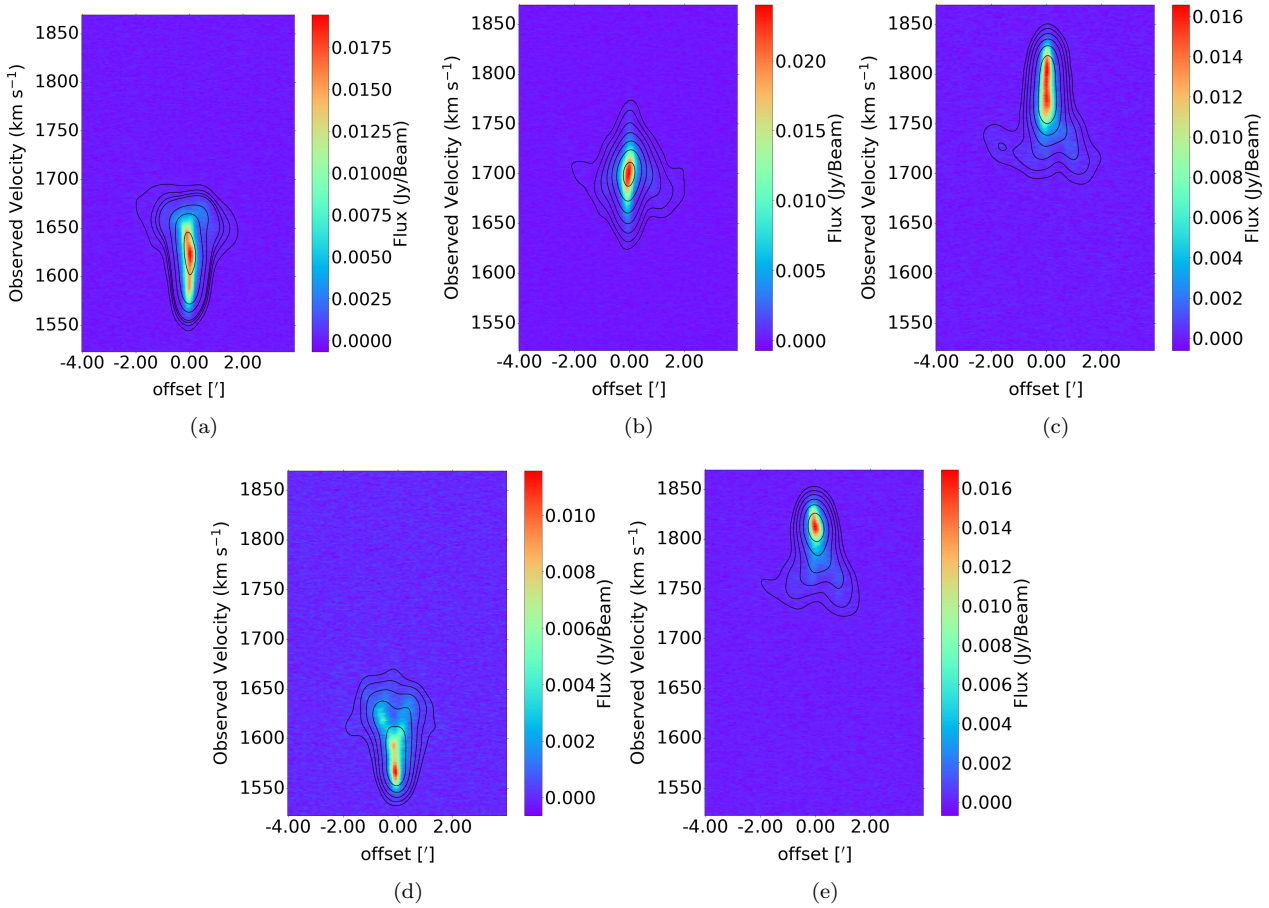

Figure 39: *Position-velocity diagrams taken along the minor-xis. Panel (b) shows the PV-diagram along the minor-axis of the galaxy. Panels (a) and (c) are the PV-diagrams taken along 1' offset parallel to the minor-axis toward the approaching side and receding side respectively. Panels (d) and (e) show the PV-diagram along the minor-axis at a 2' offset parallel to minor-axis once again toward the approaching and receding side of the galaxy. The contours are shown in units of 2^n × RMS where n=1,2..,7*

4.2.3 Rotation curves

The rotation curves derived in this section have been obtained by implementing the envelope-tracing method.

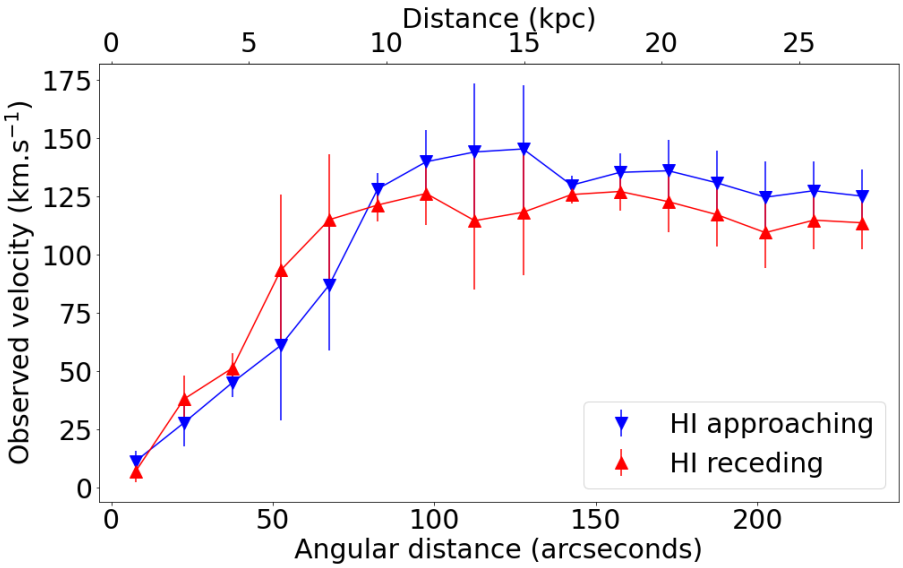

Figure 40: *The rotation curves for the approaching and receding side of the galaxy. The errors are represented as the difference between the respective velocities in the approaching and receding side.*

The rotation curves in Figure (40) appear quite similar with a steep inner part which eventually settles after about 100" from the center. The main difference between the curves is evident in the rising part where the receding side has a slightly steeper gradient, indicating that these inner parts of the receding side are rotating slightly faster than the analogous parts on the approaching side. This changes, however, where about between 80" and 120" the velocities on the approaching side are consistently higher with the largest difference in velocity being 32.34 km s^{-1} indicated by the large errorbar. The kinematics of either side are in good agreement with one another after 100" where the curves flatten out at a rotation velocity of about 120 km s^{-1}.
We look at the correlation between the rotation curves derived from the envelope-tracing method and the rotation curves from our tilted-ring models. This is shown in Figure (41) which displays the rotation curves from Figure (40) along with the rotation curves from the tilted-ring models for the symmetric disk as well as where the approaching and receding halves were modelled independently. By eye, all the rotation curves have the same trend with a gradient that increases and eventually settles after 100" at a rotation velocity of around 120 km s^{-1}. One contrast between the rotation curves derived with these different methods is that with the envelope-tracing method, we see that the receding side's curve rises more steeply than the approaching side, while the converse is true for the rotation curves derived with the tilted-ring models. Noticeably, the rotation curves of the approaching side deviate significantly in the inner regions of the galaxy, where the curve from the tilted-ring model has a much steeper gradient in this region. The kinematics on the outskirts are all in good agreement with one another, where each curve is describing a rotation velocity of about 120 km s^{-1}. The median velocities for each of the rotation curves in the region beyond 100" are listed in Table (5). Both the rotation curves of the tilted-ring model and the envelope-tracing method of the approaching side have velocities consistently higher than the receding side in the outer regions of the galaxy, indicating that the HI rotates slightly faster on the approaching side.

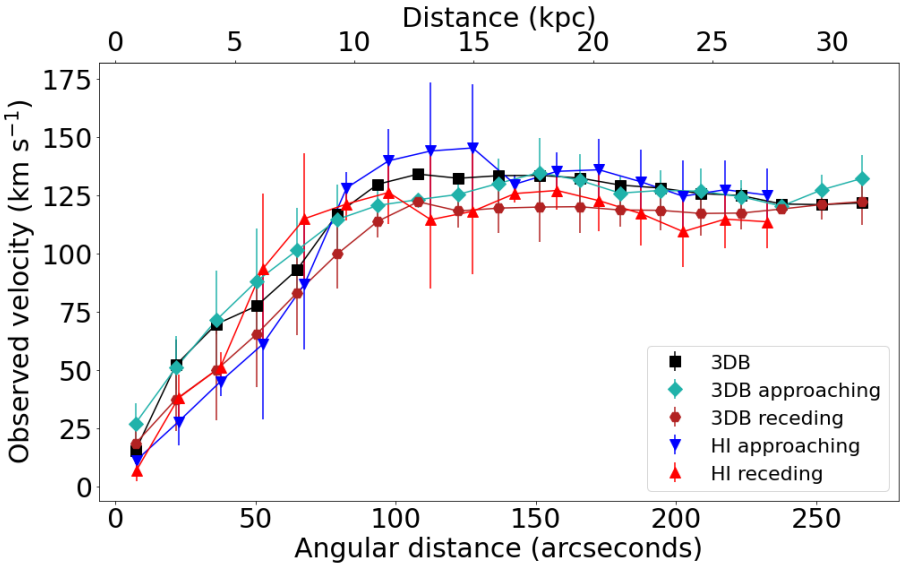

Figure 41: *The rotation curves derived with the envelope-tracing method as well as the rotation curves derived from the 3DBarolo models. These curves include those from the Base model and the independent models of the approaching and receding side.*

Rotation curve	Median velocity (km s^{-1})	Uncertainty (km s^{-1})
3DB	128.75	4.88
3DB approaching	126.93	3.93
3DB receding	119.29	1.62
HI approaching	125.07	7.21
HI receding	117.11	5.59

Table 5: *The median velocities of the rotation curves in Figure (41) beyond 100" where the rotation curves flatten out. The uncertainties reported are the standard deviation of the velocities in the region where the rotation curve flattens out. Taking the standard deviation as the error between the velocities of each of the curve we obtain a value of 4.48 km s^{-1} indicating relatively minimal spread between the rotation velocities in these curves.*

4.2.4 Gaussian decomposition

Gaussian decomposition was performed on the galaxy where a maximum of two components were assumed, with the physical justification being that one relates to the thin disk and the other to the diffuse gas in the galaxy. These were characterised by the components being narrow or broad respectively. The distinction between these was simplistic as they were differentiated solely based on their width with the diffuse component being represented by the broader Gaussian and the thin disk component the narrower Gaussian component.

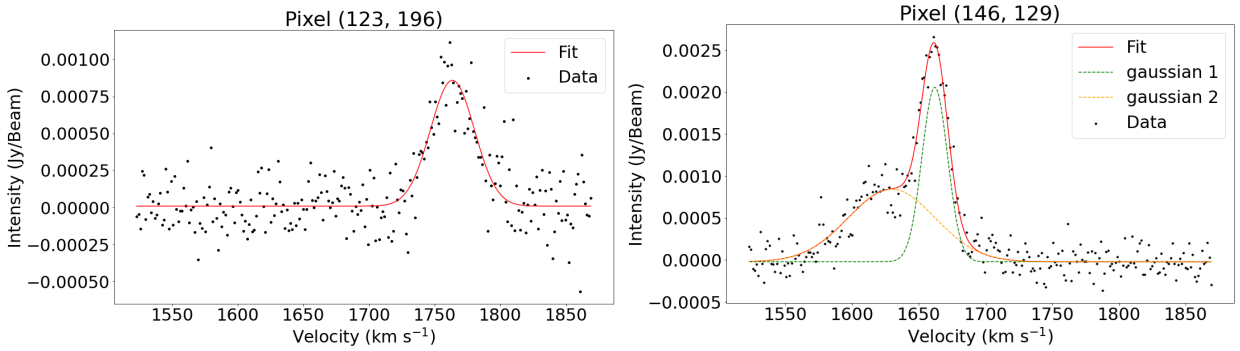

(a) (b)

Figure 42: *Velocity profiles extracted from the HI cube showing examples of the types of velocity profiles the 1-component fit (a) and 2-component fit (b) were performed upon.*

Figure (42) shows the stark contrast in the geometry of the profiles which could only be approximated by a single Gaussian fit as opposed to those that blatantly contain more than a single component. Furthermore, the two components in the profile of Figure (42 (b)) exhibit a velocity difference exceeding 50 km s^{-1}, showing the kinematic difference between the components.

After all these fits were performed, the parameters were extracted and synthetic radio cubes were made from the single fits, the broad component fits and the narrow component fits from the two-component fits. This resulted in HI cubes representing the diffuse gas, the disk gas and the HI in which only one component was detected in the profiles. In Figure (43) we visualise the pixels in the cube which contain either 1 or 2 fit components from our decomposition. The number of pixels with 2-component fits are concentrated toward the center of the galaxy within the disk with the single component fits occupying the outer regions of the galaxy. This is mostly expected, due to the high inclination we expect the profiles within the disk to be more complex as the gas is more concentrated in the inner parts of the disk. This results in a profile as shown in Figure (42 (b)) which contains more than a single component since our LOS samples gas from many galactrocentric radii. The same LOS should sample just as many radii in the outer regions where only a single component is present, however, this gas is a bit more diffuse and less gravitationally bound resulting in only a single component being present in the velocity profile.

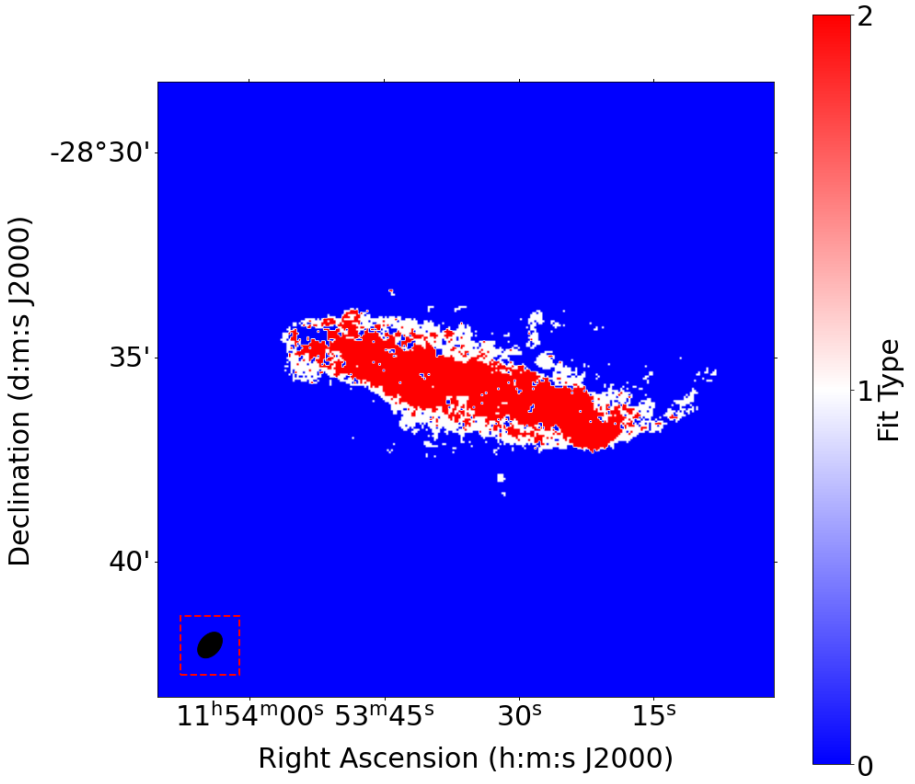

Figure 43: *Map displaying the number of fit components in each pixel. This shows where the Gaussian decomposition code fitted either 1 component or 2 components in the velocity profiles extracted from each pixel.*

The moment 1 maps of the broad and narrow components in Figure (44) show the velocity distribution of the respective cubes throughout the disk. The distribution of the velocity in the narrow component is more representative of a thin, rotating HI disk as the profiles are distributed along the major axis describing an increasing rotation curve which flattens out in the outer regions of the galaxy. The broad component velocities from the moment 1 map are not as uniformly distributed and appear more disjointed, indicative of a diffuse planar thick HI disk. This is further seen where the velocities of the broad components tend more toward the systemic velocities than those of the respective narrow components in the same regions, suggesting that there is lagging planar/extraplanar gas being represented by the broad components. Due to the high inclination of the galaxy the broad component velocities here can not be definitively attributed to either only planar or only extraplanar gas, however the kinematic lag inherent in these components is suggestive of a thicker, diffuse HI disk in addition to the thin, rotation-dominated HI disk described by the narrow components.

The moment 2 maps in Figure (44) both show larger velocity dispersion values in the central region of the galactic disk and smaller values along the outskirts of the disk with the median narrow and broad component dispersion values of 10.16 $\pm$ 3.63 km s^{-1} and 18.96 $\pm$ 5.74 km s^{-1}. This is true for the maps of both components, since the main consequence of this is that more gas is being sampled by a LOS that penetrates through central regions of the galaxy. This results in contributions to the velocity profile from gas at all radii, broadening the profile which means its components too are broadened by this effect.

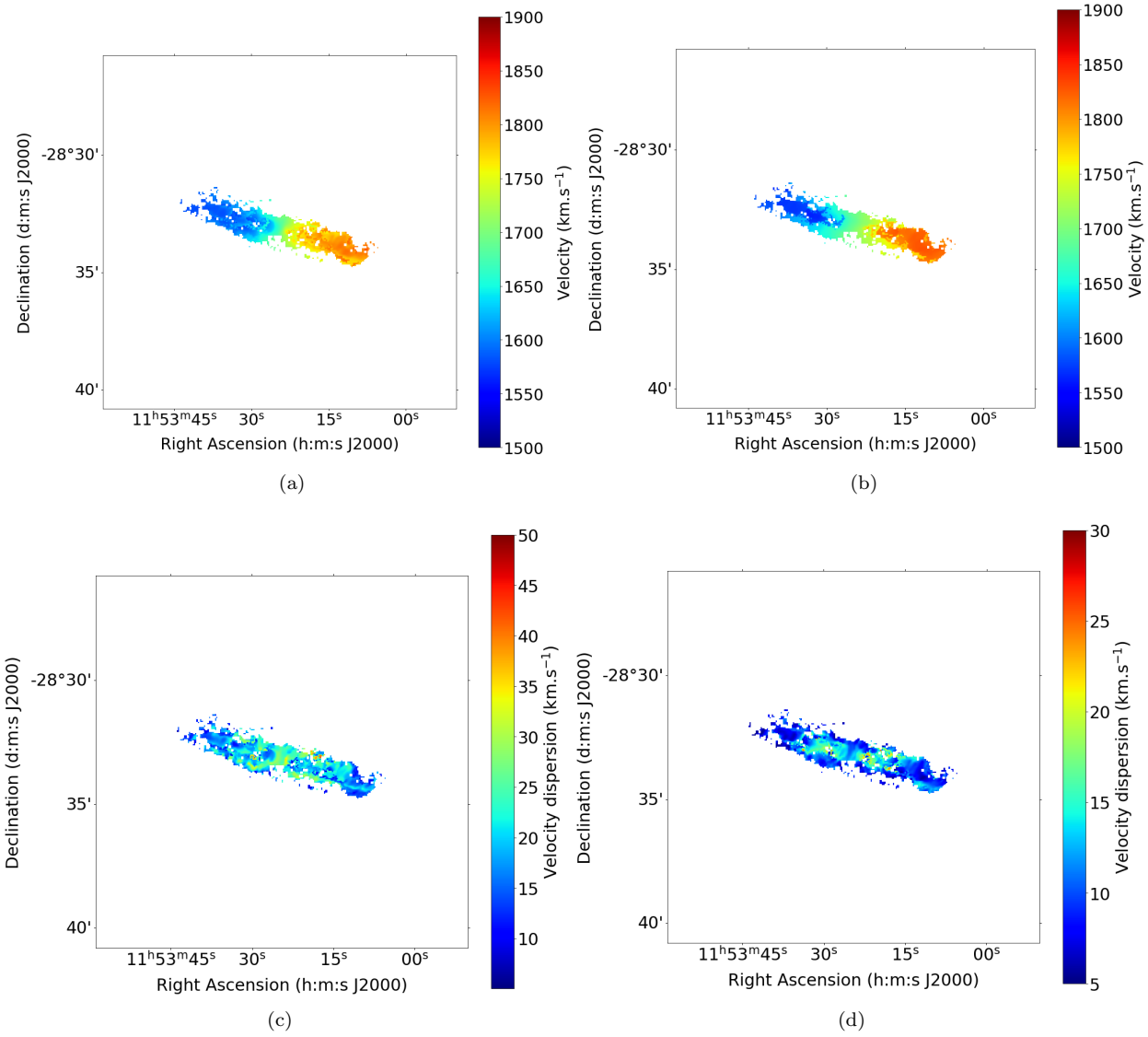

Figure 44: *Top row: Moment 1 maps of the broad component (a) and narrow component (b) cubes. Bottom row: Moment 2 maps of the broad component (c) and narrow component (d) cubes.*

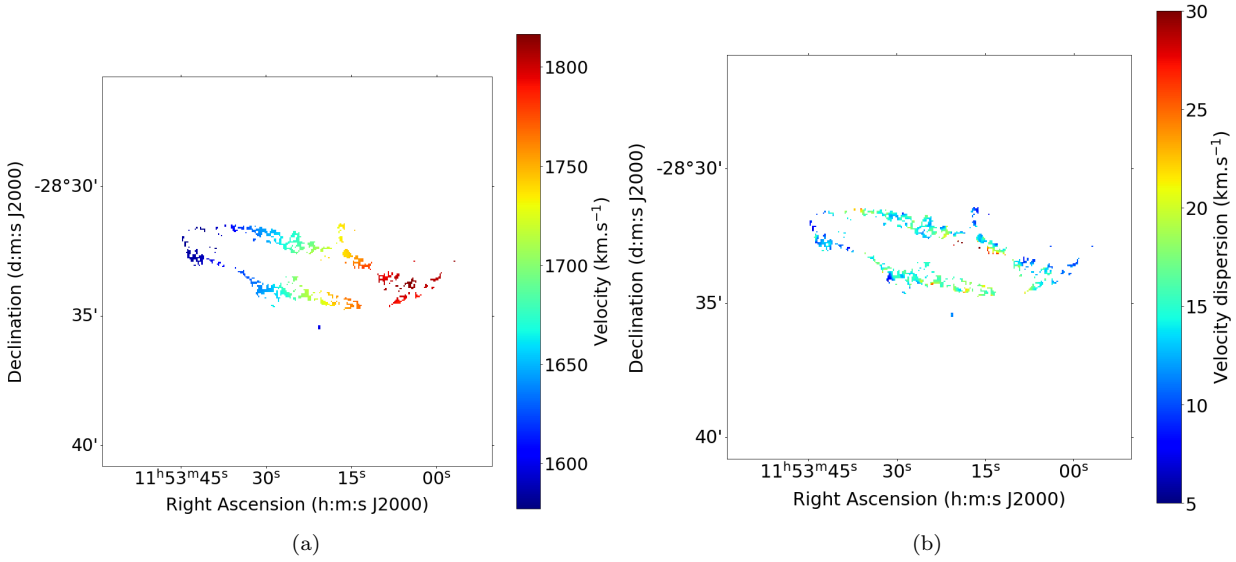

(a) (b)

Figure 45: *Moment 1 map (a) and moment 2 map (b) of the single component cubes*

The moment 1 map of the single component fits in Figure (45) show that these single component velocity profiles are following the rotation of the disk. These components do exhibit a kinematic lag with respect to the velocities of the component in the disk. This is seen when comparing the moment 1 map of the single component fits with that of the entire disk. The moment 2 map of the single component fits show no distinct trend, apart from some of the highest velocity dispersion values being concentrated toward the central region of the galactic disk. Figure (46) shows that the single component dispersions are distributed between the values for the narrow and broad component dispersions.

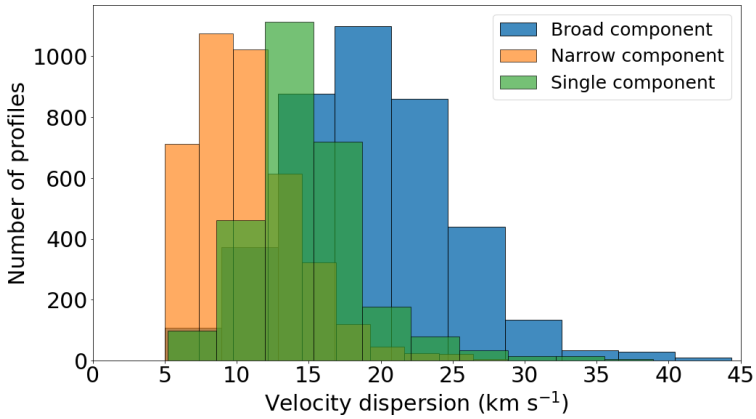

Figure 46: *Density plot of the velocity dispersions of the broad and narrow components showing the distribution of values for these components.*

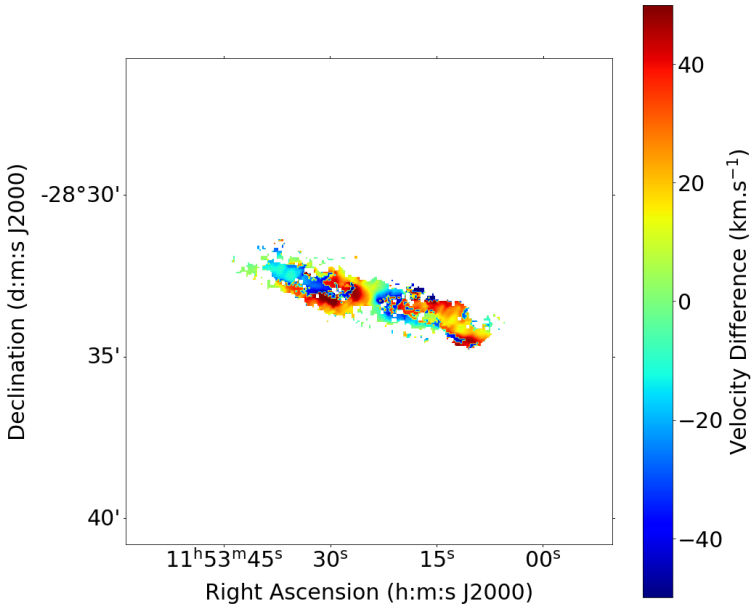

Figure 47: *The velocity difference map between the velocity maps of the narrow and broad components. The difference is taken as (narrow-broad).*

Figure (47) shows that the difference in the velocities between the broad components is not entirely indicative of lagging gas throughout the disk. There are, however, regions in which the narrow component has consistently higher velocities than the broad component. This is seen on the receding side where it shows that the narrow components are rotating faster than the broad components. Similarly, on the approaching side, the region of negative velocity difference indicates that the broad component velocities are nearer to the systemic velocities than the narrow components in this region. This does not, however, indicate the presence of a steadily lagging broad component on either side of the disk, consistent with a layer of slowly rotating EPG associated with the disk. In the inner regions, close to the systemic velocity, there is an area of great velocity difference. This is possibly the result of beam smearing which is most prevalent in the denser regions of a galaxy. Projection effects are also present throughout the disk of the galaxy, leading to greater uncertainty as to whether there is a lagging component.

4.2.5 Radial Motions

Infalling gas onto a galaxy from the IGM can be influenced by the torques exerted by the rotating disk or halo of the galaxy., resulting in a co-rotating accretion disk encompassing the galaxy and extending out to large radii (Stewart et al., 2013). In this picture, it is expected that accretion from the CGM occurs predominantly in the outskirts of galactic disks. To sustain the star-formation rate in the galaxy, this gas needs to be made available and requires efficient transport from the outermost to the innermost regions of the galaxy where majority of the star formation process occurs. To support this idea, inward radial gas flows are expected through the galactic disk.

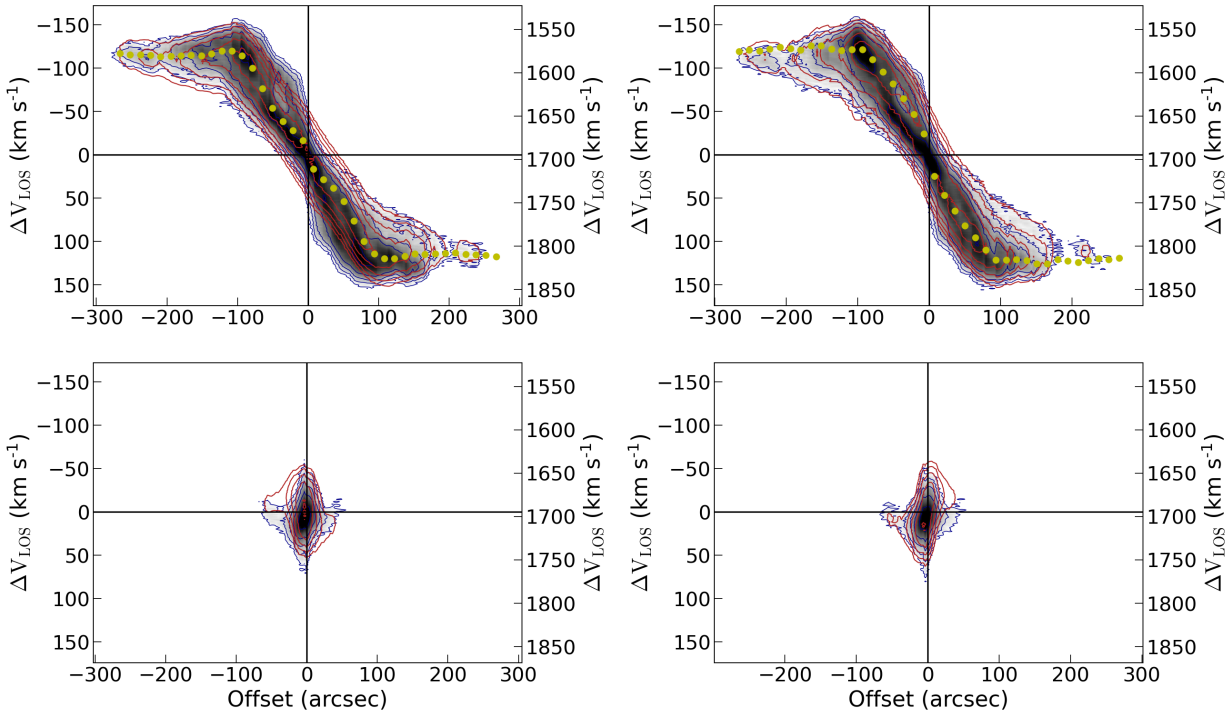

Figure 48: *Position-velocity diagrams of the major-axis (top row) and minor-axis (bottom row) for the tilted-ring models of the approaching half (a) and the receding half (b) of the galaxy*

3DBarolo has the added functionality to model radial motions in the tilted-ring modelling process. The position angle and inclination angles were fixed per ring as in our previous models for the approaching and receding side of the galaxy shown in Figure (34). The velocity dispersion was also fixed to a constant value of 15 km s^{-1} and only the rotation velocity and radial velocities were left as free parameters. All other values in the modelling process were kept the same as the previous models.

The PV-slices in Figure (48) show the correlation between the model and the data. The model of the approaching side reproduces most of the beard gas by looking at the PV-slice of the major-axis but fails to reproduce the emission on the high-velocity side. In the minor-axis PV-slice for the approaching side, the model clearly models emission where the data shows there is none and fails to reproduce a large portion of emission on the RHS of this plot. The model of the receding side in Figure (48 (b)) shows a significant improvement in reproducing emission along the major-axis compared to the approaching side PV-slice. However, once again the emission is not efficiently modelled when assessing the minor-axis PV-slice. It fails to model the emission on the RHS on the plot and does not perform the task of modelling the emission on the LHS to good effect, since only a portion coincides with the model's contours.

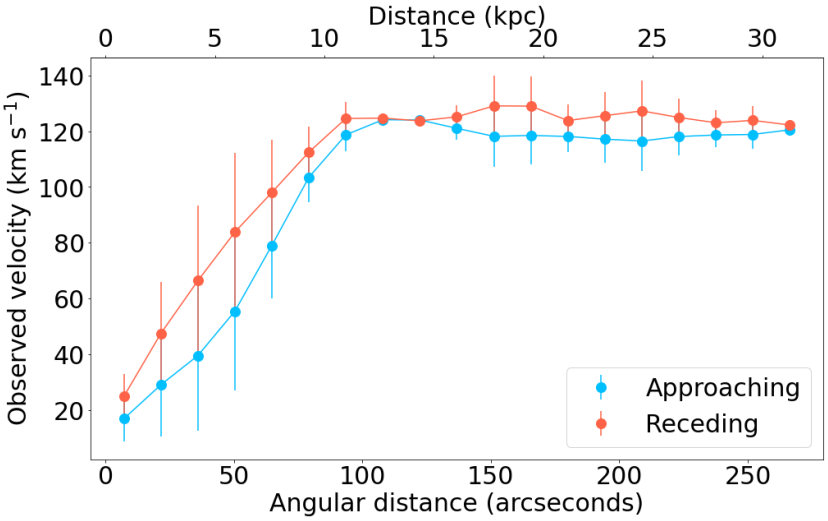

Figure 49: *The rotation curves for the approaching and receding side of the galaxy from the tilted-ring model taking radial motions into account. The errorbars are taken as the difference in the velocities of the approaching and receding sides.*

The rotation curves from both models show a similar deviation in the rotation velocities in the inner regions of the galaxies as previously seen in Figures (37) and (40). This difference is reflected in the rotation curves from the envelope-tracing method in Figure (40) where the receding side of the galaxy rises more sharply than the approaching side in the inner region. In Figure (50) we look at the radial velocities throughout the disk. Under 3DBarolo's definition of radial velocity, positive velocities are outflow when a galaxy is rotating clockwise and inflow when a galaxy is rotating anticlockwise. The converse of this is true, thus positive velocities are inflow when a galaxy is rotating anticlockwise like UGCA 250. The radial motions in Figure (50) imply that the receding side is consistently showing inflows while the approaching side shows inflows until 50" after which outflow velocities are detected in the radial motions. This change in radial motions in the approaching side could explain the slowly rising rotation curve in the inner region of the galaxy. However, these variations could also simply be a consequence of the changing position angle of the galaxy. Radial motions and changes in the position angle can be challenging to disentangle from one another. Models consisting of radial motions and models consisting of a warp in the position angle both cause a clear twist of the LOS velocity contours near the minor-axis with respect to a pure rotating disk (Di Teodoro and Peek, 2021). Furthermore, the models depicted in Figures (51) and (52) show no clear improvement upon the models without radial motions, indicating a lack of radial motions from our models.

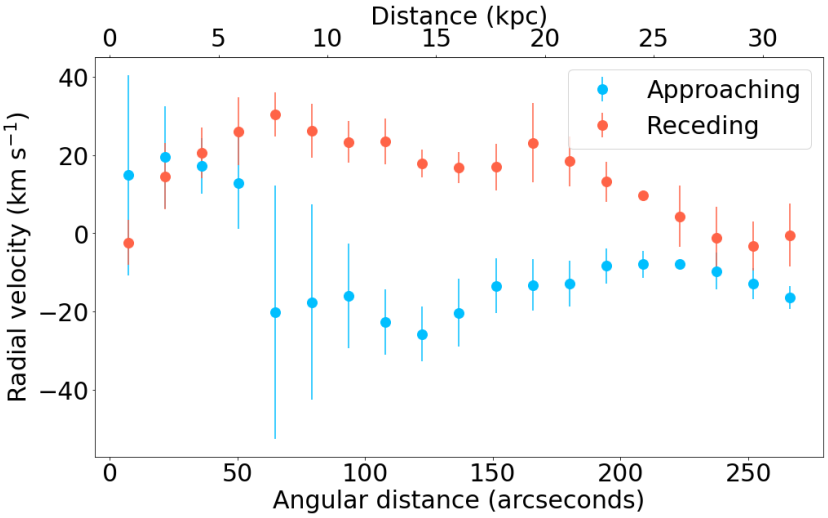

Figure 50: *The radial velocities in the disk for the tilted-ring models of the approaching and receding halves of the galaxy.*

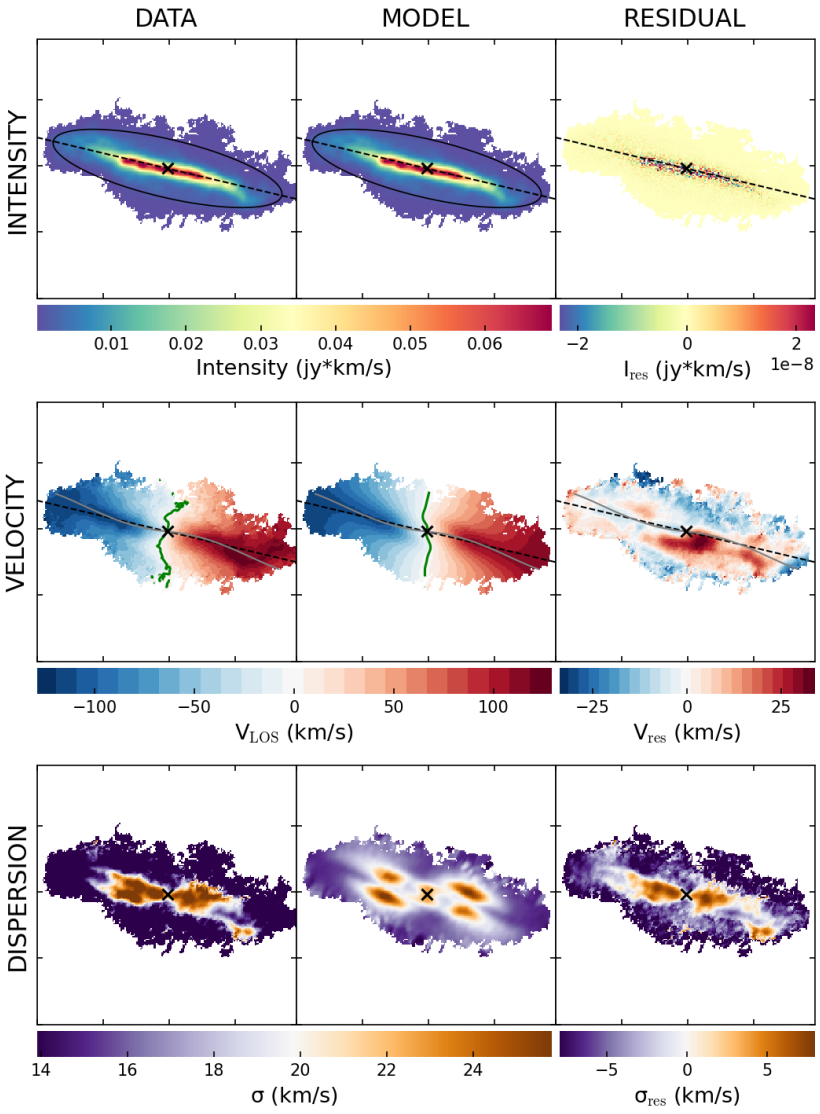

Figure 51: *The moment maps and residual maps for the tilted-ring model for the approaching side of the galaxy. These models have been produced with radial motions taken into account.*

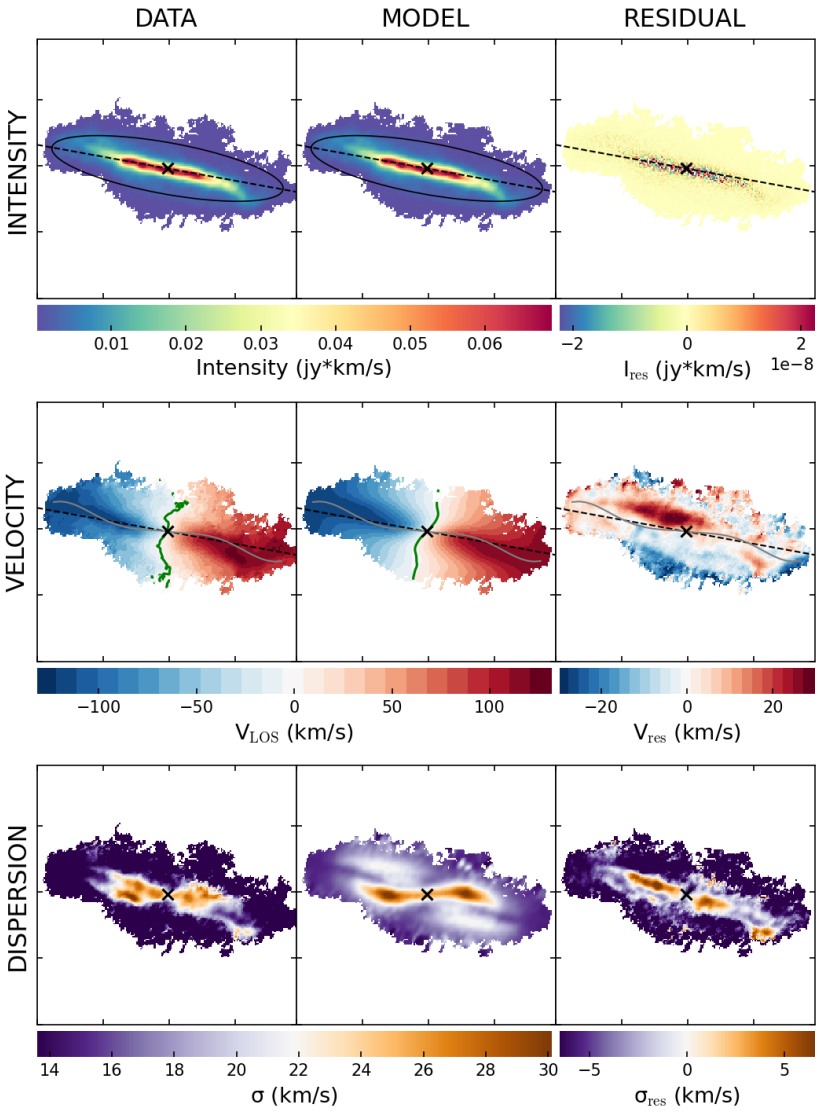

Figure 52: *The moment maps and residual maps for the tilted-ring model for the receding side of the galaxy. These models have been produced with radial motions taken into account.*

4.3 Combined Rotation curves

The rotation curves in Figure (53) show how the kinematics between the HI and the Hα correlate along both the major-axis as well as parallel to it at an offset of 13.7" which corresponds to a physical scale of 1.6 kpc.

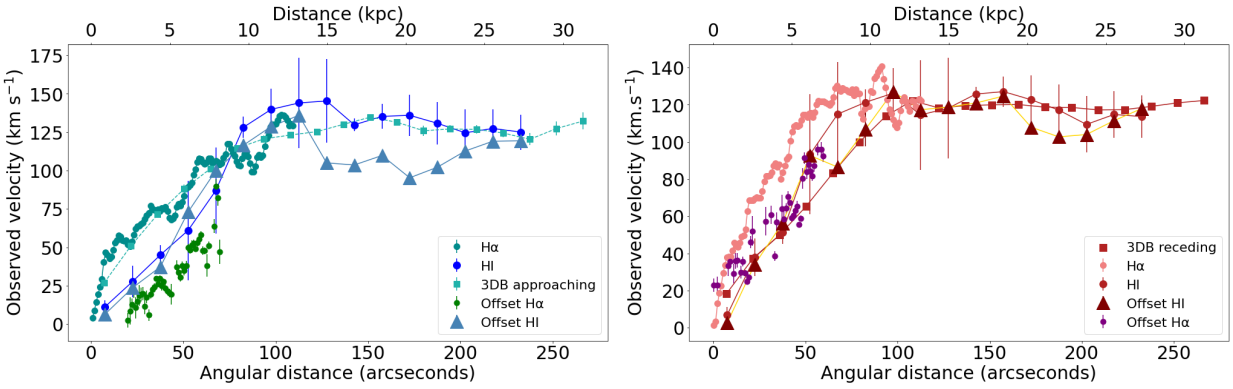

(a) (b)

Figure 53: *The rotation curves of the approaching (a) and receding side (b) of the galaxy. These plots contain the Hα single-component curve, the HI envelope-tracing curve, the 3DBarolo rotation curve as well as the rotation curves from the offset long-slit observations from slits S3 and S4. The offset HI rotation curve was derived with the envelope-tracing method from the PV-slice taken along the positions of S3 and S4.*

Noticeably, there is a discrepancy between the kinematics of the Hα rotation curve and the rotation curves of the HI derived with the envelope-tracing method. These discrepancies are most prevalent in the inner region of the galaxy. This is where we would expect these to arise due to the limited resolution of the radio observations compared to the optical observations which can resolve these denser regions. This difference in resolution between the two observations is seen in the spacing between the consecutive points. The lag between the major-axis velocities and the offset major-axis velocities of Hα is 23.29 km s^{-1} for the approaching side and 22.58 km s^{-1} for the receding side. The lag on the both sides is qualitatively consistent with rotational velocity lags associated with multi-phase gaseous halos (e.g. Fraternali et al., 2002, Fraternali et al., 2004) which is cited as being $\Delta\nu$ = -10-40 km s^{-1} kpc^{-1} observed in nearby edge-on eDIG layers (e.g. Heald et al., 2007). The lags of the HI analogous to the Hα lags are 19.54 km s^{-1} and 7.59 km s^{-1} for the approaching and receding sides respectively. The lag on the approaching side in the HI is relatively consistent with the lag detected in the Hα on this side of the galaxy, while the lag on the receding side is much less than its ionised counterpart.

We compare the rotation of the two components assumed in the profiles of Hα and HI along the major axis to assess whether the kinematics indicate the presence of eDIG or EPG.

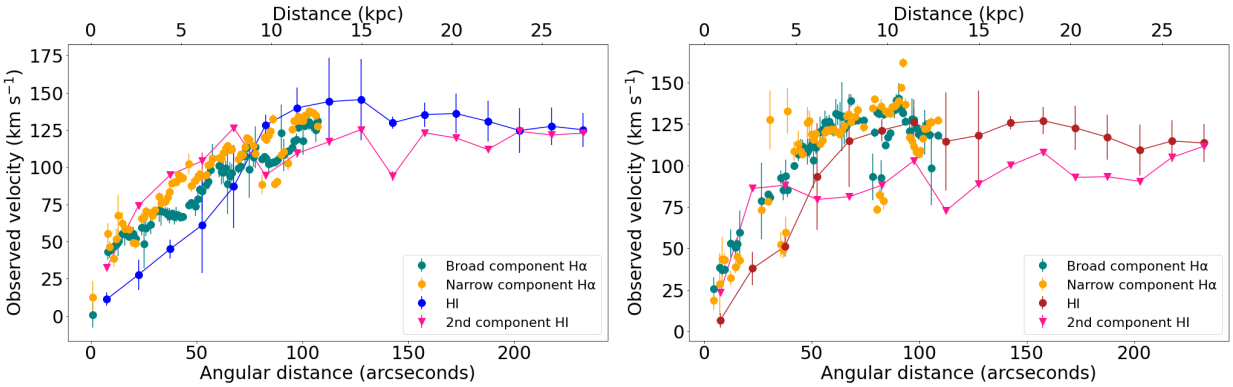

(a) (b)

Figure 54: *The rotation curves along the major-axis of the approaching (a) and receding (b) side. These curves show the kinematics of the two component Hα fits as well as the the two component HI fits with the envelope-tracing method.*

The broad components of the Hα appears to steadily lag behind the respective narrow components with a median lag of 7.27 km s^{-1}. This lag was calculated by taking the difference between the median of the narrow and the broad component velocities. This may be consistent with an eDIG layer, however, the broad components do not possess consistently lower velocities throughout the curve and some may be attributed to pDIG. The associated median difference between the narrow and broad component velocities is 0.32 km s^{-1} for the receding side of the galaxy. This velocity difference is more indicative of the broad component velocities being inherent to pDIG as opposed to eDIG as they do not exhibit a kinematic lag associated with eDIG. There is no distinct trend between whether one component lags more than the other and both seem to be dominated by the rotation of the galaxy, leading one to believe that one component stems from denser HII regions while the other from pDIG and neither can be conclusively assigned to eDIG.

Most noticeably in the inner regions of the HI rotation curves, we see the second component in the fits shows faster rotation than the primary components of the HI. This could be constituted by the limitations of our observations and these velocities are a consequence of beam smearing. The inner regions of the galaxy are the densest regions and coupled with the high inclination, these regions are most susceptible to beam smearing. Toward the outer region, both curves show relatively similar velocities between the two components, but the receding side shows a stronger deviation in the velocities between the two components. Here, we take the median lags between the first and second HI components and obtain a lag of 13.36 km s^{-1} and 25.19 km s^{-1} for the approaching and receding sides respectively. The velocity difference between the components on the receding side is nearly twice that of the difference on the approaching side. This could be a consequence of the warp in the disk of the galaxy, where the pv slice effectively samples more of the thin disk on the approaching side as opposed to the receding side.

5 Discussion

5.1 Kinematic evidence for eDIG

Observations of UGCA 250 taken with SALT and MeerKAT were used to determine the presence of eDIG and EPG in the galaxy. Multiple long-slit observations were conducted with the goal of studying the kinematics of the ionised gas in different regions of the galaxy. The fitting of Hα from these observations allowed for the derivation of rotation curves along the major-axis and minor-axis as well as at positions parallel to these axes of UGCA 250. Rotation curves of the ionised gas parallel to the major-axis offset by 1.6 kpc reveal the presence of ionised gas rotating more slowly than that of the disk. The estimated scale height of the ionised disk was taken to be 0.49 kpc. The presence of lagging ionised gas at a distance much greater than the scale height leads us to believe that this gas is extraplanar. Due to the physical warp in the structure of the disk, these long-slit observations conducted parallel to the major-axis only sample emission from either the receding or approaching side of the galaxy. Furthermore, there is a kinematic lag detected on either side with respect to the velocities along the major-axis. The lag above the disk (on the receding side) is 23.29 km s^{-1} and below the disk (on the approaching side) is 22.58 km s^{-1}. Both of these values are characteristic of the rotational velocity lags in eDIG layers commonly observed in nearby galaxies (e.g. Heald et al., 2007, Bizyaev et al., 2017, Li et al., 2021). However, due to the warp and high inclination of the disk, this may just be gas being probed at different galactrocentric radii resulting in an apparent kinematic lag.

Similarly, the rotational velocities in the HI were found and compared in these regions of long-slit observations. The associated lags in the HI were lower than that of the ionised gas. One issue with this is that in the inner regions for these HI curves, the kinematics appear to be similar for the HI along the major-axis and the HI along the off-axis cuts analogous to the off-axis long-slit observations parallel to the major-axis. A reason for this is beam smearing, the effects of which are more prominent the more inclined a galaxy is. A consequence of this is that rotation curves rise slower than they should be in the inner regions (e.g. Lelli et al., 2010). This effect is seen in this work where we would expect the kinematics of the HI and Hα to agree (e.g. Fraternali et al., 2004), however, the rotation curve of the HI has significantly lower rotation velocities in the inner regions of the galaxy. In the outer regions of the rotation curves for the HI, we do see a lag between the velocities along the major-axis and the velocities along the off-axis cuts analogous to the off-axis long-slit observations parallel to the major-axis. This is not definitive of an EPG layer, but could be showing that the galaxy only exhibits a radially varying lag in its disk.

The minor-axis rotation curve does not provide any clear indication of eDIG. The single-component rotation curve is largely flat throughout the rotation curve, indicating that the rotation velocities are distributed about the systemic velocity. In the two-component rotation curve we do, however, see a broad component with velocities lower than that of the narrow. These broad velocities have large uncertainties which could be attributed to the ripple in the disk as opposed to eDIG. The galaxy being edge-on and exhibiting a warp, means that the long-slit samples emission from the face of the disk as well. Thus diffuse gas from greater radii in the disk could be presenting itself in the emission line as opposed to eDIG emission. In the two-component fits for the observations parallel to the minor-axis, there is no clear indication of eDIG. There is a lagging component of gas at each spatial position in the rotation curves, but this is not consistently the broad component. This does not allow us to make a definite conclusion as to whether eDIG is present along these slices due to a variation as to which component lags with respect to the other. The kinematics of the broad component proved to be consistent with both pDIG and eDIG in the disk from the major-axis rotation curve by exhibiting a velocity lag compared to the narrow component in some regions whilst following the rotation of the disk in other regions.

In this work, two components were assumed. The high inclination of the galaxy imposes many challenges when modelling the emission lines with one issue being that a LOS penetrates many regions of planar and/or extraplanar gas. This can cause a LOS sampling emission from multiple HII regions in the disk, which can result in multiple 'narrow' components in an emission line causing broadened wings of emission in the profile. Approximating the emission lines as two components is justified by previous studies which stipulate that the velocity dispersion in diffuse gas may be higher than in HII regions (e.g. Boettcher et al., 2016, Boettcher et al., 2017, Zhu et al., 2023). This served as motivation to employ a two-component Gaussian model with a narrow component representative of the emission from HII regions and a broad component representative of diffuse ionised gas.

5.2 Lack of evidence for eDIG in the flux ratios

The single component flux ratios of [NII]/Hα as a function of distance from the midplane do show that these ratios are enhanced with greater distance when assessing the values for the observations along and parallel to the minor-axis, characteristic of eDIG (e.g. Haffner et al., 2009). Although these values never reach unity and that the flux of Hα dominates everywhere, the ratios increase along the minor-axis as we move beyond 500pc which is greater than the assumed scale height of the ionised disk. The ratios for the parallel minor-axes observations are confined within about 500 pc of either side of the disk, but the receding side does show increasing ratios when moving away from the midplane on either side of the galaxy. The same can not be said for the observation along the approaching side of the galaxy, but these values are consistently higher than the ratios along the receding side.

The two-component ratios along these lines of observations do not show as distinct a trend in either component being enhanced as a function of distance. The ratios of the two components along the minor axes observations show a similar trend in being enhanced, albeit not as conclusive and not consistent. One would expect a consistently higher broad component ratio to indicate that there is a dominant diffuse gaseous component above and below the disk associated with eDIG. This is not seen here and there is variation as to which components have higher ratios. A caveat in the analysis of the flux ratios along the parallel minor-axis observations was that the SNR cut-off needed to be reduced from 3 to 1 in order to obtain enough data points to assess a trend in the two-component flux ratios. This explains the failure to detect a diffuse component representative of eDIG in the two-component flux ratios off the disk of the galaxy. The flux ratios analysed in this work do not provide any clear evidence as to whether eDIG is associated with UGCA 250.

5.3 Comparison of Hα and HI rotation curves

The single-component rotation curves between the HI and Hα show that the Hα rotates faster in the inner region of the galaxy where the Hα velocities are rising more quickly. This is true when comparing the ionised gas kinematics to the rotation curves derived via the envelope-tracing method on either side of the galaxy. The velocities of the second component in the envelope-tracing method agrees better with the Hα velocities within 5 kpc of the center of the galaxy as opposed to the main component velocities. This discrepancy in the HI velocities can be a consequence of beam-smearing effects being maximised in this denser, inner region of the galaxy. However, the Hα velocities are traced well by the rotation curve of the tilted-ring model on the approaching side of the galaxy, but this correlation between the velocities is not present on the receding side of the galaxy. One issue with this analysis is that the assumed center of the galaxy for the Hα fits was the position of maximum intensity as opposed to the kinematic center of the galaxy. This could introduce some slight errors in interpreting the kinematics of the disk. Something to note regarding the long-slit observations along the major-axis would be the regions of the disk the observation actually probes. It is assumed that the kinematic major-axis is observed, however, the disk does have a structural warp. Thus, the slit may

only be probing the major-axis of the galaxy on one half of the galaxy due to this asymmetry in structure, leading to slight deviations in the measured Hα rotation curves on either side of the galaxy.

5.4 Tilted-ring models

The residuals from the tilted-ring models in this work show that the disk of the galaxy is asymmetric and the approaching and receding sides need to be modelled independently to describe the kinematics of the HI. The HI disk does have a warp and this is traced by the changing position angle of the models which do not describe the warp as being identical in shape on either side of the galaxy. The models also describe a similar trend in the velocities on either side of the galaxy, but the model for the approaching side has velocities in the rotation curve consistently higher than that of the receding side. This is true for both the rising and flat section of the rotation curves. The behaviour of the approaching side rotating faster on the outskirts is affirmed by comparing the rotation curves obtained with the envelope-tracing method which also show the approaching side rotating faster in the flat part of the rotation curve.

The tilted-ring models applied in this work all describe the galaxy as a single disk. The scale height of this disk was measured by fitting a decaying exponential to the flux distribution perpendicular to the plane of the disk. However, the fit with a singular exponential term did not perform an adequate fit to the data by eye. When applying a two exponent fit, a much better fit is obtained which suggests that this galaxy has two gaseous disks of different scale heights. This, along with the kinematics of the HI suggest that this galaxy can not be sufficiently modelled with the assumption of a singular disk and perhaps a model consisting of a thin and a thick HI disk would efficiently reproduce the HI features (e.g. Zschaechner et al., 2015). The Gaussian decomposition revealed that there was more than a single component present throughout the disk. More complex modelling is required to accurately model both components simultaneously, which can not be done with 3DBarolo as it is unable to perform simultaneous modelling of multiple components. More detailed kinematic modelling involving the addition of distortions simulating arcs or spiral arms could significantly improve the model of an edge-on galaxy (Kamphuis et al., 2013).

One issue with the tilted-ring models in this work is that the adopted scale-height is based on the assumption of one disk being present. The peculiar kinematics of the HI in the galaxy suggest that a singular disk is not sufficient to describe the kinematics and there may be both a thin and a thick HI disk associated with this galaxy. Figure (55) shows the quality of the fit performed on the intensity distribution as a function of distance from the midplane for a decaying exponential. The single-exponential fit appears to provide a reasonable fit by eye, however, the scale height calculated from this exponential fit was 12.28" which corresponds to a physical scale of about 1.44 kpc, suggesting that this function is only providing an estimate of the vertical scale height for the thin HI disk. Furthermore, the shape of the curve suggests that a better fit may be obtained by employing either a *sech* or Gaussian function. Another caveat is the value of the measured scale height is close to the beam size of the observation. The major-axis is 14.37" which indicates that the measured scale height is a value close to a resolution element of the observation, suggesting that the scale height used in this work is not entirely accurate and is one of the limitations of modelling the galaxy with a single disk. This led to investigating the kinematics through another method of analysis, which is why the envelope-tracing method was also used in this work.

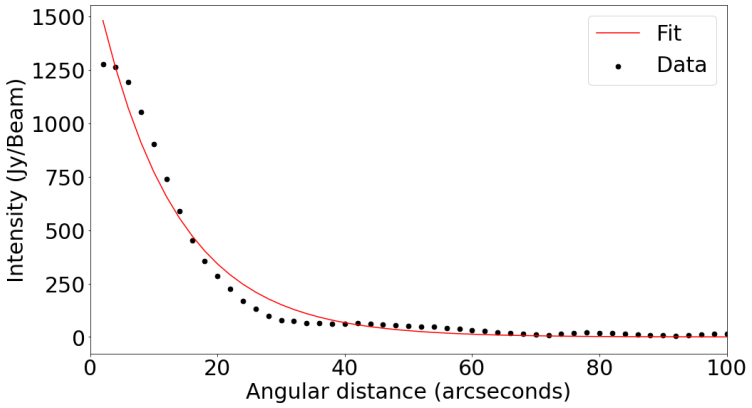

Figure 55: *Decaying exponential fits of the intensity as a function of distance from the midplane of the galaxy.*

The presence of radial motions was also investigated in this work, however, no conclusive results were ascertained as to quantify the radial motions. The results obtained do suggest that radial motions could be present in this galaxy, either in the form of inflows or outflows but these results have much uncertainty and need to be investigated more thoroughly. More extensive modelling is required to confirm the presence of these motions.

5.5 HI Gaussian decomposition

Building upon this idea of two disk components in the HI, the Gaussian decomposition performed on the HI velocity profiles revealed that there was a lagging diffuse component throughout the disk of the galaxy under our assumption that the profiles exist as a superposition of two components where one pertains to the thin HI disk and the other a diffuse component. This broad component presents itself within the disk and lags in some areas with respect to the narrow component, while rotating faster in other areas. The lagging diffuse components could be consistent with EPG layers associated with the galaxy, but the high inclination of the galaxy suggests that these lagging components could be a consequence of HI sampled at greater galactrocentric radii by our LOS which presents this gas as rotating more slowly. Future work would involve a tilted-ring analysis on both of the cubes representative of the broad and narrow disk components respectively to characterise the kinematic differences between the two components.

The single-component fits are all situated in the outskirts of the galaxy. These are not representative of a lagging EPG layer, but come as a result of the projection effects being less pronounced in the outskirts where the gas is less dense. Another possibility is that the signal-to-noise is lower in these regions, making it harder to distinguish multiple Gaussian components in these profiles. The velocity dispersions of the single components are distributed between the narrow and broad component velocities as shown in Figure (46). These dispersions not being mostly consistent with the dispersions of either component indicates that this gas is not necessarily extraplanar and is disk gas in regions where the projection effects are minimised. EPG can only be separated kinematically in face-on or intermediately incline galaxies (e.g. Marasco et al., 2019), here the limitations are clear when applying Gaussian decomposition to an edge-on galaxy.

5.6 Is eDIG present?

As explained in section (1), the presence of eDIG in external galaxies is determined by the following criteria: (1) The flux ratios of [NII]/Hα are elevated with distance from the galactic disk (e.g. Madsen et al., 2006), (2) the velocity dispersions of diffuse gas are significantly higher than that of the HII regions in the disk (e.g. Boettcher et al., 2016, Boettcher et al., 2017) and (3) eDIG exhibits a kinematic lag with respect to the gas in the disk (e.g. Fraternali et al., 2004, Bizyaev et al., 2017). The flux ratios for UGCA 250 along the minor-axis provide no conclusive evidence as to whether there exists a layer of eDIG. This is true for the observations along the minor-axis as well as the observations taken parallel to the minor-axis. Through fitting the emission-lines of Hα with two components, we were able to show that there were regions in the galaxy in which the emission-line consisted of both a narrow and a broad component. We assumed that the broad component was constituted by the diffuse gas in the galaxy while the narrow component stemmed from the emission from HII regions. One caveat with this approach is that multiple 'narrow' components from multiple HII regions along a LOS can exist in the emission-line, giving the appearance of broadened wings on the emission-line. This work assessed whether there was a distinct kinematic lag in the ionised gas above and below the disk through long-slit observations parallel to the major-axis. These observations showed that there was an apparent lag in the kinematics between the gas probed in this observation compared to the velocities in the major-axis. However, the warp of the disk and high inclination suggest that the apparent lag is a consequence of the LOS sampling emission from different galactrocentric radii in the disk. We find no clear evidence for eDIG that satisfy the aforementioned criteria. This work further demonstrates how high-resolution spectroscopy is an extremely viable method of analysis to be used in probing for eDIG and obtaining a complete kinematic analysis of an external galaxy.

5.7 The connection to star formation

A layer eDIG has been shown to be ubiquitous in starburst galaxies, which are galaxies considered to exhibit a high rate of star formation (Lehnert and Heckman, 1995). We employ the same definition for starburst galaxies as in Lu et al. (2023b) where a galaxy is considered to be starburst if $SFR_{\rm SD} > 0.002\,M_\odot\,{\rm yr}^{-1}\,{\rm kpc}^{-2}$. Using the Star formation rate of $SFR = 0.44\,M_\odot\,{\rm yr}^{-1}$ determined in Cluver et al. (2018) and the radius of the disk being 13.17 kpc obtained from assessing the extent of Hα emission using Figure (13), we find:

$$\begin{aligned} SFR_{\rm SD} &= \frac{SFR}{\pi(r)^2} \\ SFR_{\rm SD} &= \frac{0.44}{\pi(13.17)^2} \\ &= 0.81 \times 10^{-3}\,M_\odot\,{\rm yr}^{-1}\,{\rm kpc}^{-2} \end{aligned} \tag{16}$$

This value indicates that the galaxy does not display large amounts of star formation and can be classified as a non-starburst galaxy under the aforementioned criteria. The low rate of star formation density suggests that the likelihood of a layer of eDIG being present in UGCA 250 might be lower, as it is less probable to possess such a layer as a result of star formation activity.

6 Conclusion

Observations of MHONGOOSE galaxy UGCA 250 were taken with both MeerKAT as well as the RSS instrument on SALT. These observations were used in conjunction to obtain a comprehensive study of the kinematics of the gas associated with the galaxy. Multiple long-slit observations allow for the ionised gas to be studied in different regions of the galaxy such as along the major and minor axes as well as along positions parallel to these axes. Furthermore, this work illustrates a comprehensive analysis in the search for signatures of extraplanar gas associated with this galaxy in the form of both ionised gas as well as HI. This was done by measuring the velocities of ionised gas residing outside of the main disk, assessing the trend in the [NII]/Hα flux ratios with distance from the galaxy and the detection of eDIG through multiple-component emission-line modelling.

The two-component fits conducted on the Hα line reveal the presence of two gaseous components in the galaxy where some of the components are characteristic of pDIG and others of eDIG in certain regions of the galaxy. However, the high inclination of the galaxy imposes many challenges to this approach. One of which is that an emission line can consist of contributions from many HII regions, resulting in a broadened profile constituted by these multiple narrow components. The diagnostic [NII]/Hα plots do not provide clear indications of a layer of eDIG associated with this galaxy. The long-slit observations parallel to the major-axis that probe ionised gas at a distance of 1.6 kpc from the major-axis reveals lagging ionised gas with respect to the major-axis. The galaxy does have a structural warp, the effect of which is that these slits are only probing emission on the outskirts of the disk as opposed to eDIG. This is affirmed by the slit above the disk only probing emission on the receding side while the same can be said for the slit below the disk regarding the approaching side.

The tilted-ring models applied to this galaxy show that the kinematics of this galaxy is complex and requires a more extensive modelling scheme to fully describe the HI kinematics throughout the galaxy. The envelope-tracing method was employed to compare the rotation curves of the HI obtained with the tilted-ring models. These curves largely agree with each other as well as the Hα, however, the Hα provides a more robust estimation of the velocities in the inner regions of the galaxy. The analysis performed on the HI data revealed that there exists more than a single disk associated with this galaxy and that a more comprehensive analysis of the kinematics would require modelling this galaxy with two disks as opposed to one.

This work exhibits how the combination of radio data achieved at both a high sensitivity and high resolution can be combined with high-resolution long-slit spectroscopy. This work further demonstrates how this can be applied to a MHONGOOSE galaxy and contribute to accomplishing one of its chief scientific aims.

References

[1] E. P. Hubble. "Extragalactic nebulae." In: 64 (Dec. 1926), pp. 321–369. DOI: 10.1086/143018.

[2] R. G. Bower et al. "Precision photometry of early-type galaxies in the Coma and Virgo clusters : a test of the universality of the colour-magnitude relation - II. Analysis." In: 254 (Feb. 1992), p. 601. DOI: 10.1093/mnras/254.4.601.

[3] Yoshiaki Sofue and Vera Rubin. "Rotation Curves of Spiral Galaxies". In: 39 (Jan. 2001), pp. 137–174. DOI: 10.1146/annurev.astro.39.1.137. arXiv: astro-ph/0010594 [astro-ph].

[4] Stefano Casertano and J. H. van Gorkom. "Declining Rotation Curves: The End of a Conspiracy?" In: 101 (Apr. 1991), p. 1231. DOI: 10.1086/115759.

[5] H. I. Ewen and E. M. Purcell. "Observation of a Line in the Galactic Radio Spectrum: Radiation from Galactic Hydrogen at 1,420 Mc./sec." In: 168.4270 (Sept. 1951), p. 356. DOI: 10.1038/168356a0.

[6] J. Jonas and MeerKAT Team. "The MeerKAT Radio Telescope". In: *MeerKAT Science: On the Pathway to the SKA*. Jan. 2016, 1, p. 1. DOI: 10.22323/1.277.0001.

[7] Fernando Camilo. "African star joins the radio astronomy firmament". In: *Nature Astronomy* 2 (July 2018), pp. 594–594. DOI: 10.1038/s41550-018-0516-y.

[8] D. H. Rogstad and G. S. Shostak. "Aperture synthesis study of neutral hydrogen in the galaxy M101: I. Observations." In: 13 (June 1971), pp. 99–107.

[9] R. A. Swaters, R. Sancisi, and J. M. van der Hulst. "The H I Halo of NGC 891". In: 491.1 (Dec. 1997), pp. 140–145. DOI: 10.1086/304958. arXiv: astro-ph/9707150 [astro-ph].

[10] Colin A. Norman and Satoru Ikeuchi. "The Disk-Halo Interaction: Superbubbles and the Structure of the Interstellar Medium". In: 345 (Oct. 1989), p. 372. DOI: 10.1086/167912.

[11] Paul R. Shapiro and George B. Field. "Consequences of a New Hot Component of the Interstellar Medium". In: 205 (May 1976), pp. 762–765. DOI: 10.1086/154332.

[12] Matthew D. Lehnert and Timothy M. Heckman. "Ionized Gas in the Halos of Edge-on Starburst Galaxies: Evidence for Supernova-driven Superwinds". In: 462 (May 1996), p. 651. DOI: 10.1086/177180.

[13] Tom Oosterloo et al. "The Cold Gaseous Halo of NGC 891". In: 134.3 (Sept. 2007), p. 1019. DOI: 10.1086/520332. arXiv: 0705.4034 [astro-ph].

[14] Bregman. "The Search for the Missing Baryons at Low Redshift". In: 45.1 (Sept. 2007), pp. 221–259. DOI: 10.1146/annurev.astro.45.051806.110619. arXiv: 0706.1787 [astro-ph].

[15] Di Teodoro and Fraternali. "Gas accretion from minor mergers in local spiral galaxies". In: 567, A68 (July 2014), A68. DOI: 10.1051/0004-6361/201423596. arXiv: 1406.0856 [astro-ph.GA].

[16] Dušan Kereš et al. "How do galaxies get their gas?" In: 363.1 (Oct. 2005), pp. 2–28. DOI: 10.1111/j.1365-2966.2005.09451.x. arXiv: astro-ph/0407095 [astro-ph].

[17] George B. Field and William C. Saslaw. "A Statistical Model of the Formation of Stars and Interstellar Clouds." In: 142 (Aug. 1965), p. 568. DOI: 10.1086/148318.

[18] J. Rossa and R. -J. Dettmar. "An Hα survey aiming at the detection of extraplanar diffuse ionized gas in halos of edge-on spiral galaxies. I. How common are gaseous halos among non-starburst galaxies?" In: 406 (Aug. 2003), pp. 493–503. DOI: 10.1051/0004-6361:20030615. arXiv: astro-ph/0304452 [astro-ph].

[19] R. J. Reynolds et al. "Evidence for an Additional Heat Source in the Warm Ionized Medium of Galaxies". In: 525.1 (Nov. 1999), pp. L21–L24. DOI: 10.1086/312326. arXiv: astro-ph/9911047 [astro-ph].

[20] Scott T. Miller and Sylvain Veilleux. "Extraplanar Emission-Line Gas in Edge-On Spiral Galaxies. I. Deep Emission-Line Imaging". In: 148.2 (Oct. 2003), pp. 383–417. DOI: 10.1086/376604. arXiv: astro-ph/0305026 [astro-ph].

[21] Bregman. "The galactic fountain of high-velocity clouds." In: 236 (Mar. 1980), pp. 577–591. DOI: 10.1086/157776.

[22] Richard J. Rand. "Diffuse Ionized Gas in Nine Edge-on Galaxies". In: 462 (May 1996), p. 712. DOI: 10.1086/177184.

[23] R. -J. Dettmar. "Tracers of Extra-planar Gas and the Disk-Halo Connection". In: *Extra-Planar Gas*. Ed. by Robert Braun. Vol. 331. Astronomical Society of the Pacific Conference Series. June 2005, p. 155.

[24] Fraternali et al. "Deep H I Survey of the Spiral Galaxy NGC 2403". In: 123.6 (June 2002), pp. 3124–3140. DOI: 10.1086/340358. arXiv: astro-ph/0203405 [astro-ph].

[25] Fraternali et al. "Kinematics of the ionised gas in the spiral galaxy NGC 2403". In: 424 (Sept. 2004), pp. 485–495. DOI: 10.1051/0004-6361:20040529. arXiv: astro-ph/0405619 [astro-ph].

[26] Li-Yuan Lu et al. "eDIG-CHANGES I: extended H emission from the extraplanar diffuse ionized gas (eDIG) around CHANG-ES galaxies". en. In: *Monthly Notices of the Royal Astronomical Society* 519.4 (Jan. 2023), pp. 6098–6110. ISSN: 0035-8711, 1365-2966. DOI: 10.1093/mnras/stad006.

[27] Zschaechner et al. "HALOGAS: HI Observations and Modeling of the Nearby Edge-on Spiral Galaxy NGC 4565". en. In: *The Astrophysical Journal* 760.1 (Nov. 2012). arXiv:1210.0609 [astro-ph], p. 37. ISSN: 0004-637X, 1538-4357. DOI: 10.1088/0004-637X/760/1/37.

[28] Richard J. Rand. "A Very Deep Spectrum of the Diffuse Ionized Gas in NGC 891". In: 474.1 (Jan. 1997), pp. 129–139. DOI: 10.1086/303455.

[29] L. M. Haffner et al. "The warm ionized medium in spiral galaxies". en. In: *Reviews of Modern Physics* 81.3 (July 2009). arXiv:0901.0941 [astro-ph], pp. 969–997. ISSN: 0034-6861, 1539-0756. DOI: 10.1103/RevModPhys.81.969.

[30] Heald et al. "Integral Field Unit Observations of NGC 4302: Kinematics of the Diffuse Ionized Gas Halo". In: 663.2 (July 2007), pp. 933–947. DOI: 10.1086/518087. arXiv: astro-ph/0703324 [astro-ph].

[31] Collins et al. "Kinematics of Diffuse Ionized Gas Halos: A Ballistic Model of Halo Rotation". In: 578.1 (Oct. 2002), pp. 98–108. DOI: 10.1086/342309. arXiv: astro-ph/0206193 [astro-ph].

[32] Anqi Li et al. "Fountain-driven gas accretion feeding star formation over the disc of NGC 2403". In: 520.1 (Mar. 2023), pp. 147–160. DOI: 10.1093/mnras/stad129. arXiv: 2301.03614 [astro-ph.GA].

[33] H. Domgorgen and John S. Mathis. "The Ionization of the Diffuse Ionized Gas". In: 428 (June 1994), p. 647. DOI: 10.1086/174275.

[34] Richard J. Rand. "Further Spectroscopy of the Diffuse Ionized Gas in NGC 891 and Evidence for a Secondary Source of Ionization". In: 501.1 (July 1998), pp. 137–152. DOI: 10.1086/305814. arXiv: astro-ph/9802045 [astro-ph].

[35] B. Otte et al. "Emission Line Ratios and Variations in Temperature and Ionization State in the Diffuse Ionized Gas of Five Edge-on Galaxies". en. In: *The Astrophysical Journal* 572.2 (June 2002). arXiv:astro-ph/0202495, pp. 823–837. ISSN: 0004-637X, 1538-4357. DOI: 10.1086/340381.

[36] de Blok et al. *An Overview of the MHONGOOSE Survey: Observing Nearby Galaxies with MeerKAT*. 2017. arXiv: 1709.08458 [astro-ph.GA].

[37] Fabian Walter et al. "THINGS: THE H I NEARBY GALAXY SURVEY". In: *The Astronomical Journal* 136.6 (Nov. 2008), pp. 2563–2647. DOI: 10.1088/0004-6256/136/6/2563. URL: https://doi.org/10.1088%2F0004-6256%2F136%2F6%2F2563.

[38] Heald et al. "The Westerbork Hydrogen Accretion in LOcal GAlaxieS (HALOGAS) survey. I. Survey description and pilot observations". In: 526, A118 (Feb. 2011), A118. DOI: 10.1051/0004-6361/201015938. arXiv: 1012.0816 [astro-ph.CO].

[39] M. J. Meyer et al. "The HIPASS catalogue - I. Data presentation". In: 350.4 (June 2004), pp. 1195–1209. DOI: 10.1111/j.1365-2966.2004.07710.x. arXiv: astro-ph/0406384 [astro-ph].

[40] Gerhardt R. Meurer et al. "The Survey for Ionization in Neutral Gas Galaxies. I. Description and Initial Results". In: 165.1 (July 2006), pp. 307–337. DOI: 10.1086/504685. arXiv: astro-ph/0604444 [astro-ph].

[41] Piero Madau and Mark Dickinson. "Cosmic Star-Formation History". In: 52 (Aug. 2014), pp. 415–486. DOI: 10.1146/annurev-astro-081811-125615. arXiv: 1403.0007 [astro-ph.CO].

[42] D. Espada et al. "Star Formation in the Extended Gaseous Disk of the Isolated Galaxy CIG 96". In: 736.1, 20 (July 2011), p. 20. DOI: 10.1088/0004-637X/736/1/20. arXiv: 1107.0588 [astro-ph.CO].

[43] Jason Tumlinson et al. "The Circumgalactic Medium". In: 55.1 (Aug. 2017), pp. 389–432. DOI: 10.1146/annurev-astro-091916-055240. arXiv: 1709.09180 [astro-ph.GA].

[44] M. F. Skrutskie et al. "The Two Micron All Sky Survey (2MASS)". In: 131.2 (Feb. 2006), pp. 1163–1183. DOI: 10.1086/498708. URL: https://doi.org/10.1086/498708.

[45] Buckley et al. "Completion and commissioning of the Southern African Large Telescope". In: *Society of Photo-Optical Instrumentation Engineers (SPIE) Conference Series*. Ed. by Larry M. Stepp. Vol. 6267. Society of Photo-Optical Instrumentation Engineers (SPIE) Conference Series. June 2006, 62670Z, 62670Z. DOI: 10.1117/12.673750.

[46] Eric B. Burgh et al. "Prime Focus Imaging Spectrograph for the Southern African Large Telescope: optical design". In: *Instrument Design and Performance for Optical/Infrared Ground-based Telescopes*. Ed. by Masanori Iye and Alan F. M. Moorwood. Vol. 4841. Society of Photo-Optical Instrumentation Engineers (SPIE) Conference Series. Mar. 2003, pp. 1463–1471. DOI: 10.1117/12.460312.

[47] Gerard de Vaucouleurs et al. *Third Reference Catalogue of Bright Galaxies*. 1991.

[48] B. S. Koribalski et al. "The 1000 Brightest HIPASS Galaxies: H I Properties". In: 128.1 (July 2004), pp. 16–46. DOI: 10.1086/421744. arXiv: astro-ph/0404436 [astro-ph].

[49] M. T. Doyle et al. "The HIPASS catalogue - III. Optical counterparts and isolated dark galaxies". In: 361.1 (July 2005), pp. 34–44. DOI: 10.1111/j.1365-2966.2005.09159.x. arXiv: astro-ph/0505591 [astro-ph].

[50] Doug Tody. "The IRAF Data Reduction and Analysis System". In: *Instrumentation in astronomy VI*. Ed. by David L. Crawford. Vol. 627. Society of Photo-Optical Instrumentation Engineers (SPIE) Conference Series. Jan. 1986, p. 733. DOI: 10.1117/12.968154.

[51] Steven M. Crawford et al. "PySALT: the SALT science pipeline". In: *Observatory Operations: Strategies, Processes, and Systems III*. Ed. by David R. Silva, Alison B. Peck, and B. Thomas Soifer. Vol. 7737. Society of Photo-Optical Instrumentation Engineers (SPIE) Conference Series. July 2010, 773725, p. 773725. DOI: 10.1117/12.857000.

[52] Pieter G. van Dokkum. "Cosmic-Ray Rejection by Laplacian Edge Detection". In: 113.789 (Nov. 2001), pp. 1420–1427. DOI: 10.1086/323894. arXiv: astro-ph/0108003 [astro-ph].

[53] Józsa et al. *CARACal: Containerized Automated Radio Astronomy Calibration pipeline*. Astrophysics Source Code Library, record ascl:2006.014. June 2020. ascl: 2006.014.

[54] Bengt Strömgren. "The Physical State of Interstellar Hydrogen." In: 89 (May 1939), p. 526. DOI: 10.1086/144074.

[55] Santiago Erroz-Ferrer et al. "Hα kinematics of S^{4}G spiral galaxies - III. Inner rotation curves". In: 458.2 (May 2016), pp. 1199–1213. DOI: 10.1093/mnras/stw300. arXiv: 1602.02789 [astro-ph.GA].

[56] Lelli et al. "Evolution of dwarf galaxies: a dynamical perspective". In: 563, A27 (Mar. 2014), A27. DOI: 10.1051/0004-6361/201322658. arXiv: 1311.4556 [astro-ph.GA].

[57] Kyle B. Westfall et al. "The DiskMass Survey. IV. The Dark-matter-dominated Galaxy UGC 463". In: 742.1, 18 (Nov. 2011), p. 18. DOI: 10.1088/0004-637X/742/1/18. arXiv: 1108.2946 [astro-ph.CO].

[58] C. R. O'dell and L. K. Townsley. "A very high resolution study of emission line widths in galactic and extragalactic HII regions." In: 198 (June 1988), pp. 283–286.

[59] J. L. Sérsic. "Influence of the atmospheric and instrumental dispersion on the brightness distribution in a galaxy". In: *Boletin de la Asociacion Argentina de Astronomia La Plata Argentina* 6 (Feb. 1963), pp. 41–43.

[60] D. H. Rogstad et al. "Aperture-synthesis observations of H I in the galaxy M83." In: 193 (Oct. 1974), pp. 309–319. DOI: 10.1086/153164.

[61] K. G. Begeman. "HI rotation curves of spiral galaxies". PhD thesis. University of Groningen, Kapteyn Astronomical Institute, Dec. 1987.

[62] J. M. van der Hulst et al. "The Groningen Image Processing SYstem, GIPSY". In: *Astronomical Data Analysis Software and Systems I*. Ed. by Diana M. Worrall, Chris Biemesderfer, and Jeannette Barnes. Vol. 25. Astronomical Society of the Pacific Conference Series. Jan. 1992, p. 131.

[63] P. Teuben. "The Stellar Dynamics Toolbox NEMO". In: *Astronomical Data Analysis Software and Systems IV*. Ed. by R. A. Shaw, H. E. Payne, and J. J. E. Hayes. Vol. 77. Astronomical Society of the Pacific Conference Series. Jan. 1995, p. 398.

[64] Joshua D. Simon et al. "High-Resolution Measurements of the Dark Matter Halo of NGC 2976: Evidence for a Shallow Density Profile". In: 596.2 (Oct. 2003), pp. 957–981. DOI: 10.1086/378200. arXiv: astro-ph/0307154 [astro-ph].

[65] Kristine Spekkens and J. A. Sellwood. "Modeling Noncircular Motions in Disk Galaxies: Application to NGC 2976". In: 664.1 (July 2007), pp. 204–214. DOI: 10.1086/518471. arXiv: astro-ph/0703688 [astro-ph].

[66] A. Bosma. "The distribution and kinematics of neutral hydrogen in spiral galaxies of various morphological types". PhD thesis. University of Groningen, Netherlands, Mar. 1978.

[67] Di Teodoro and Fraternali. *3D-Barolo: a new 3D algorithm to derive rotation curves of galaxies*. 2015. DOI: 10.48550/ARXIV.1505.07834. URL: https://arxiv.org/abs/1505.07834.

[68] Józsa et al. "Kinematic modelling of disk galaxies. I. A new method to fit tilted rings to data cubes". In: 468.2 (June 2007), pp. 731–774. DOI: 10.1051/0004-6361:20066164. arXiv: astro-ph/0703207 [astro-ph].

[69] P. Kamphuis et al. *FAT: Fully Automated TiRiFiC*. Astrophysics Source Code Library, record ascl:1507.011. July 2015. ascl: 1507.011.

[70] R. Sancisi et al. "The Vertical Structure and Kinematics of HI in Spiral Galaxies". In: *Galaxy Disks and Disk Galaxies*. Ed. by José G. Funes and Enrico Maria Corsini. Vol. 230. Astronomical Society of the Pacific Conference Series. Jan. 2001, pp. 111–118. DOI: 10.48550/arXiv.astro-ph/0010407. arXiv: astro-ph/0010407 [astro-ph].

[71] A. Marasco et al. "HALOGAS: the properties of extraplanar HI in disc galaxies". In: 631, A50 (Nov. 2019), A50. DOI: 10.1051/0004-6361/201936338. arXiv: 1909.04048 [astro-ph.GA].

[72] Yoshiaki Sofue. "The Most Completely Sampled Rotation Curves for Galaxies". In: 458 (Feb. 1996), p. 120. DOI: 10.1086/176796. arXiv: astro-ph/9507098 [astro-ph].

[73] M. Kregel and P. C. van der Kruit. "Structure and kinematics of edge-on galaxy discs - III. The rotation curves in the gas". In: 352.3 (Aug. 2004), pp. 787–803. DOI: 10.1111/j.1365-2966.2004.07978.x. arXiv: astro-ph/0405174 [astro-ph].

[74] Rob P. Olling. "NGC 4244: A Low Mass Galaxy With a Falling Rotation Curve and a Flaring Gas Layer". In: 112 (Aug. 1996), p. 457. DOI: 10.1086/118028. arXiv: astro-ph/9605110 [astro-ph].

[75] K. M. Mogotsi et al. "H I and CO Velocity Dispersions in Nearby Galaxies". In: 151.1, 15 (Jan. 2016), p. 15. DOI: 10.3847/0004-6256/151/1/15. arXiv: 1511.06006 [astro-ph.GA].

[76] Boettcher et al. "Testing a Dynamical Equilibrium Model of the Extraplanar Diffuse Ionized Gas in NGC 891". In: 832.2, 118 (Dec. 2016), p. 118. DOI: 10.3847/0004-637X/832/2/118. arXiv: 1609.07491 [astro-ph.GA].

[77] Boettcher et al. "Detection of Extraplanar Diffuse Ionized Gas in M83". In: 845.2, 155 (Aug. 2017), p. 155. DOI: 10.3847/1538-4357/aa81ca. arXiv: 1707.08126 [astro-ph.GA].

[78] Matthew T. Whiting. "DUCHAMP: a 3D source finder for spectral-line data". In: 421.4 (Apr. 2012), pp. 3242–3256. DOI: 10.1111/j.1365-2966.2012.20548.x. arXiv: 1201.2710 [astro-ph.IM].

[79] P. M. W. Kalberla and L. Dedes. "Global properties of the H I distribution in the outer Milky Way. Planar and extra-planar gas". In: 487.3 (Sept. 2008), pp. 951–963. DOI: 10.1051/0004-6361:20079240. arXiv: 0804.4831 [astro-ph].

[80] P. Kamphuis et al. "HALOGAS observations of NGC 5023 and UGC 2082: modelling of non-cylindrically symmetric gas distributions in edge-on galaxies". In: 434.3 (Sept. 2013), pp. 2069–2093. DOI: 10.1093/mnras/stt1153. arXiv: 1306.5312 [astro-ph.GA].

[81] Kyle R. Stewart et al. "Angular Momentum Acquisition in Galaxy Halos". In: 769.1, 74 (May 2013), p. 74. DOI: 10.1088/0004-637X/769/1/74. arXiv: 1301.3143 [astro-ph.CO].

[82] Enrico M. Di Teodoro and Josh E. G. Peek. "Radial motions and radial gas flows in local spiral galaxies". en. In: *The Astrophysical Journal* 923.2 (Dec. 2021). arXiv:2110.01618 [astro-ph], p. 220. ISSN: 0004-637X, 1538-4357. DOI: 10.3847/1538-4357/ac2cbd.

[83] D. Bizyaev et al. "SDSS IV MaNGA - Rotation Velocity Lags in the Extraplanar Ionized Gas from MaNGA Observations of Edge-on Galaxies". en. In: *The Astrophysical Journal* 839.2 (Apr. 2017). arXiv:1704.02582 [astro-ph], p. 87. ISSN: 1538-4357. DOI: 10.3847/1538-4357/aa6979.

[84] Anqi Li et al. "A kinematic analysis of ionized extraplanar gas in the spiral galaxies NGC 3982 and NGC 4152". In: 504.2 (June 2021), pp. 3013–3028. DOI: 10.1093/mnras/stab1043. arXiv: 2104.05736 [astro-ph.GA].

[85] Lelli et al. "Structure and dynamics of giant low surface brightness galaxies". In: 516, A11 (June 2010), A11. DOI: 10.1051/0004-6361/200913808. arXiv: 1003.1312 [astro-ph.CO].

[86] Hanjue Zhu et al. "Spatially Resolved Kinematics of Extraplanar Diffuse Ionized Gas in NGC 3511 and NGC 3513". en. In: arXiv:2306.13012 (June 2023). arXiv:2306.13012 [astro-ph]. URL: http://arxiv.org/abs/2306.13012.

[87] Zschaechner et al. "INVESTIGATING DISK-HALO FLOWS AND ACCRETION: A KINEMATIC AND MORPHOLOGICAL ANALYSIS OF EXTRAPLANAR H I IN NGC 3044 AND NGC 4302". en. In: *The Astrophysical Journal* 799.1 (Jan. 2015), p. 61. ISSN: 1538-4357. DOI: 10.1088/0004-637X/799/1/61.

[88] G. J. Madsen et al. "A Multiwavelength Optical Emission Line Survey of Warm Ionized Gas in the Galaxy". In: 652.1 (Nov. 2006), pp. 401–425. DOI: 10.1086/508441. arXiv: astro-ph/0609558 [astro-ph].

[89] Matthew D. Lehnert and Timothy M. Heckman. "Ionized gas in the halos of edge-on, starburst galaxies: Data and results". en. In: *The Astrophysical Journal Supplement Series* 97 (Mar. 1995), p. 89. ISSN: 0067-0049, 1538-4365. DOI: 10.1086/192137.

[90] Li-Yuan Lu et al. “eDIG-CHANGES I: extended H emission from the extraplanar diffuse ionized gas (eDIG) around CHANG-ES galaxies”. en. In: *Monthly Notices of the Royal Astronomical Society* 519.4 (Jan. 2023), pp. 6098–6110. ISSN: 0035-8711, 1365-2966. DOI: 10.1093/mnras/stad006.

[91] M. E. Cluver et al. “Erratum: “Calibrating Star Formation in WISE Using Total Infrared Luminosity” (2017, ApJ, 850, 68)”. en. In: *The Astrophysical Journal* 860.2 (June 2018), p. 177. ISSN: 0004-637X, 1538-4357. DOI: 10.3847/1538-4357/aacaf6.